Transition Metal Oxides Anchored onto Heteroatom Doped Carbon Nanotubes as Efficient Bifunctional Catalysts for Rechargeable Zinc-Air Batteries

by

Alexandra McDougall

A thesis submitted in partial fulfillment of the requirements for the degree of

Master of Science

in

Materials Engineering

Department of Chemical and Materials Engineering
University of Alberta

Abstract

It is well known that renewable energy, e.g., wind and solar power, are intermittent energy sources. This means that energy storage devices are needed to store the energy for when it is needed. Currently Li-ion batteries are used as these energy storage devices, not only for alternative energy plants but in vehicles and electronics. There are several drawbacks with using Li-ion batteries, such as low safety, harmful Li mining practices, and high material costs. Rechargeable zinc-air batteries (ZABs) have gained a lot of traction recently due to their low cost, high safety, low environmental impact, and high theoretical energy density. However, a major obstacle is the sluggish oxygen reduction reaction (ORR) and oxygen evolution reaction (OER) at the air electrode, which have hindered practical applications of ZABs. Precious metal catalysts have been applied to help mitigate the slow reaction kinetics; however, these are expensive and complicate manufacturing practices since two different precious metals are needed to achieve a bifunctional catalyst. Therefore, a low-cost bifunctional catalyst is needed to improve the slow reaction kinetics at the air electrode.

This work focuses on further investigating a previously developed impregnation technique for air electrode preparation using an array of transition metal (Zn, Ni, Mn, and Co) oxide combinations. Various electrochemical and microstructural characterization techniques, e.g., linear sweep voltammetry, electrochemical impedance spectroscopy, electron microscopy, and energy dispersive X-ray spectroscopy, are used to examine each sample.

The first study involved fabricating several catalysts by decorating nitrogen doped carbon nanotubes (N-CNTs) with either tri-metallic (Ni-Mn-Co) or tetra-metallic (Zn-Ni-Mn-Co) oxides, through a simple impregnation method into carbon-based, gas diffusion layers (GDL). Metal oxide compositions were selected based on previous results, preliminary electrochemical

testing, and statistical design of experiments (DOE). Microstructural characterization was done using electron microscopy and X-ray photoelectron spectroscopy (XPS), and determined that the oxides fabricated were spinel oxides. Samples were electrochemically tested and the best candidates were subjected to full cell testing and bifunctional cycling for 200 charge/discharge cycles at 10 mA/cm^2. The overall bifunctional efficiency, after cycling, of the best $NiMnCoO_x$/N-CNT and $ZnNiMnCoO_x$/N-CNT catalysts was 53.3% and 56.4%, respectively; both outperformed Pt-Ru/C in both overall bifunctional efficiency (38%) and cycling stability. The maximum power density of one of the tetra-metallic oxides exceeded that of Pt-Ru/C (110 mW/cm^2) at 134 mW/cm^2. The addition of Zn with Ni-Mn-Co oxide particles showed improved cycling stability and overall bifunctional efficiency.

The second study investigated the effect of co-doping of carbon nanotubes with nitrogen and sulfur (N,S-CNTs), combined with tri-metallic and tetra-metallic oxides, on the ORR and OER reaction kinetics at the air electrode. The best tri-metallic (Ni-Mn-Co) oxide and tetra-metallic (Zn-Ni-Mn-Co) oxide from the first study were used in this investigation. Microstructural characterization analysis revealed that the Co and Mn valences increased for the Ni-Mn-Co and Zn-Ni-Mn-Co oxides, respectively. Electrochemical testing revealed that the Ni-Mn-Co oxide was comparable to the Pt-Ru/C catalyst with a power density of ~95 mW/cm^2 and Zn-Ni-Mn-Co oxide was comparable to the Pt-Ru/C catalyst with an efficiency of 56.0% at 20 mA/cm^2. The addition of sulfur to the N-CNTs positively impacted the Ni-Mn-Co oxide, leading to a round trip bifunctional cycling efficiency of 55.1% for 200 charge-discharge cycles at 10 mA/cm^2. The impact of sulfur did not have a positive impact on the Zn-Ni-Mn-Co oxide; the LSV results were significantly worse than the equivalent oxide on N-CNTs and the full cell

testing was comparable to the N-CNT oxide. Both tri-metallic and tetra-metallic oxides outperformed Pt-Ru/C during bifunctional cycling.

Preface

This thesis focuses on the synthesis, characterization, and electrochemical testing of air electrodes impregnated with transition metal oxides decorating heteroatom doped carbon nanotubes for rechargeable zinc-air batteries. The research presented in Chapter 3 and Chapter 4, along with the Supporting Information is my original work.

Chapter 3 and Chapter 4 summarizes work done in collaboration with Zahra Abedi (PhD student) in our group. Zahra performed some of the SEM analysis (Chapter 3 and Chapter 4), some TEM analysis (Chapter 4), and contributed to discussions about characterization. Dr. Leistenschneider and Lisa Brandt performed CHNS analysis (Chapter 4). Dr. Anqiang He provided expertise in XPS analysis (Chapter 3). Composition optimization, electrode preparation, electrochemical testing, and some of the SEM analysis were conducted by myself. Manuscript preparation was accomplished with the help of Dr. Douglas Ivey. Additionally, Dr. Ivey performed TEM analysis and provided insight into other characterization analyses.
A version of Chapter 3 has been submitted to the Journal of Applied Electrochemistry (July 2021).

Dedication

To my loving family who have been a constant source of support and encouragement. I am truly grateful to have you in my life.

Acknowledgements

I would like to thank my supervisor Dr. Douglas Ivey for his continuous support and guidance throughout this project. Your expertise and feedback has pushed me to think critically and improve my work. Your patience, work ethic, and deep knowledge inspire me and helped me grow and become a better person and engineer.

I am also grateful to the group members of the Ivey Research Group for their encouragement, friendship, and thoughtful discussions. In particular I would like to thank Zahra Abedi for her encouragement and guidance. You truly made my experience here more enjoyable. I would also like to thank Dr. Anqiang He and Dr. Desirée Leistenschneider for their technical support and input.

Financial support from Future Energy Systems (FES, T06 P03) is gratefully recognized.

I would like to thank my parents for their ongoing support with not only this experience but with everything I pursue in life. Thank you to my sister for being such a great role-model and always pushing me to grow. Your encouragement throughout my life has instilled the confidence I need to follow my passions. Thank you for being my emotional support system when I needed it most. Finally I would like to thank my best friend for her words of encouragement and friendship.

Table of Contents

List of Figures:

List of Tables:

1.0. Introduction

Renewable energy sources (e.g., wind turbines and solar panels) are becoming more relevant in today's society as a way of becoming more environmentally friendly. Unlike non-renewable energy (e.g., oil, coal, and natural gas), renewable energy sources only supply intermittent energy. This causes a need for energy storage materials that can reliably supply power needed during peak hours. Typically Li-ion batteries are used commercially. However, Li-ion batteries have issues with high cost, high environmental impacts, and safety concerns [1], [2]. Recently, metal-air batteries have been gaining traction as they have high energy density since air is not stored inside the battery casing. Figure 1-1 shows various metal-air batteries and their specific energies, volumetric energy densities, and nominal cell voltages. Although Li-air has the highest theoretical specific energy (5928 Wh/kg), Li is unstable when exposed to air [1]. Mg and Al have the second highest theoretical specific energies; however, they have low reduction potentials which can lead to fast self-discharge and poor charging efficiencies [1]. Zn-air batteries (ZABs) have gained traction because of their high theoretical energy density (1218 Wh/kg – 1353 Wh/kg), good stability in alkaline environments, high safety and environmentally friendly nature, and low cost [1], [3], [4], [5].

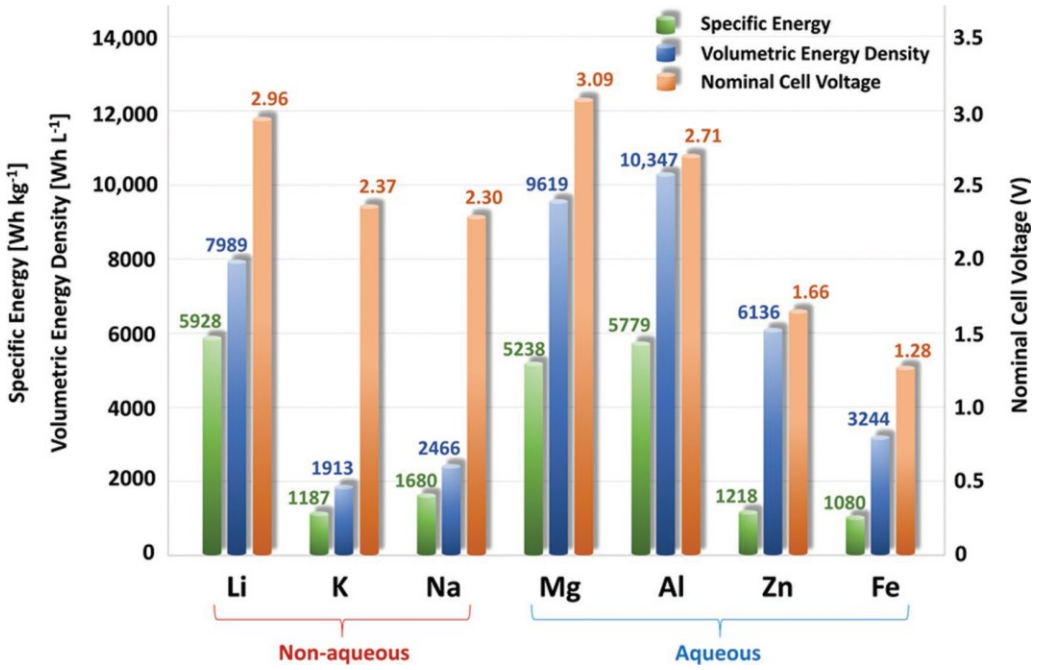

Figure 1-1 Theoretical specific energies, volumetric energy densities, and nominal cell voltages for various metal-air batteries [1].

Zn-air batteries consist of a Zn-metal anode, a gas diffusion layer (GDL) as the air electrode, and an electrolyte. Thus far, primary Zn-air batteries have been used in hearing aids, watches, and other small device applications [1]. Rechargeable (secondary) Zn-air batteries are a more suitable battery storage technology, since oxygen is continually accessible. However, secondary Zn-air batteries suffer from slow reaction kinetics at the air electrode; i.e., the oxygen reduction and oxygen evolution reactions (ORR and OER), respectively. The inefficiencies at the air electrode decrease the potential from the theoretical value of 1.65 V to an operational value of ~1.4 V [6], [7], [8]. Typically catalyst materials, e.g., Pt, Ru, and Ir, are added to the GDL to improve the performance of the cell [6]. There are drawbacks to using precious metals as catalyst materials; these include high cost, short lifetime (unstable), and material scarcity. Other catalyst materials, like transition metals and transition metal oxides, have become more popular alternatives as they are less corrosive than pure carbon and are able to achieve similar catalytic activity to precious metals [6]. Transition metals and their oxides have poor conductivity and tend to be unstable. Nanosizing and combining the materials with carbon materials are approaches that can be taken to mitigate the problems. Despite great advances in creating suitable bifunctional catalysts for the air electrode in Zn-air batteries, further

development of scalable, high-efficiency catalysts is still needed to commercialize rechargeable Zn-air batteries.

This thesis is divided into several chapters. Chapter 2 provides a literature review on ZABs, focusing on cathode materials, microstructural characterization techniques, and electrochemical performance techniques. Chapter 3 investigates different transition metal oxide compositions, combined with N-doped carbon nanotubes (N-CNTs), using the impregnation technique for electrode preparation. Chapter 4 explores the effect that nitrogen and sulfur co-doped carbon nanotubes (N, S-CNTs) have on electrochemical performance when paired with the transition metal oxide catalysts. To conclude the thesis, Chapter 5 will provide a summary of research from each study as well as different paths for future work regarding cathode materials for ZABs.

2.0. Literature Review

2.1. Zinc Air Batteries

ZABs follow the standard battery set up by having four main elements; anode, cathode, separator, and electrolyte. Figure 2-1 shows the typical structure of a rechargeable zinc-air battery and the reactions that take place at each electrode. The anode is Zn metal, the cathode commonly consists of a combination of a catalyst with porous carbon paper which acts as the gas diffusion layer (GDL) to allow for constant supply of air (oxygen), and the electrolyte is usually an aqueous potassium hydroxide solution and is present around the Zn and GDL [2], [4], [9]. Each component will be discussed in further detail in the following sections.

During discharge the Zn metal at the anode is oxidized into zincate ions ($Zn(OH)_4^{2-}$), which then dissolve and precipitate into ZnO. These are the forward reactions in Equation 2-1 and 2-2 [2], [7]. This reaction frees electrons needed to produce OH^- ions at the air electrode, which is the forward reaction of Equation 2-3 [2], [7]. Oxygen is able to diffuse through the GDL due to the pressure difference between the inside and outside of the cell [7]. To charge the cell, the backward or reverse reactions that occur during discharge take place.

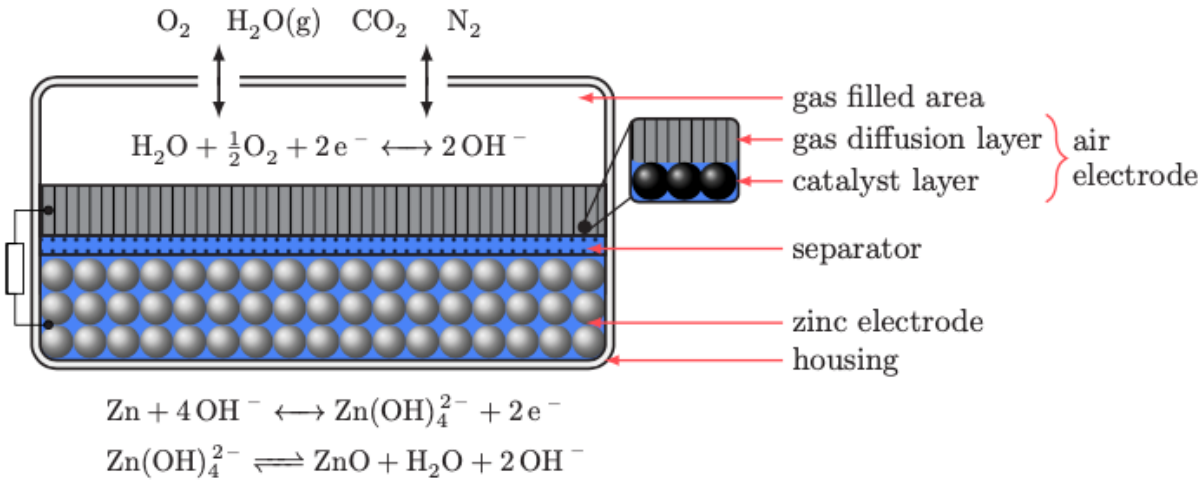

Figure 2-1 Typical Zn-air battery components and reactions [4].

Anode: $Zn + 4OH^- \rightarrow Zn(OH)_4^{2-} + 2e^-$ Equation 2-1

$Zn(OH)_4^{2-} \rightarrow ZnO + H_2O + 2OH^-$ Equation 2-2

Cathode: $O_2 + 4e^- + 2H_2O \rightarrow 4OH^-$ Equation 2-3

2.1.1. Electrodes

The key reactions behind ZABs are redox reactions, which in this case are between oxygen and zinc. Based off this principle there is a zinc electrode (anode) and an oxygen (air) electrode (cathode). The theoretical potential of ZABs is approximately 1.65 V, but they are usually operated between 1.2 V and 1.4 V [2], [6], [7], [8]. The voltage drop that occurs during cycling of the battery is due to different problems at each electrode. These losses are caused by slow kinetics, ionic resistance in the electrolyte, and electronic resistance in the electrodes [2], [7], [10].

Zinc Electrode

The zinc electrode is used in either metal plate or particle form. When used as particles, a paste is usually formed [4], [9]. As previously mentioned, there are losses that occur at each electrode that reduce the potential. The over-potential losses occur due to dendrite growth, shape change, passivation, and hydrogen evolution [1], [9].

Dendrite growth is a serious problem as the dendrites can detach during charging and create a short circuit by coming into contact with the air electrode [1], [11]. Dendrite formation is caused by saturated $Zn(OH)_4^{-2}$ accumulating near the surface of the electrode and then after several cycles a dendritic zinc layer forms [11]. Shape change occurs due to the redistribution of zinc, which causes densification of the electrode and loss of battery capacity [9]. Studies have found that shape change occurs due to uneven current distribution, reaction zones, and convective flow from electro-osmotic forces within the battery [1]. Passivation occurs due to zincate (ZnO) powder, formed according to Equation 2-2, covering the surface of the zinc electrode and acting as an insulator [9]. These insulating properties decrease the conductivity and block the activation sites [11]. The hydrogen evolution reaction (HER) is an unwanted side reaction that occurs at the zinc electrode. It has been found that zinc will corrode when in contact

with aqueous solutions which are commonly used as the electrolyte for ZABs [9]. HER is detrimental in ZABs because it can consume zinc and form hydrogen gas [4], [9]. If zinc is consumed there is less active material for the reactions. The production of hydrogen gas can expand the battery device causing unwanted changes in the battery and eventually cause failure [4].

Several studies have been conducted into alleviating these problems with the zinc electrode. Increasing the surface area of the zinc electrode has been shown to decrease the growth of dendrites, minimize shape change of the zinc, and prevent passivation [9]. Adding additives to the electrolyte and to the electrode are able to minimize HER [9].

Air Electrode

The reaction that occurs at the air electrode is given by Equation 2-3. This reaction enables ZABs to be rechargeable, by either consuming oxygen (discharge) through the oxygen reduction reaction (ORR) or by producing oxygen (charge) through the oxygen evolution reaction (OER) [2], [4], [7], [9]. There are two possible reactions that can occur at the air electrode during the ORR; one involves several steps and the transfer of two electrons per reaction, and the other is a direct reaction involving four electrons transferred. Equations 2-4 to 2-9 show different pathways that occur during ORR in alkaline and acidic solutions. The two-electron pathway (Equation 2-5, Equation 2-6, Equation 2-8, and Equation 2-9) results in peroxide being produced, which is harmful to the battery as it is corrosive and decreases the stability [2], [7]. The four-electron transfer reaction (Equation 2-4 and Equation 2-7) is more direct, leading to higher energy efficiency [2], [7]. This direct pathway is the reaction that is most likely occurring in ZABs and is the most desirable [2], [4], [9].

Alkaline Aqueous Solution	$O_2 + H_2O + 4e^- \rightarrow 4OH^-$	Equation 2-4
	$O_2 + H_2O + 2e^- \rightarrow HO_2^- + OH^-$	Equation 2-5
	$HO_2^- + H_2O + 2e^- \rightarrow 3OH^-$	Equation 2-6
Acidic Aqueous Solution	$O_2 + 4H^+ + 4e^- \rightarrow H_2O$	Equation 2-7
	$O_2 + 2H^+ + 2e^- \rightarrow H_2O_2$	Equation 2-8
	$H_2O_2 + 2H^+ + 2e^- \rightarrow 2H_2O$	Equation 2-9

There are two common OER pathways that occur in an alkaline electrolyte. Both pathways start with the OH^- ions going to the active sites [7]. The first pathway is given by Equations 2-10 to 2-12, where the M – O_{ads} intermediates produce O_2 [2], [7]. The other pathway follows Equations 2-10 to 2-11, and 2-13 to 2-14, where M – O_{ads} reacts with the hydroxide ions to create an M-$OOH_{2,\,ads}$ intermediate that reacts further with OH^- to produce oxygen [2], [7], [6].

$$M + OH^- \rightarrow M - OH_{ads} + e^- \quad \text{Equation 2-10}$$

$$M - OH_{ads} + OH^- \rightarrow M - O_{ads} + H_2O + e^- \quad \text{Equation 2-11}$$

$$M - O_{ads} + M - O_{ads} \rightarrow 2M + O_2 \quad \text{Equation 2-12}$$

$$M - O_{ads} + OH^- \rightarrow M\text{-}OOH_{ads} + e^- \quad \text{Equation 2-13}$$

$$M\text{-}OOH_{ads} + OH^- \rightarrow M + O_2 + H_2O + e^- \quad \text{Equation 2-14}$$

The air electrode consists of a gas diffusion layer (GDL), a catalyst layer (CL), and a current collector [2]. The GDL is typically made up of a porous carbon material (carbon paper) combined with a hydrophobic coating, typically polytetrafluoroethylene (PTFE). PTFE is added to the GDL to prevent flooding, allowing air into the cell and blocking water from exiting the cell [4], [8], [9]. GDL has two layers; the microporous layer and the macroporous layer. The microporous layer is the side that is facing the electrolyte when placed in the battery. This side is also the side on which catalyst material is deposited. There are several techniques for applying

the catalyst to the GDL; the main ones are spray coating, impregnation, and electrodeposition. These methods are further discussed in Section 2.2. Metal meshes are commonly used as the current collectors in ZABs. This is because the metal mesh has pores that allow for ion transport (good conductivity) and mass transport [9]. It is important to have porous materials to increase the number of active sites, since the reaction at the air electrode occurs at what is called the three phase boundary. This is the region where the catalyst, air, and electrolyte are all in contact with one another [2], [9]. Nickel foam is a common current collector used in ZABs, since it has a high surface area which improves the kinetics of the reactions at the air electrode [1], [12].

There are several issues associated with the air electrode, like slow reaction kinetics (ORR/OER), unstable cycling, and flooding [12]. Before rechargeable ZABs can be commercialized and scaled up, these issues need to be resolved. Electrocatalysts have the ability to increase reaction kinetics and stabilize the battery while cycling [12]. Precious metal catalysts, like Pt/Ru, have been used in small scale applications; however, these are costly materials and have poor cycling stability [2]. Recently, transition metals and their oxides have been investigated among other cost effective materials as electrocatalysts for ZABs. These are further discussed in Section 2.1.4.

2.1.2. Separators

Separators, sometimes called membranes, are commonly used in batteries in order to prevent the two electrodes from coming into contact with one another, resulting in a short circuit, while still allowing ion transportation to occur [4], [9], [13], [14]. In ZABs, separators are specifically used to prevent the growth of zinc dendrites and to control the ionic species that are transported between the two electrodes [13]. The ionic species that should be transported between the two electrodes are the OH^- ions [14]. If the Zn^{2+} ions reach the air electrode, the capacity of the battery decreases due to polarization of the air electrode [9], [13]. Separators need to be porous and thin to ensure the hydroxide ions can be sufficiently transported [9]. There are different classes of separators, i.e., porous membranes and polymer electrolyte membranes [14]. Porous membranes are defined as a solid material with a defined pore size (0.2 nm to 20 μm) [14]. Polymer electrolytes, usually made from polyethylene (PE), polyvinyl alcohol (PVA), polyolefin (PO), and polypropylene (PP), use solution-diffusion mechanisms to exclude unwanted ion transport [9], [13], [14]. An acceptable separator material must have the following

properties: appropriate pore size, high ionic conductivity, high stability and adsorption capacity, and high electronic resistivity [13]. Celgard® 5550 is commonly used as a separator material because the structure allows for fast electrolyte wetting [13]. However, the ability for Zn^{2+} ions to pass through to the air electrode is still significant. Anion exchange membranes are a possible solution to polarization of the air electrode, since they are more selective to ion transport [13]. For example, when Celgard® 5550 is coated with an ionic liquid the pore size is decreased limiting the transport of Zn^{2+} ions to the air electrode [13].

2.1.3. Electrolytes

The purpose of the electrolyte is to ensure the transport of ions between both electrodes. Electrolytes have different media in which they can be used; solid, gel, and liquid. The most common form of electrolyte used in ZABs is liquid/aqueous. Important qualities for an electrolyte are good ionic conductivity and no electronic conductivity as the latter can cause the cell to short circuit [15].

Alkaline Electrolytes

Alkaline electrolytes are typically aqueous electrolytes and are most commonly used in ZABs. Alkaline electrolytes are favoured over neutral and acidic electrolytes because they increase the reaction kinetics at the air electrode, provide better zinc-corrosion protection, and are compatible with a variety of electrocatalyst materials [1]. For ZABs, a 6 M KOH-solution is used instead of NaOH because it has a higher ionic conductivity (30 wt% KOH at 620 mS/cm vs. NaOH at 200 mS/cm), lower viscosity, and has a higher solubility for carbonate precipitates (e.g., K_2CO_3 and $KHCO_3$) [4], [6], [9]. Since CO_2 is present in the air, alkaline electrolytes easily form carbonates. Carbonates are detrimental to the life span of the battery as they increase polarization and deposit within the pores of the air electrode [1], [9]. One approach to prevent carbonate formation in the pores of the air electrode is to use a flow cell configuration. Electrolyte is allowed to flow over the electrode thereby removing any buildup of carbonates on the surface [1]. Water evaporation from the alkaline electrolyte is another problem during long term cycling of ZABs [1]. Additionally, altering the electrolyte composition with additives can hinder dendrite formation at the zinc electrode [1].

Gel Polymer Electrolytes (GPEs)

Gel polymer electrolytes (GPEs) contain the aqueous solution within the polymer [16]. There are several advantages to using GPEs over traditional aqueous electrolytes. Flooding and leaking do not occur, dendrite formation at the zinc electrode is decreased, and the formation of carbonates on the air electrode is reduced [16]. GPEs are safe, flexible, and can possess other advantageous properties, making them attractive for a variety of applications. Adding zinc compounds, like ZnO or $ZnCl_2$, to the GPEs with KOH helps decrease the amount of corrosion. It is important to note that if too much ZnO is added, the conductivity of the electrolyte will decrease and passivation can occur earlier [16]. A problem with using GPEs is that there may be poor contact between the electrodes and the electrolytic ions, which decreases cell performance [1].

Ionic Liquids (ILs)

Ionic liquids are composed of salts that have low melting points (< 100 °C). These are called room temperature ionic liquids (RTILs), the majority of which have organic cations [1], [17]. Some advantages of RTILs as electrolytes include high thermal stability, non-toxicity, non-flammability, and a tendency to avoid water evaporation and corrosion [1], [3], [17]. Additionally, since several cation/anion combinations are available, the properties of the electrolytes are tunable [17]. Traditionally, RTILs have low conductivity and high viscosity [1], [17]. However, due to their high viscosity, the transport rate of hydroxide ions is very slow [3], [1], [17]. When RTILs are used in metal-air batteries, the air changes the electrochemical behaviour of the electrolyte causing an increase in conductivity and a decrease in the viscosity [18]. Since RTILs have high thermal stability, ZABs using RTILs could operate at much higher temperatures and increase the reaction kinetics by lowering the thermodynamic barrier [1].

2.1.4. Catalysts

Bifunctional catalysts are needed to help increase the stability and reaction kinetics at the air electrode for both discharge and charge of ZABs [1], [2], [7], [19]. As previously discussed there are two pathways for electron transfer during ORR; two electron transfer and four electron transfer (Equations 2-4 to 2-9) [1], [2], [7]. Four electron transfer is preferred for ORR because there is no peroxide produced which can cause a reduction in catalyst efficiency by poisoning the

catalyst and carbon supports because of its high oxidizability [1]. The reverse of the four electron transfer equation is preferred for OER [2].

Several characteristics need to be considered for an effective bifunctional catalyst. These include catalytic activity, conductivity, selectivity, stability, cost, and environmental impacts [2], [7]. For a material to be considered as having good catalytic activity it needs to increase the number of active sites and reduce ionic and charge-transfer resistances [1]. Heteroatom doping (N, S, P, B) has the ability to change the electronic structure which can improve the catalytic activity [2], [7]. Selectivity is needed to prioritize the production of OH^- ions vs. peroxide ions, so that during ORR four elections are transferred. CO_2 consumption should be limited during OER as well [1]. Figure 2-2 shows the different factors that can be changed to impact the characteristics of the oxygen electrocatalysts in rechargeable ZABs. Precious metals have been used in small scale applications in primary ZABs. In order to scale up ZABs for a range of applications, cheaper, more stable, and more efficient bifunctional catalysts are needed. Transition metals and their oxides, as well as heteroatom doped carbon materials, have become increasingly popular in research. These materials will be further explored in this section.

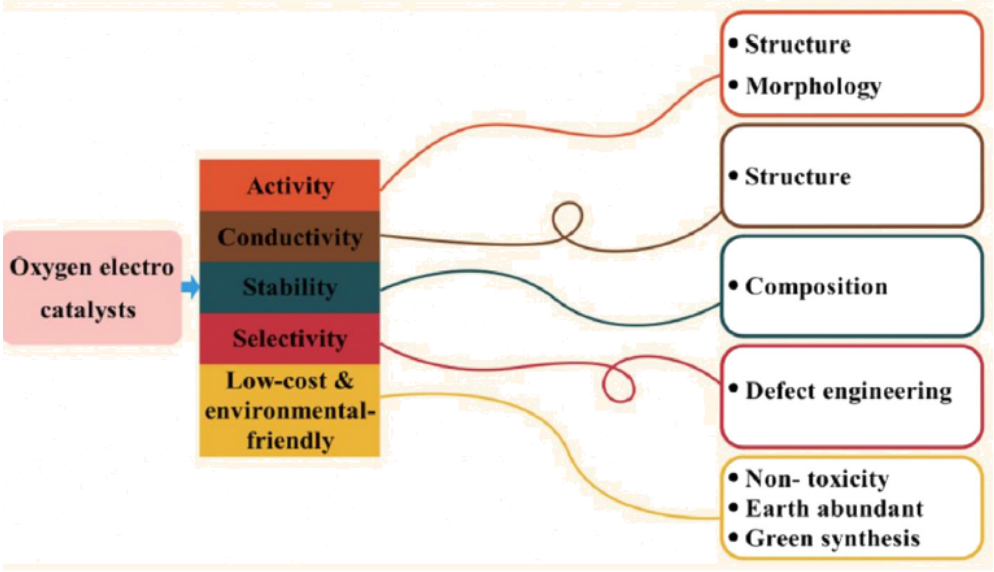

Figure 2-2 Flow chart dictating which factors affect different characteristics for rechargeable ZABs [7].

2.1.4.1. Precious Metals and Alloys

Precious metal catalysts have been used in several applications to increase reaction kinetics in batteries and fuel cells. Pt metal is advantageous for ZAB applications since it has high catalytic activity in alkaline media [9]. Precious metal catalysts when using alkaline electrolyte will follow the four electron transfer path during ORR [1]. Pt is the best noble metal for promoting ORR activity and is most commonly used in commercial applications. Therefore, Pt is used as a benchmark for new ORR catalyst performance testing [1], [2], [7], [9], [13]. IrO_2 and RuO_2 are the best precious metal oxides for promoting OER catalytic activity[1], [2], [7], [9], [13], [20]. Ir oxides have poorer catalytic activity than Ru oxides, but have better stability during operation [9]. With this in mind, RuO_2 is regularly used as the benchmark when comparing new OER catalysts. Bifunctional catalysts are needed for improving ZABs to simplify the manufacturing process. The precious metal catalysts are not bifunctional, so two precious metal-based catalysts are combined for both ORR and OER. Using two precious metals not only increases the cost of the battery, but also complicates the fabrication process since the material compatibility between Pt/C and IrO_2/C or RuO_2/C is low [1], [2], [13]. Noble metal catalysts do not meet the durability requirements for ZABs and the synthesis method for manufacturing the catalysts greatly affects their activity [1], [9].

The cost of precious metal catalysts can be decreased by using nanoparticles of the metals [9]. The surface area will be increased, which will have a positive impact on the catalytic activity, so that less material is required [9]. An obstacle with using nanoparticle precious metals is that the stability and the lifetime of the catalysts, mainly Pt and Ru, will be significantly reduced [21].

Different precious metals, like silver and gold, have also been investigated as possible catalyst materials. Ag-based catalysts have been studied as replacement catalysts for Pt-based catalysts because they are more cost effective (1% the cost of Pt), have high catalytic activity, and good stability in alkaline solutions [9], [19], [22]. Ag-based alloy catalysts, like Ag-Co and Ag-Cu, have higher catalytic activity than Ag alone [19], [22]. Jin *et al.* [19] directly grew a Ag-Cu catalyst on Ni foam which resulted in stable bifunctional cycling stability of ~53% after 100 discharge-charge cycles at 20 mA/cm^2.

2.1.4.2. Transition Metal Based Catalysts

Transition metals (e.g., Mn, Co, Fe, and Ni) and transition metal oxides have been increasingly popular as potential OER/ORR catalysts due to their high abundance in nature, low cost, and high catalytic activity [13], [23]. Transition metals have incomplete d-orbitals meaning they easily accept/donate electrons leading to good redox reactions [6]. However, transition metals are only semi-conductive which leads to poor catalytic activity and poor conductivity [6], [13]. To improve their stability and conductivity they can be combined with nanocarbon materials (e.g., carbon nanotubes (CNTs), graphene, etc.) [6], [13], [22], [23], [24]. Carbon based catalysts will be discussed further in Section 2.1.4.3. A limitation of transition metal based catalyst materials lies in the difficulty of predicting electrochemical results, so much of the research is conducted using trial and error methods [1]. Electrochemical results for transition metal oxides are difficult to predict because their morphology, composition, and electronic structure have significant effects on their performance [9], [13].

The most promising structures are the spinel and perovskite oxide structures, since the metals have multiple valences so they can be electron donors and/or acceptors [1], [13], [25]. The spinel structure (Figure 2-3) has a formula of AB_2O_4, where A and B are metals [13], [25], [26], [27]. The structure is built with tightly packed O^{2-} ions while the A^{2+} and B^{3+} cations fill a fraction or all of the tetrahedral and octahedral positions [13], [25], [28]. Perovskites (Figure 2-4) have a structure of ABO_3, where A is a rare-earth metal and B is a transition metal [13], [25], [26]. An advantage that perovskites provide is that they are more stable and resistant to corrosion than spinels [13], [26]. The B site cations are responsible for and have the most effect on ORR activity [13]. To increase electrical conductivity, chemical stability, oxygen adsorption, and catalytic activity, partial substitution of other cations into the A and B sites can be done [13], [25]. In addition to partial substitution, doping with aliovalent cations can increase the catalytic activity for ORR. It is important to note that the amount of dopant will affect the catalytic properties [13].

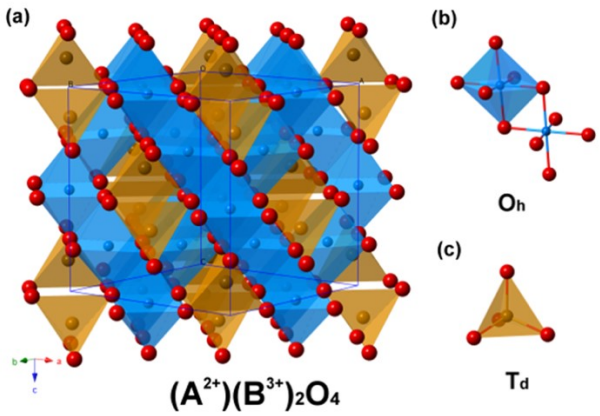

Figure 2-3 Spinel crystal structure [29]. O_h: octahedral sites, T_d: tetrahedral sites.

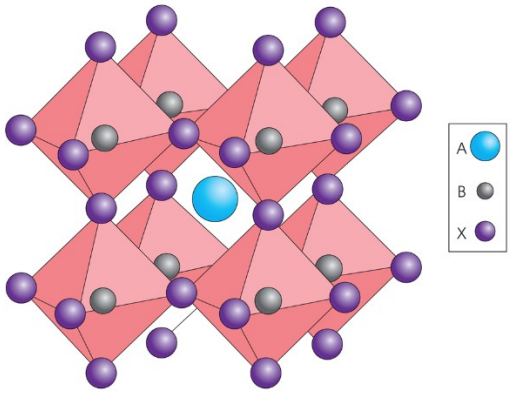

Figure 2-4 Perovskite crystal structure [30].

Cobalt-based oxides have become increasing popular as they have the potential for high activity for both ORR and OER in alkaline environments [25]. Co_3O_4 is a commonly used spinel that is based on a tightly packed FCC structure of the oxygen ions, and comprised of Co^{2+} (one-eighth of tetrahedral A sites) and Co^{3+} (half of the octahedral B sites) ions [25]. The Co^{2+} ions are able to transfer electrons to O_2 molecules to help break the oxygen-oxygen bond while simultaneously oxidizing to Co^{3+}; thus the ORR activity is directly related to Co^{2+} surface ions [25], [31]. The OER activity in Co-based oxides is related to the conversion of Co^{3+} to Co^{4+} before the onset of OER [25], [31]. The activity is affected by the oxidation state on the exposed surface [25]. Several studies show that bimetallic oxides have multiple oxidation states which facilitate redox reactions [32]. It is proposed that Zn and Co oxides have a synergy when combined to make a $ZnCo_2O_4$ spinel, where Zn has a valence of 2+ and occupies the tetrahedral sites, and Co has a 3+ valence occupying the octahedral sites [32], [33]. Huang *et al.* [32]

synthesized porous $ZnCo_2O_4$ rodlike nanostructures for high rate supercapacitors, which had high specific capacitance (605 F/g at 1 A/g) and good cycling stability for 3000 cycles. Xu *et al.* [33] synthesized a Zn-Co spinel oxide on CNTs ($ZnCo_2O_4$/CNT) which had a power density of 249 mW/cm^2 and a potential gap of 1.43 V at 65 mA/cm^2, outperforming Pt/C (221 mW/cm^2 and 1.52 V at 35 mA/cm^2). These studies suggest there is a strong synergy between Zn and Co. $NiCo_2O_4$ has been reported to have better ORR activity than Ni doped Co oxides [25]. $NiCo_2O_4$ possesses an inverse spinel structure, where the A sites are octahedral interstitials and the B sites are tetrahedral interstitials [25]. X-ray photoelectron spectroscopy (XPS) has confirmed that Ni^{2+} ions occupy the octahedral sites, while the Co cations are in both tetrahedral and octahedral sites [25]. It has been proposed that having the Ni cations exposed allows for better oxygen adsorption, thereby increasing ORR performance. OER performance is due to the different valence states of Co, which have a lower potential than Ni, making the OER potential lower than that for NiO [25].

Ni-based oxides are good OER catalysts since they resist corrosion well compared to other oxides [34]. Ni-based catalysts are more conductive than Mn-based catalysts; however, they do not exceed the conductivity of Pt- or C-based catalysts [34]. An advantage that Ni-based catalysts have is that they are more stable than the precious metal based catalysts [34]. The good conductivity is attributed to the Ni^{3+} ions; however, the Ni^{2+} ions have better stability [34]. A problem with the Ni ions is that they move within the crystal structure because of Ni^{3+} reduction to Ni^{2+}, which makes reversibility nearly impossible [34].

A common single transition metal oxide catalyst candidate is MnO_x, because of its low cost, minimal environmental impact, and availability [13], [20], [25]. MnO_2 has several polymorphs resulting in 1D tunnel structures, like α-MnO_2, β-MnO_2, and γ-MnO_2, and 2D layered structures, such as δ-MnO_2, and 3D spinel λ-MnO_2 [20], [25], [35]. Amorphous MnO_x is highly active for ORR because there is a large amount of defects in the lattice [13]. Further analysis of the different polymorphs shows that the ORR activity depends on the crystallographic structure and follows the order α-MnO_2 > β-MnO_2 > γ-MnO_2 [25], [36]. α-MnO_2 has the best ORR activity because the insertion and transfer of ions is likely favoured and there are more defects in the structure allowing for easier adsorption of O_2 [25]. For OER, studies have found that MnO_x with high amounts of Mn^{3+} had good catalytic activity since the bonds are stronger towards OH^-, increasing the generation of MnOOH instead of peroxide formation [13], [20],

[25], [36]. Zhong *et al.* [37] deposited Co onto porous MnO_2 nanosheets (Co-MnO_2). The resulting catalyst material had a maximum power density of 167 mW/cm^2 and a round trip bifunctional cycling efficiency of 63% at 5 mA/cm^2 for 36 cycles (10 min/cycle), which outperformed MnO_2 nanosheets [37].

Fe-based oxides are not usually employed as bifunctional catalysts. With iron oxide catalysts it is difficult to achieve stability and consistent electrochemical results [34]. A Ni_3FeN-supported Fe_3Pt bifunctional catalyst was fabricated and shows comparable linear sweep voltammetry (LSV) results to that of pure precious metal catalysts for both ORR and OER (Figure 2-5). This is promising as the cost is significantly decreased due to the lower amount of Pt.

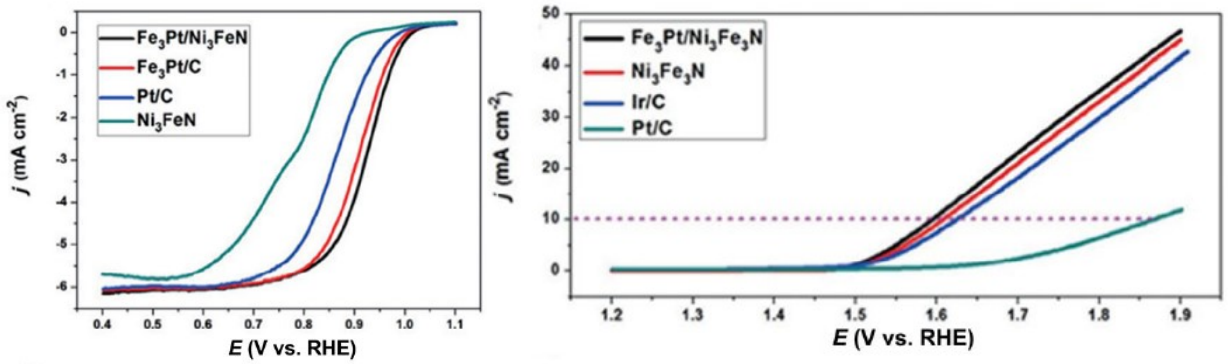

Figure 2-5 a) ORR and b) OER polarization curves for Fe-based catalysts in 0.1 M KOH [38].

Layered double hydroxide (LDH) materials are conducting clay materials that have the formula $[M_{1-x}^{II}M_x^{III}(OH)_2][(A^{n+})_x mH_2O]$; M^{II} and M^{III} are divalent (e.g., Ni^{2+}) and trivalent (e.g., Fe^{3+}) cations, respectively, and A^{n+} is an anion (e.g., CO_3^{2-}) [13]. An advantage to using CO_3^{2-} is that carbonate precipitates will not be able to form at the triple phase boundaries, thereby improving performance of the battery [13]. Recently it was reported that there was no degradation when a CoO/N-CNT hybrid and Ni-Fe-LDH were used as ORR and OER catalysts, respectively [13].

As mentioned above, mixing transition metal oxides has been shown to improve both ORR and OER performance. Adding Fe into the Ni-oxide structure increases the stability of the catalyst and the OER activity is comparable or even better than precious metal based catalysts [34]. There is a synergistic effect between the Fe and Ni ions. Fe inhibits the transition between Ni^{3+} and Ni^{2+} ions, thereby stabilizing the active sites [34]. It was found that by adding more Fe into the catalyst the promotion of Ni^{2+} increased, thus increasing the stability [34]. Iron usually

promotes ORR activity, while Ni promotes OER activity [39]. Guan *et al.* [39] created an Fe-Ni-S-N carbon catalyst (Fe,Ni-SNC) which produced a high maximum power density of 291 mW/cm^2 and excellent bifunctional cycling stability with an overall efficiency of 60% after 140 cycles at 5 mA/cm^2. A spinel Fe-Co oxide on N-doped ordered mesoporous carbon (Fe_xCo/NOMC, where x represents the Fe:Co ratio) was successfully synthesized [40]. The $Fe_{0.5}Co$/NOMC catalyst was found to have a maximum power density of ~230 mW/cm^2 and reasonable bifunctional cycling efficiency of 53.8% after 432 cycles at 5 mA/cm^2 [40]. Wei *et al.* [40] found that the molar ratio of trivalent Fe to bivalent Fe increased as the Co content was increased, and the opposite occurred for Co. The ratio of Co^{3+}:Co^{2+} decreased as the Fe content increased. This observation led to the conclusion that there is a strong electronic interaction between the Fe and Co ions, having a significant impact on catalyst performance.

Spinel structured ferrite nanoparticles are receiving more attention as bifunctional catalysts for metal-air batteries due to their material abundance, low cost, and high catalytic activity towards ORR [41]. As mentioned above, spinel transition metal oxides are paired with a carbon structure to increase their electrical conductivity and stability during electrochemical cycling.

2.1.4.3. Carbon-Based Catalysts

Carbon-based catalysts, like porous carbon, CNTs, graphene, and carbon black, have become prominent in ZAB applications because of their high conductivities, high stability in alkaline environments, high surface area, and low cost [22], [25], [26], [42], [43]. To aid in the cost and environmental friendliness, carbon materials can be derived from biomass waste (e.g., corn silks, leaves, or crab shells) [22], [44]. Since carbon materials are very porous they can work as both a substrate and a mechanical support for the air electrode [22].

Carbon nanotubes (CNTs) have become increasing popular as they are relatively inexpensive, have good thermal stability and conductivity, high strength and toughness, and have good ORR activity by themselves [45]. However, pure CNTs lack the good dispersion, hydrophilicity, and selective adsorption performance needed for practical applications [45]. To improve these properties combining CNTs with other catalyst materials, doping, and/or modifying the surface can be done [26], [43], [45]. A study comparing different types of CNTs showed that multi-walled CNTs combined with the same catalyst material had the best ORR

performance when compared with single walled and double walled CNTs [26]. Carbon materials have a unique structure that allows them to be easily modified [42]. One of the most common ways of changing carbon material structure is through heteroatom (N, S, B, or P) doping [1], [42], [43], [46]. In order to dope pristine CNTs, a functionalization step needs to be done to create binding sites for dopants and metal precursors [26]. Doping nanocarbons with heteroatoms causes defects within the framework. Phosphorous creates defects and delocalizes electrons within the structure allowing for more active sites and improving the electronic conductivity of the nanocarbon [42]. These defects can be advantageous because they have the ability to change either the charge or the spin of the sp^2 carbon plane, which can expedite electron transfer and improve the adsorption of intermediate species [42], [43].

Nitrogen is one of the most common dopants, since the N-doped carbon structure contains n-type doping for electron donation (ORR) and p-type doping for electron acceptance (OER) [42]. Additionally, the size of the N-atom is similar to the C-atom allowing for easy entrance into the lattice of the CNTs [44], [45]. It has been found that N-doping increases the amount of surface defects and the amount of active sites on the CNTs [44], [45]. TEM images show the difference between pristine CNTs and nitrogen doped CNTs (N-CNTs) (Figure 2-6) [46], [47]. The pristine CNTs do not have the bamboo structure that the N-CNTs possess. This is an indication of the defect structure in N-CNTs vs. pristine CNTs [45]. This bamboo like structure is considered to be formed from the recurring formation and spalling of N-doped graphitic layers [45]. Liu *et al.* generated Co-Mn oxide supported on N-doped CNTs that had high stability and a low potential gap (difference between ORR and OER potential) of 0.57 V when cycled for 12 h at 7 mA/cm^2 [48]. Degradation tests were conducted for this material and there was little to no oxidation of the carbon. It is hypothesized that graphitized nanocarbons reduce carbon oxidation and increase corrosion resistance [48], [49]. Wu *et al.* constructed Co/Co_2P heterojunctions confined in N-CNTs, which had a potential gap of 0.72 V and an overall efficiency of 62.5% after bifunctional cycling at 5 mA/cm^2 for 1000 cycles [49]. A maximum power density of around 330 mW/cm^2 was obtained, which compares favourably to that of Pt-Ru/C (158 mW/cm^2) [49]. Mn_3O_4 quantum dots were successfully anchored onto nitrogen doped, partially exfoliated CNTs that had comparable ORR performance and better stability to Pt/C [42].

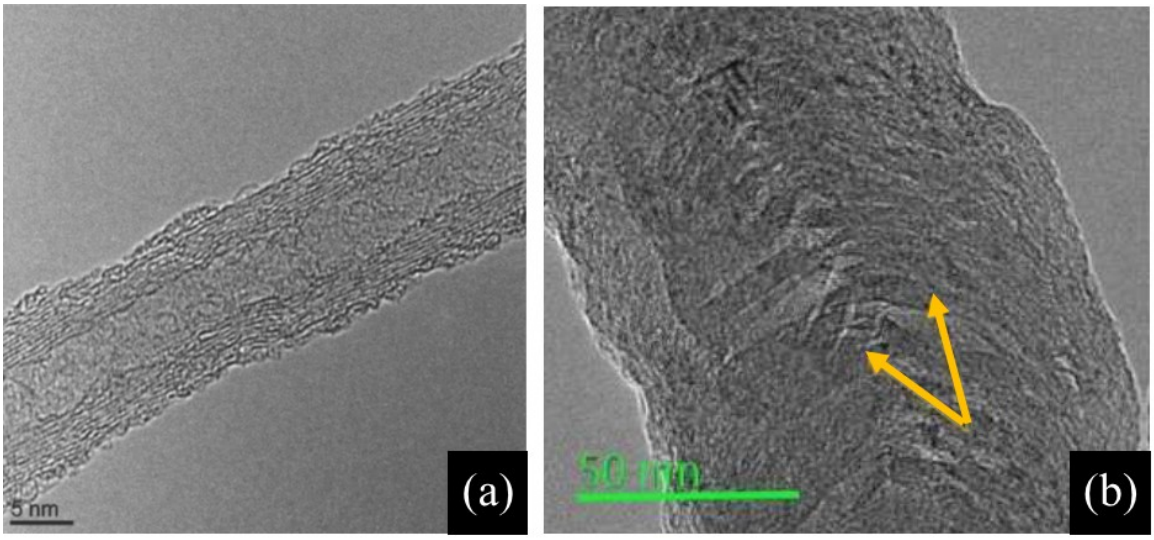

Figure 2-6 HRTEM images of (a) pristene CNTs [47] and (b) N-CNTs [46]. The bamboo structure is indicated by the arrows in (b).

Lanthanum-based perovskites are gaining attention because of their good bifunctional catalytic activity. The formula for the perovskites is $La_{1-x}A_xMO_{3-d}$, where A is commonly Ca, Sr, Mn, Co, or Ba and M is Co, Ni, Mn, Fe, or Ir [13]. A new core-corona bifunctional catalyst (CCBC) was designed using N-CNTs as the corona component and $LaNiO_3$ as the core component, providing excellent ORR and OER performance [50]. It is likely that there is a synergistic effect between the N-CNTs and $LaNiO_3$ components, as degradation and decrease in activity happen after the charging cycle (OER); however, after charging e the discharge cycle (ORR) did not show a significant decrease in catalytic activity [50]. Additionally, the new CCBC catalysts were more stable than Pt/C after 75 cycles [50]. Mousavifar *et al.* tested a $LaCoFe_2O_4$ nano-electrocatalyst on graphene to help facilitate the flow of electrons [41]. LSV testing found that the onset potential at -3 mA/cm^2 was -0.13 V vs. Ag/AgCl in 0.1 M KOH [41]. It is likely that the La-ion in the spinel structure increased the ORR catalytic activity by substituting for the Fe 3+ ions, altering the electrical properties of the spinel structure [41].

Synergistic effects can occur when multiple heteroatoms are co-doped onto nanocarbon materials [42]. Doping nanocarbon materials with one or more heteroatoms (N, S, B, or P) increases the number of active sites, which improves the ORR and/or the OER performance [1], [22], [43], [46]. Several combinations of heteroatoms have been doped onto nanocarbon materials, such as N-S, and N-F-P, with success in increasing battery performance [42], [43]. Sulfur is thought to support maintenance of charge neutrality of carbon, polarization of electron

pairs, and the production of charge positions [44]. Sulfur and nitrogen can fine tune the electronic structure of carbon, promoting both ORR and OER [39], [44]. Not only does doping nanostructured carbon materials with heteroatoms improve carbon ORR/OER activity, but doping can also help anchor metal and metal oxides onto the surface of the carbon material to further increase catalytic activity [42]. CoFe was successfully synthesized onto co-doped sulfur and nitrogen porous carbon (CoFe/S,N-C) [51]. The CoFe/S,N-C material had a half-cell potential gap of 0.661 V vs. RHE and had an overall bifunctional efficiency of ~56.8% for 255 cycles at 10 mA/cm^2, outperforming Pt/C in electrode stability. Wei *et al.* used fish bones as a precursor material for C, N, and S to create N, S co-doped carbon fibers (NSCF) [44]. These carbon fibers were then combined with an Fe-Co-Ni sulfide ((Fe,Co,Ni)$_9$S$_8$/NSCF), which had a maximum power density of 158 mW/cm^2 which outperformed Pt/C + RuO_2 (138 mW/cm^2) [44]. This ternary sulfide on co-doped carbon fibers was also stable and had high efficiency (56%) during bifunctional cycling at 10 mA/cm^2 for 360 cycles [44]. Wu *et al.* [43] synthesized N, F, and P doped porous carbon nanofibers (NFPC), which exhibited stable bifunctional cycling for ~22 h at 10 mA/cm^2 and had an overall efficiency of ~57.5%, outperforming Pt-Ru/C catalysts.

2.1.4.4. High Entropy Alloys

High entropy alloys (HEAs) are composed of four/five or more elements and are single-phase alloys [52], [53], [54], [55]. It has been seen that adding the additional fourth and fifth elements significantly increases the charge transport efficiency, ORR activity, and lowers the OER potential [52], [55]. Additionally, the stability of these five element catalysts is higher compared to precious metal catalysts, and even binary or ternary catalysts [52]. This increase in stability is likely due to the synergistic effect of mixing certain elements together, known as the cocktail effect [52], [55], [56]. It is proposed that the addition of the fifth element may modify the electronic structure, which in turn affects the catalytic activity [52]. Fang *et al.* reported an AlFeCoNiCr catalyst that had a stable ORR and OER potential of 1.15 V and 2.01 V, respectively, during bifunctional cycling at 20 mA/cm^2 in KOH + $Zn(Ac)_2$ (Figure 2-7) [52].

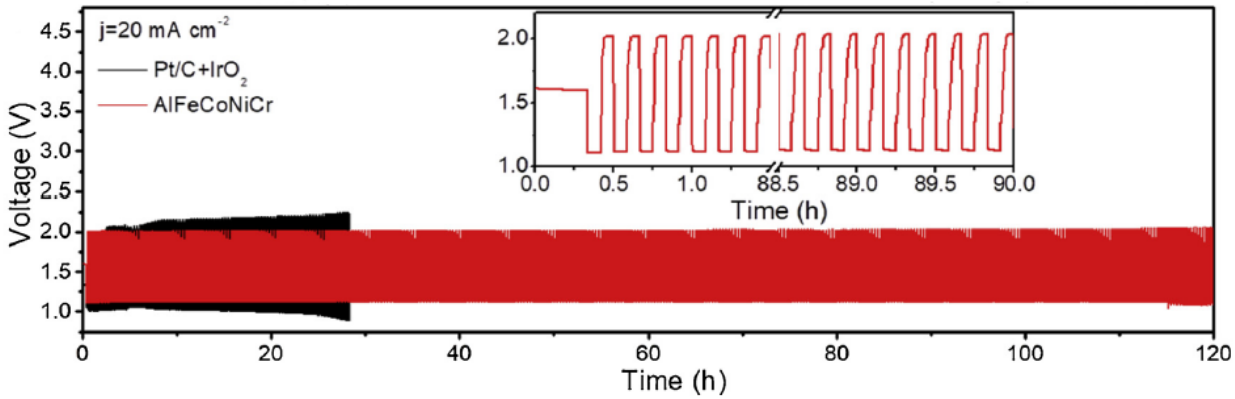

Figure 2-7 Bifunctional cycling test comparison of Pt/C + IrO_2 and AlFeCoNiCr HEA at a current density of 20 mA/cm^2 [52].

Jin *et al.* produced several HEAs, that had better LSV results for both ORR and OER potentials compared to Pt/C and IrO_2 [55]. Figure 2-8 shows a comparison between the precious metal catalysts and the HEAs. AlNiCoRuMo has a smaller potential gap (0.61 V) between the half-wave ORR and OER potentials than the Pt/C-IrO_2-based catalyst (0.68 V) [55]. The smaller potential gap between ORR and OER potentials indicates a more efficient bifunctional catalyst for ZABs.

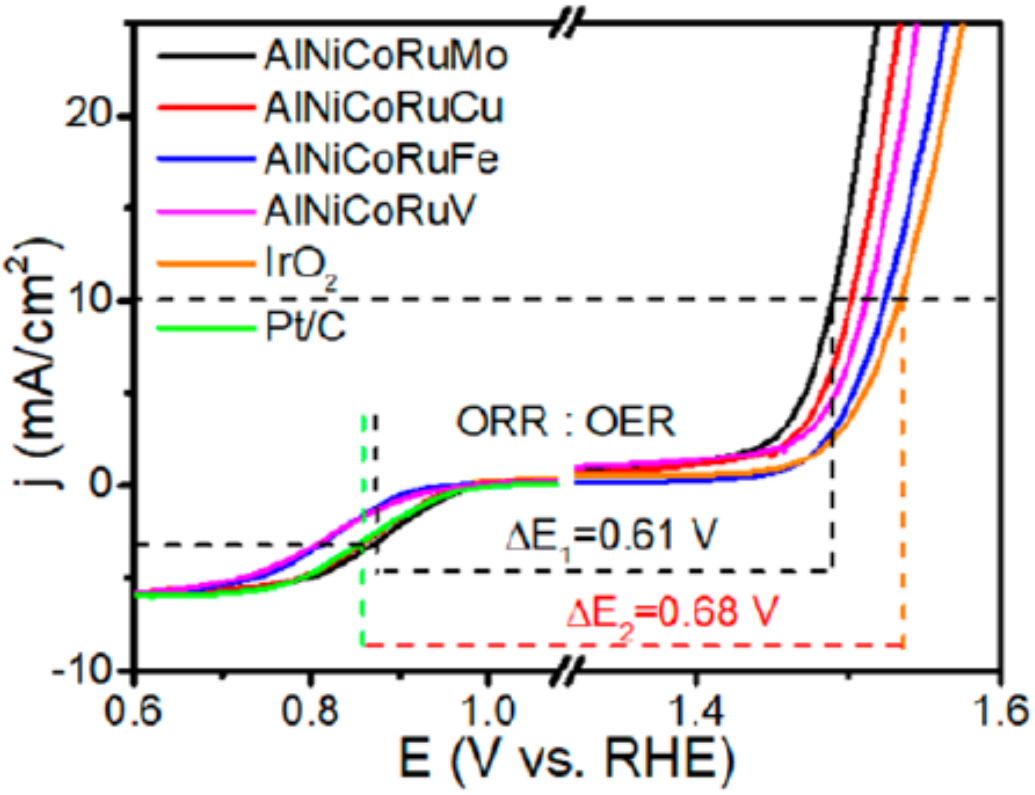

Figure 2-8 Comparison of OER/ORR LSV curves in 0.1 M KOH for different high entropy electrode materials and precious metal based catalysts [55].

Dai *et al.* loaded carbon fiber paper (CFP) with MnFeCoNi HEA powders and conducted LSV tests to investigate the OER performance [54]. They found that the as prepared/milled CFP had worse OER activity than RuO_2, but when activating the HEA powder on the CFP by cyclic voltammetry (CV), OER activity was comparable or even better than that for RuO_2 (Figure 2-9). It was predicted that through the CV-activating process the compound is transformed into a MnFeCoNi oxide, which is more catalytically active [54].

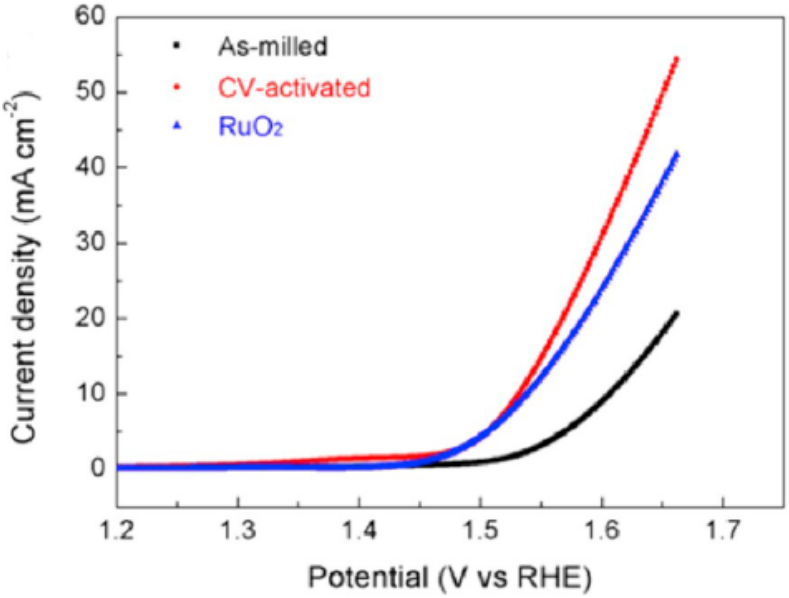

Figure 2-9 ORR LSV curves for MnFeCoNi power, MnFeCoNi on CFP, and RuO_2 in 1 M KOH at a scan rate of 5 mV/s [54].

Li *et al.* [57] investigated several multicomponent spinel metal oxide nanocomposites through chemically de-alloying Al-based precursors. They determined that Mn_3O_4- and $(CoFe)_3O_4$-based oxides are the best oxides for ORR and OER activity, respectively. In this study they found that adding Ni to the precursor alloy with Fe allowed for the benefit of increased OER activity without the negative effects of Fe on ORR activity [57]. The AlFeCoNiMn precursor was used to obtain the $(FeCoNi)_3O_4/Mn_3O_4$ composite, which had a potential gap of 0.7 V and stable bifunctional cycling for 400 h at 2 mA/cm^2 [57].

High entropy oxides (HEOs) are a new classification of material, which like HEAs are single phase and they have five or more cations [56]. Investigation into the defect structure of HEOs has been done, specifically into spinel- and perovskite-structured oxides as they have good catalytic properties [53]. The defect structure affects the transport properties which affects the properties of the compound [53]. HEAs and HEOs have been used as anode materials in Li-ion batteries. Zhao *et al.* prepared a layered nine component HEO as a cathode material for Na-ion batteries that showed stable long-term cycling with little capacity loss [58]. HEAs and HEOs have not been extensively studied as bifunctional electrocatalysts for ZABs; however, they have the potential to be good bifunctional electrocatalysts.

2.2. Electrode Preparation

Electrode preparation is important as it involves addition of the catalyst layer to the electrode. There are several methods for preparation. The most common ones are spray coating, electrodeposition, and impregnation of catalyst material into the GDL. Each method has its advantages and disadvantages. The electrode preparation technique has an effect on the mass loading and consistency of results. This is important when comparing different catalysts as the method could affect the performance.

2.2.1. Spray Coating and Pasting

Spray coating and pasting methods have been popular for fabricating electrodes. These methods entail spraying a catalyst ink on GDL or mixing the catalyst into a paste and spreading it onto the GDL. Binders like Nafion and PTFE are added to the catalyst ink or slurry to ensure there is proper adhesion between the catalyst and the GDL. Zhu *et al.* dispersed N-CNTs into isopropanol, Nafion 5%, and deionized water before spray coating the catalyst ink onto porous carbon paper and then placing it into an oven for 1 h at 80°C [59]. The samples need to be placed in an oven to activate the components. The pasting method is similar to that of spray coating as a carbon, catalyst mixture is needed. Typically, the catalyst material is combined with carbon (e.g., graphite powder) and mixed with a silicon-based product (e.g., silicon oil, and paraffin oil) until a paste is made [60], [61]. The carbon-catalyst paste is then spread to the desired geometry. Despite the simplicity of these methods, it is difficult to maintain continuity in mass loading for different electrodes. Another issue with these methods is that the electrode is highly degradable. This means the catalyst layer loses contact with the electrolyte and air.

2.2.2. Electrodeposition

Electrodeposition (ED) uses an electric current on a conductive material that is submerged in a solution that contains the material to be deposited [62]. ED techniques are useful because they are affordable and are able to uniformly distribute material on complex shapes [63]. Thin films can be produced by controlling the synthesis conditions such as the potential, current density, deposition time, and plating solution [62], [64], [65]. Despite the benefits of electrodeposition, there are problems with this method for electrode preparation. The first issue is that the substrate for deposition must be conductive. The second issue is that low temperatures

are generally used, so the products may be poorly ordered and contain impurities making characterization difficult [66].

Two different techniques are commonly used for ED; galvanostatic and potentiostatic. These two techniques allow for various types of deposits, varying from single metals to alloys and from single layers to multilayers and use direct current (DC), meaning the metallic ions are reduced/oxidized [67]. Galvanostatic deposition has good deposit adhesion since the rate of the reaction (current density) is controlled and is suitable for applications where morphology is not a concern [66], [68]. Potentiostatic deposition is useful for applications that require control over the morphology since the applied potential is controlled [66], [68]. ED is advantageous due to the high level of control over layer thickness, speed of deposition, and accessibility to equipment [66]. In addition, it can be a single-step method for co-deposition [67]. Other commonly used techniques are pulse current (PC) deposition and pulse reversed current (PRC) deposition [67]. PC deposition is done by applying two or more direct cathodic currents at different deposition times. PC is better than DC since there is better control and higher current densities can be used [67]. During PRC deposition, a cathodic current is applied during the "on" time, while an anodic current is imposed during the "off" time [67].

A common practice is to dissolve the precursor (typically metal salts) into the electrolyte bath [63], [64], [65]. Layers with different components can be obtained. Ranjbar-Nouri *et al*. [63] used sequential pulse ED techniques to deposit a protective $CuMn_2O_4$ spinel coating on stainless steel interconnects. The anode used was Pt. Cu deposition was first which consisted of a Cu sulfate + sulfuric acid (H_2SO_4) electrolyte with a pH of 1. The current density applied was 48 mA/cm^2 for 4 min, leading to a layer thickness of ~ 4 µm. To deposit the Mn layer, Mn sulfate + ammonium sulfate + hydroxylamine hydrochloride electrolyte with a pH of 3 was used. A current density of 125 mA/cm^2 was applied for 8 min, resulting in ~ 6 µm thick Mn layer. Xiong *et al.* [69] successfully fabricated a MnO_x/Co-Fe catalyst directly onto porous carbon paper through sequential electrodeposition. First the MnO_x was anodically deposited onto the carbon substrate at a constant current of 40 mA for 10 min from a Mn sulfate, sodium acetate, and sodium dodecyl sulfate electrolyte. A Co-Fe layer was then cathodically deposited onto the MnO_x layer at a constant current of 200 mA for 2 min from a Co sulfate, Fe sulfate, sodium citrate, boric acid, L-ascorbic acid, and sodium dodecyl sulfate electrolyte. The

electrodeposited oxide on the porous carbon paper exhibited strong adhesion and excellent battery cycling stability and efficiency for 40 h in a ZAB [69].

Similar to ED, electrophoretic deposition (EPD) uses similar properties to deposit ceramics and non-metals [64]. EPD involves charged powder particles suspended in a liquid medium with DC applied to the particles so they are attracted to the substrate and are deposited [64]. EPD depends on the charge on the particle and its influence in the solvent when an electric field is applied [64]. This is why it is important to use similarly charged particles and solvents in order to have proper control over the thickness of each layer [64]. Sun *et al.* [70] suspended a $CuMn_{1.8}O_4$ spinel fine powder in an ethanol:acetone solution and successfully electrophoretically deposited (EPD) it onto interconnect plates. The interconnect plates were used as the cathode, a Cu plate was used as the anode, and a constant current of 20 V was applied for 10 min [70]. A drawback to using EPD is that water cannot be used as the solvent due to hydrogen evolution and oxygen gas being formed when a voltage is applied, as this will affect the quality of the deposit [64].

A newer method of ED is to incorporate particles into the deposit. Incorporation of particles into the deposit can be done in using a couple of the aforementioned techniques. PC deposition is commonly used since there is a higher degree of control and higher current densities can be used, allowing for higher concentrations of particles to be incorporated [67]. An advantage to using PRC deposition, is that since there is an anodic pulse, larger amounts of nanoparticles are entrapped. This is due to the partial dissolution of the metallic deposit during these pulses [67]. There are three main problems with this method: 1) There is less than one percent of particle incorporation; 2) particles in the plating bath agglomerate; and 3) particles agglomerate making it difficult to get a uniform coating [67]. These difficulties can be partially alleviated by making the particles more hydrophobic by surface tuning the properties of the particles [67]. Additionally, by combining high speed mechanical stirring and chemical surface modifications the degree of particle incorporation can be increased [67].

2.2.3. Impregnation of Air Electrode

The impregnation technique occurs when the catalyst solution fills the pores of the electrode, leading to catalyst material present throughout the entire electrode. Incorporating the catalyst throughout the porous electrode provides a larger surface area which potentially

increases the electrochemical performance of the air electrode. However, there are limited studies using the impregnation technique.

There are a few different ways the impregnation technique can be carried out. The first is soaking the air electrode (GDL) with the catalyst solution and letting it air dry [71]. Another method is to soak the GDL during sonication and then vacuum filtering the catalyst solution through the catalyst soaked GDL [46]. There are several advantages to using the impregnation technique. As previously mentioned, the catalyst material is present throughout the GDL which improves the reaction kinetics of ZABs. Secondly, it is simpler and gives more consistent mass loading with different catalysts. Consistency is very important in ZABs to ensure the results are comparable and reproducible.

2.3. Microstructural Characterization

The microstructural characteristics of materials used in ZABs is of great interest, as they provide a better understanding of which materials and processing conditions improve battery performance and which are detrimental to it. There are several microstructural characterization techniques, each with their own advantages and disadvantages. Techniques range from light microscopy to electron microscopy. This section will focus on characterization techniques that are commonly used to examine nanosized particles.

2.3.1. Scanning Electron Microscopy (SEM)

SEM is a common imaging technique used in several areas of research, since it is non-destructive, produces high quality images, and has the ability for elemental analysis [72], [73]. The main operating principle of the scanning electron microscope involves emission of a beam of electrons (energies from 1-30 keV) at a specimen's surface and then analyzing the signals produced from this process. Each signal is produced by interacting with different depths of the specimen (Figure 2-10) [72], [74]. The main signals analyzed when conducting SEM are secondary electrons (SEs), backscattered electrons (BSEs), and characteristic X-rays [73], [75], [76]. SEs are produced by inelastic scattering and have energies lower than 50 eV, while BSEs are primary electrons that have undergone elastic scattering at angles between 90º-180º [72], [75]. SEs only escape from the near surface region of the sample (less than 1 nm), so they can

reveal topographic information with a spatial resolution between 1 and 10 nm [72], [75]. BSE electrons primarily provide atomic number contrast, since they are produced through Rutherford scattering which is influenced by the number of protons in the nucleus [72], [75]. Characteristic X-rays are emitted when an inner shell vacancy is produced by an incoming energetic electron and an outer shell electron moves into the inner shell. The energy released during the transition can be in the form of an X-ray, which will have an energy characteristic of the element involved [75], [77], [78]. Energy dispersive X-ray (EDX) spectrometry is used to analyze the characteristic X-rays to determine the near surface chemical composition. EDX analysis typically has a spatial resolution of ~1 μm, but this will depend on the electron beam energy and sample composition. This process involves separating the X-rays in terms of energy [72], [79]. The different energies are grouped and compared with standard energies of specific elements and used to create an EDX spectrum [72]. The EDX spectrum shows the number of X-rays collected at different energies. The EDX spectrum defines each characteristic X-ray peak in terms of the inner shell vacancy; i.e., the shell corresponding to the X-ray and the intensity of the line within that group [78].

Figure 2-11 shows a typical layout of an SEM. The electron source, often called the electron gun, is the source of electrons and controls the energy of the beam. Electron guns (electron source) need to provide a stable beam with high current, a small spot size, adjustable energy, and small energy dispersion. There are three main types of electron guns: tungsten "hairpin" guns, lanthanum hexaboride (LaB_6) guns, and field emission (FE) guns. The best resolution images are produced from FE guns, followed by LaB_6 guns, and lastly tungsten guns [73], [75]. The electron beam travels through several lenses before impacting the specimen; the lenses reduce the beam size and focus the electron beam [76]. There are several detectors and other equipment used for analysis of topology, chemical composition, and microstructural characteristics of the specimen [75], [76].

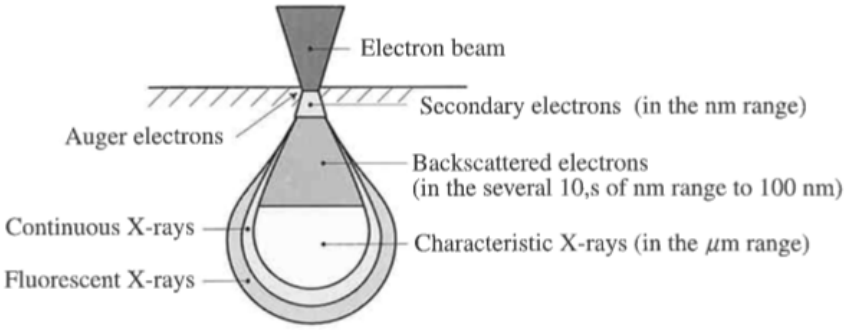

Figure 2-10 Depth of generation of different signals [74].

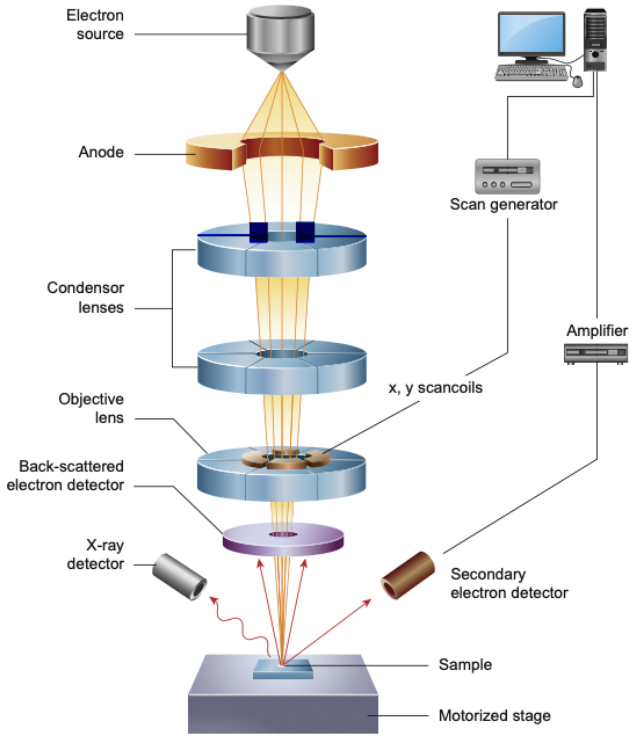

Figure 2-11 Typical SEM layout [72].

2.3.2. Transmission Electron Microscopy (TEM)

Transmission electron microscopy (TEM) is similar to SEM; however, the electron beam is operated at higher energies to allow for full specimen penetration, which allows the transmitted electrons to be used for imaging and diffraction patterns. The usual electron energy is between 80 and 300 keV [72], [77], [78]. Since the electron beam can penetrate through the specimen, internal microstructure can be observed. Figure 2-12 shows the typical the components of a TEM. Much like the SEM, a TEM has several lenses that the electron beam

passes through. Transmission electron microscopes (TEMs) have more lenses than SEMs since they are needed above and below the specimen stage used to control the diameter, convergence, and focus for both the incident electron beam and transmitted electrons [72], [78]. Scanning transmission electron microscopes (STEM) have an extra coil that scans the electron beam over a localized area of the specimen. The improved spatial resolution is attributed to the smaller interaction volume with the thin samples versus the bulk samples used in SEM [72], [77]. There are different imaging modes for TEM/STEM; e.g., bright-field (BF) imaging, dark-field (DF) imaging, high-resolution TEM (HRTEM) imaging, and high angle annular dark field (HAADF) imaging. BF images are produced in TEM mode from the unscattered electrons, while DF images are produced in TEM mode from specific scattered electrons [72], [78]. HRTEM can be achieved on ultra-thin samples (<<100 nm) since the majority of scattering is elastic scattering. These high resolution images are able to show atom positioning at magnification exceeding 400 kX [72]. STEM annular dark field (ADF) images are able to display atomic number effects with atomic resolution [72]. Different techniques are used to analyze the crystal structure and chemical composition of the specimen during TEM: electron diffraction and EDX analysis, respectively. Selected area diffraction (SAD) is one type of electron diffraction. There are two main types of SAD patterns; ring patterns and spot patterns [78]. Ring patterns are produced from multiple grains, while spot patterns are formed from single crystals [77], [78]. Single crystal patterns can also be used to determine crystal orientation [78].

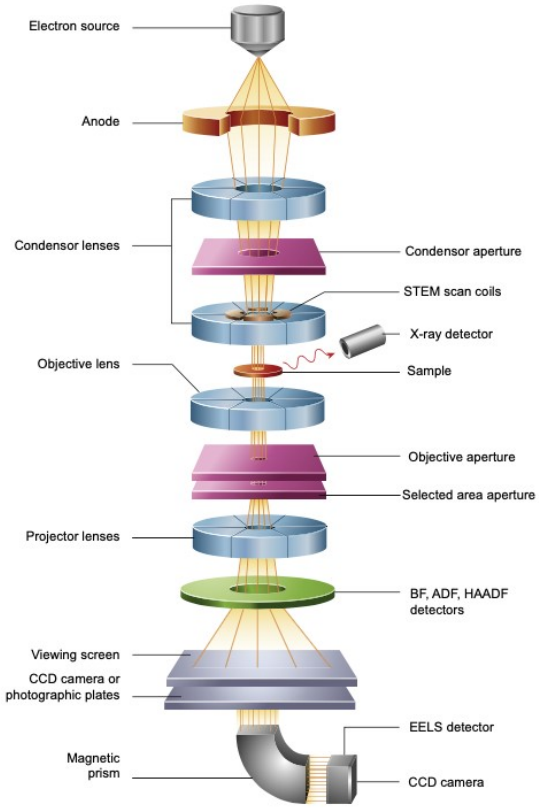

Figure 2-12 Typical TEM setup [72].

2.3.3. X-ray Photoelectron Spectroscopy

X-ray photoelectron spectroscopy (XPS) is commonly used to analyze surface elemental composition and provide chemical bonding information. Photoelectrons are produced when the incoming photon beam causes the ejection of an electron (Figure 2-13) [80]. XPS is specific to the surface of each specimen, and determines the concentrations of each element to about 0.1% accuracy, while being non-destructive (beam penetration between 1-100 μm) [81], [82]. Even though the X-ray beam can penetrate deeply into the specimen, the electrons that provide chemical bonding and composition information are emitted within ~10 nm of the surface [81], [83]. A limitation with XPS is that it does not have the ability to detect H or He due to their low atomic numbers. H and He cannot be detected as their photoionization cross sections are too small [84], [85]. For perspective, the H photoionization cross section is ~5000 times smaller than that for the C 1s orbital [85].

The technique measures the kinetic energy of photoelectrons that are given off when a beam of X-rays interacts with the atoms near the specimen surface. The kinetic energy data collected is used to determine the binding energy of the electrons within the specimen. By

subtracting the kinetic energy of the photoelectron from the energy of the photon (incoming X-ray beam), the binding energy of the specimen is determined [81]. Along with photoelectrons, Auger electrons can also be emitted. Auger electrons are produced when an electron leaves the orbital (causing the atom to become unstable) and undergoes a relaxation process (Figure 2-13) [80], [81]. Each photoelectron and Auger electron is sorted in terms of kinetic energy; however, the data is typically plotted as electron intensity vs binding energy in an X-ray photoelectron spectrum. The composition of each element is proportional to the area under the peak (intensity of the peak) [81].

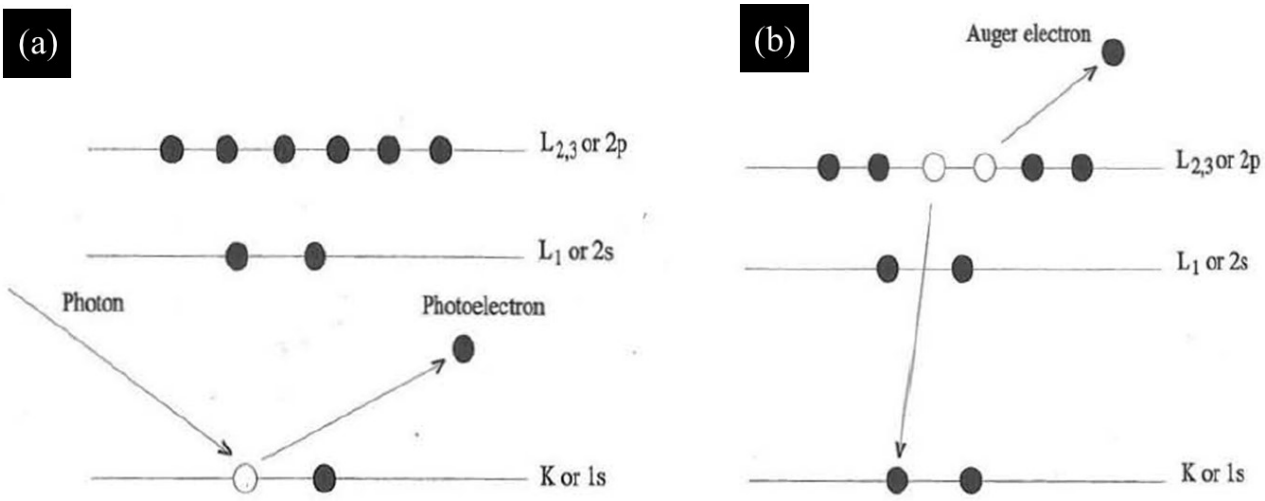

Figure 2-13 Photoelectron and Auger electron emission process [80].

A special feature of XPS analysis is the ability to determine the bonding state of each element in the specimen. The bonding state is determined by the characteristic features of the XPS spectrum; i.e., peak position, multiplet splitting, and satellite structure [83]. These characteristic features of the spectrum are compared to standard reference materials provided by the National Institute of Standards and Technology (NIST) of the USA. The chemical shift, and differences between the peak position of the obtained spectrum and the reference material depend on the oxidation state of the atom [81]. There are also smaller peaks (satellite peaks) included in the spectrum; these are caused by multiplet splitting and shake-up satellites. Multiplet splitting is due to unpaired electrons in the core and unpaired electrons in the valence shell coupling [80]. Shake-up satellites are caused by an electron within that atom moving to a higher energy level, which causes an overall decrease in the kinetic energy of that atom [83]. In an XPS spectrum, there is also background noise due to scattered photoelectrons [83].

2.3.4. Carbon, Hydrogen, Nitrogen, Sulfur (CHNS) Analysis

CHNS analysis is performed at high temperature (>800 °C) in an oxygen rich environment in order to combust the elements. Combustion leads to carbon conversion to carbon dioxide, hydrogen conversion in water, nitrogen conversion into nitrogen gas or nitrogen oxides, and sulphur conversion to sulphur dioxide [86]. The products of combustion are removed from the combustion chamber by an inert gas and passed over copper at ~600 ºC. The copper at the bottom of the chamber removes any residual oxygen from the combustion process and converts any nitrogen oxides into nitrogen gas [86]. Analysis of the gases can be done in several ways: 1) Gas chromatopgraphy (GC) coupled with thermal conductivity detection; 2) frontal chromatography coupled with thermal conductivity detection for CHNS; and 3) infra-red with thermal conductivity for individual element detection [86].

2.4. Electrochemical Testing

Electrochemical testing is important in assessing the performance of catalyst materials. By understanding the reaction mechanisms for charge transfer, mass transport, and electron transport, better electrocatalyst materials can be developed. There are several electrochemical testing methods. The ones that help determine the performance of ZABs are explained further in this section.

2.4.1. Linear Sweep Voltammetry (LSV) and Cyclic Voltammetry (CV)

Linear sweep voltammetry (LSV) and cyclic voltammetry (CV) follow very similar processes. These methods can be referred to as half-cell testing and are done with a three electrode configuration; reference, working, and a counter electrode. LSV is useful for determining reaction kinetics for ORR and OER, while CV investigates the surface reactions beyond ORR and OER (e.g., chemical reactions at the surface, rate limiting factors, etc.) [87]. In simpler terms, LSV curves indicate which catalysts are best for ORR and OER and CV curves provide information into the chemical reactions [88]. Both methods linearly vary potential with time, known as the scan rate ν, between two potentials E_1 and E_2 [88], [89], [90]. The difference between LSV and CV is that during CV testing once E_2 is reached the process is reversed until E_1 is reached again. After E_1 is reached the test can either be stopped, reversed back to E_2, or continued to another potential, E_3 [88]. The amount of cycles done during CV range from one to

several; there is no set amount. The scan rate used can vary, scan rates from 10 mV/s to 1000 V/s being typical [88], [90]. A drawback to using high scan rates is that double-layer charging as well as iR effects become significant [88], [90]. The peak positions give information regarding the type of reaction. If too high a scan rate is used, the results of a reversible reaction can mimic those of an irreversible reaction [90].

Figure 2-14 shows typical CV curves with different scan rates. There are two peaks, corresponding to positive and negative current. These peaks represent reactions in the electrode, usually termed oxidation and reduction peaks. The peak occurring in the positive y-axis is the oxidation peak and the peak occurring in the negative y-axis is the reduction peak. The scan rate effects the amplitude of the oxidation and reduction peaks as shown in the figure. Slower scan rates broaden the peak meaning the reactions occur at steady-state allowing the diffusion layer to reach equilibrium [87], [88]. Higher scan rates do not provide enough time for the diffusion layer to reach equilibrium which is why higher currents are needed [87], [88]. The CV peaks are also affected by scan rate. The peak positions do not change with scan rate when the reaction is reversible. However, for quasi-reversible and irreversible reactions, the peak positions do shift as a result of the relationship between electron transfer and mass transfer [88], [90]. In the case of irreversible reactions, there will only be one peak.

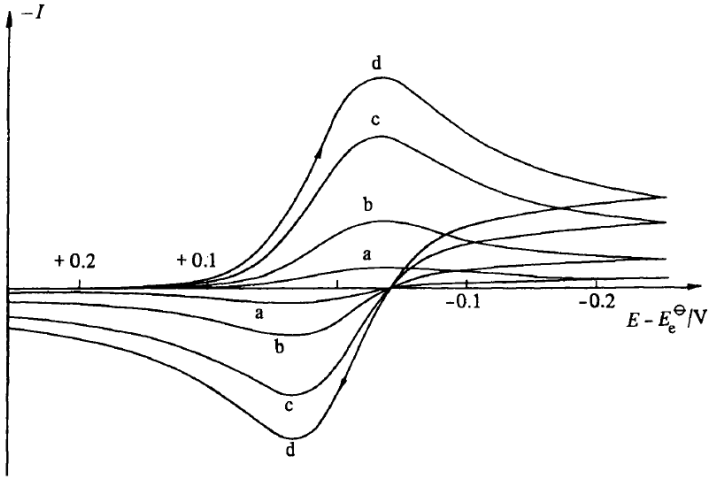

Figure 2-14 CV curves for a reversible reaction at different scan rates. a) ν, b) 10 ν, c) 50 ν, and d) 100 ν. [88].

Typical LSV curves for ORR are shown in Figure 2-15a, and typical curves for OER are shown in Figure 2-15b. The region where the slope of the LSV curves start to change is called

the onset potential. This potential marks where the kinetic reactions stops and the diffusion controlled reaction begins. A smaller overpotential is beneficial for both ORR and OER LSV curves.

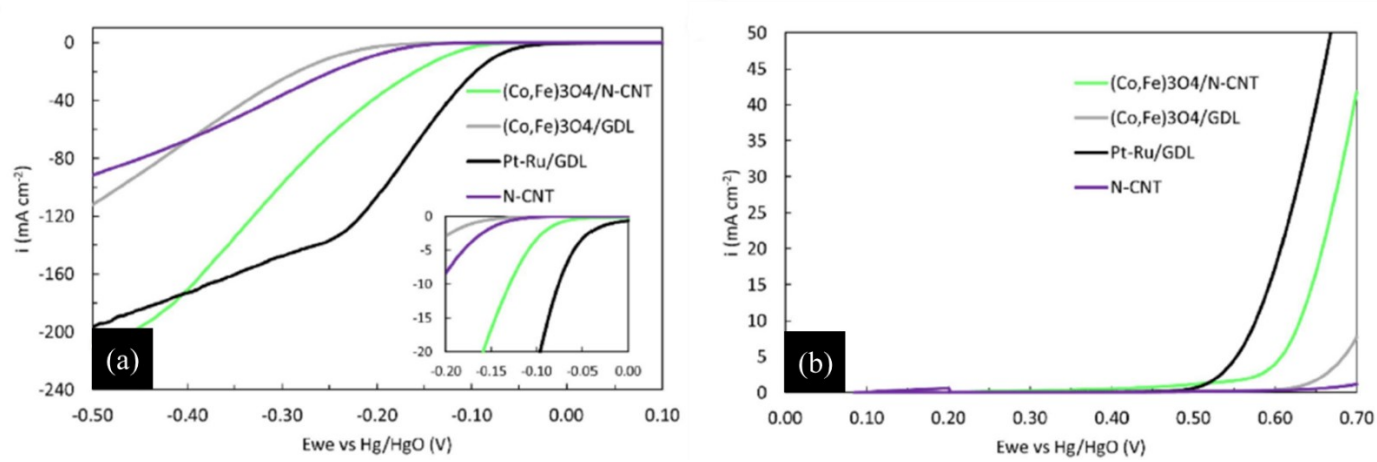

Figure 2-15 LSV curves for Co-Fe oxide catalysts, Pt-Ru, and N-CNTs (a) showing ORR catalyst activity and (b) OER catalyst activity. Testing was done in O_2-saturated 1 M KOH at a scan rate of 5 mV/s [91].

2.4.2. Electrochemical Impedance Spectroscopy (EIS)

Electrochemical impedance spectroscopy (EIS) measures the change in impedance at the electrode-electrolyte interface [87], [89], [90], [92]. EIS also provides insight into conductivity, charge transfer properties, and properties of the passivating layer [92]. The process of EIS is conducted by applying an AC signal to an electrochemical cell, which results in a current expressed by its amplitude and phase angle [87], [89], [90], [92], [93]. Using Ohms law (Equation 2-15) the impedance, Z, is calculated [87], [89]. Either a two- or three-electrode cell configuration is used to perform this test [93]. However, a limitation to the two-electrode set-up is that it may not incorporate the processes that occur in a full-cell battery at different stages of the charge/discharge process [93].

$$Z(\omega) = \frac{E}{I} \qquad \text{Equation 2-15}$$

The graphical output of EIS is called a Nyquist plot (Figure 2-16), which consists of two regions; high and low frequency. The semicircle portion of the plot corresponds to the charge transfer resistance, R_{ct}, which is in the kinetic controlled region (high frequency) [87], [90], [93]. The diffusion of ions between the electrolyte and electrode, also known as Warburg impedance,

Z_w, is the straight line within the mass transfer controlled region (low frequency) [87], [90], [93]. For ZABs the x-axis intercept (impedance is zero) in the high frequency region is of interest as it gives the resistance between the electrolyte and the electrode [87]. The smaller the semi-circle, the lower the charge transfer resistance, which indicates a more promising catalyst.

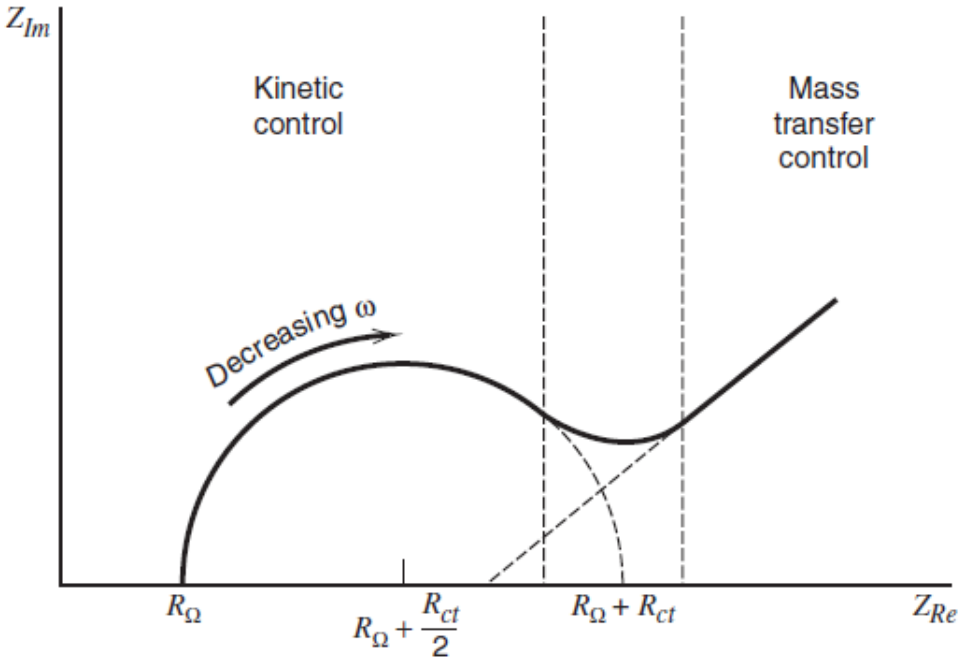

Figure 2-16 Impedance plot for EIS outlining the kinetic and mass transfer reigions [90].

2.4.3. Chronopotentiometry (CP)

The chronopotentiometric (CP) technique investigates how the potential responds to different applied currents [89]. Unlike the electrochemical techniques presented earlier, CP techniques are performed using a full-cell battery configuration. CP techniques are used to evaluate the battery as a whole, while LSV and CV tests evaluate the effectiveness as a catalyst. The current can be applied in various ways. The first way is applying current in a step wise manner; i.e., holding the current at a constant value. This method is commonly referred to as rate testing, since the potential stability is shown for a certain amount of time at a specific current (Figure 2-17a) [87]. A second approach is to linearly increase the applied current. This second method often results in polarization curves which can then be used to determine the power as a function of current (Figure 2-17b) [87]. The last two methods of CP either cycle the current or reverse the current and will be furthered discussed in the next section.

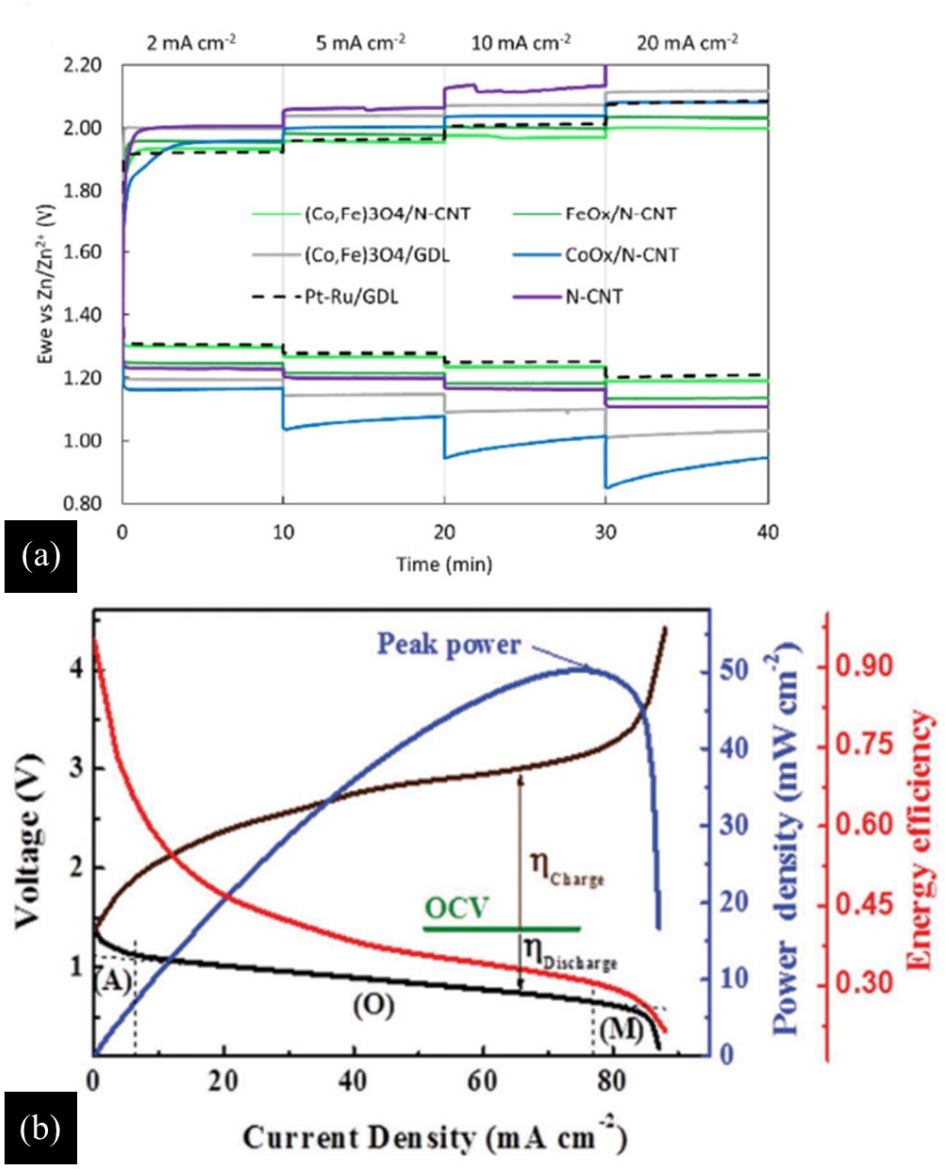

Figure 2-17 CP curves for (a) Co-Fe oxides, Pt-Ru, and N-CNT electrodes battery rate tests at varying current densities [91] and (b) discharge/charge polarization and power density as a function of current of a typically rechargeable zinc-air battery [1].

CP methods are beneficial when dealing with ZABs and are used in a full cell battery configuration. Rate tests are often used to assess the battery performance at different current densities, e.g., stability at specific current density. The efficiency at each current density can be determined by dividing the discharge (ORR) potential by the charge (OER) potential. Polarization curves are used to gauge how much the battery's operating potential differs from the open circuit voltage (OCV) under changing currents [1]. The difference between the

operating potential (charge/discharge potential) and the OCV represents how much potential is lost due to activation, mass-transfer, or Ohmic losses [1]. The energy barrier (activation losses from oxygen reactions) make up the majority of the losses in ZABs, and can be seen as the initial steep reigion on the polarization curves [1]. The Ohmic losses are due to the resistance within the electrolyte, while the mass-transfer losses are due to the limited amount of reactants at the electrode at the end. As previously mentioned, linearly increasing the applied current can produce polarization curves which allow the maximum power output to be determined. Power is calculated by multiplying the absolute value of current by the output potential. Knowing the maximum power output of the cell as well as the stability of the electrodes is useful when comparing electrodes and different types of batteries. Thus, CP is a useful technique for evalutating the performance of ZABs.

2.4.4. Galvanostatic Charge-Discharge (GCD)

Galvanostatic charge-discharge (GCD), also called galvanostatic cycling or bifunctional cycling, is based on chronopotentiometry (CP) and provides information about stability during cycling of the battery [87]. GCD alternates the current between a positive and negative value for a set amount of time. The testing configuration used is a full-cell battery. During GCD, a cycle consists of one charge and one discharge cycle at a specific charge/discharge current density (Figure 2-18) [87]. The test parameters (number of cycles, length per cycle, current density applied, etc.) need to be determined. There are two common cycling tests performed for ZABs. The first one includes short cycle lengths but a large amount of cycles, and the second uses longer length cycles but a smaller amount of cycles. The limitation to using the first cycling test is that only a fraction of the total capacity of the zinc-electrode is used [1]. The second cycling test is more applicable for evaluating ZAB performance, since the length of the cycle is long enough to use both the air electrode and Zn electrode capacitance [1].

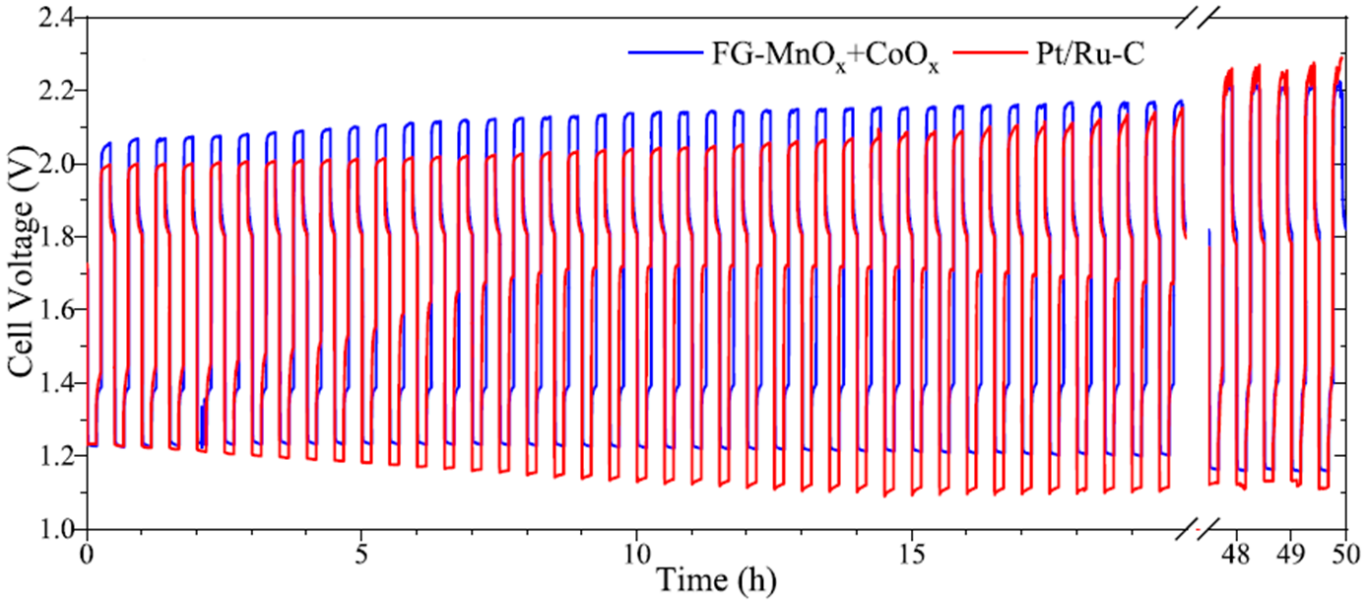

Figure 2-18 Bifunctional cycling of batteries with a Pt/Ru-C catalyst and a MnO_x-CoO_x catalyst, fabricated by atomic layer deposition (ALD) using forming gas plasma, at 10 mA/cm^2 for 100 cycles in 6 M KOH + 0.25 M ZnO [94].

Unfortunately, there is no standard for these parameters, so comparing different electrodes and batteries is difficult if different testing conditions were used. Due to the lack of standard testing procedures, precious metal catalysts, like Pt or RuO_2, are used to compare cycling results [7]. Typically initial and final efficiencies, the difference between the ORR and OER potentials, and the overall battery stability are compared. GCD is a good technique for evaluating the battery performance (e.g., degradation, and stability) under different parameters that best suit the intended application.

2.5. Summary

Zinc-air batteries (ZABs) are a promising technology due to their safe operation, environmental friendliness, and high theoretical energy density. Although ZABs have high theoretical energy density, the slow reaction kinetics at the air electrode decrease the operating potential. Throughout this review, several catalyst materials were reviewed; e.g., precious metals, transition metals and their oxides, and nanocarbons. These catalyst materials have one or both of two problems; i.e., low cycle life (<1000 cycles) or poor efficiency (<70%). Different electrode preparation techniques were compared. Among the methods, the impregnation

technique is a promising method since the catalyst material can be deposited within the GDL which assists in generating the three phase boundary layer. Additionally, a range of microstructural characterization and electrochemical testing methods were discussed that will aid in evaluating the performance of ZABs. The durability and efficiency of ZABs need to be improved for them to compete with the Li-ion batteries that currently dominate the market.

3.0. Tri- and Tetra-Metallic Oxides Anchored to Nitrogen Doped Carbon Nanotubes as Bifunctional Electrocatalysts for Rechargeable Zinc-Air Batteries

A version of this chapter has been submitted to the Journal of Applied Electrochemistry (July 2021).

3.1. Introduction

Traditional, non-renewable energy sources (e.g., oil and natural gas) are harmful to the environment, which has generated increasing interest in renewable energy sources. Renewable energy sources, like wind turbines and solar cells, are being increasingly implemented, but they provide intermittent power so that reliable and efficient energy storage devices are needed. Rechargeable Li-ion batteries are the most commonly utilized energy storage devices, since they have high efficiencies and high energy densities; however, there are several issues with these batteries. They can be unsafe during operation and have their own environmental issues due to the mining practices employed to extract Li and disposal of spent batteries. A promising alternative is metal-air batteries and more specifically rechargeable zinc-air batteries (ZABs). ZABs are safe, environmentally friendly, cost effective, and have a high theoretical energy density (1353 Wh/kg) [7], [9]. Zinc is also abundant [7], [9]. Nevertheless, there are drawbacks associated with ZABs. The oxygen reduction reaction and oxygen evolution reaction (ORR/OER) kinetics at the air electrode are slow and battery stability during cycling is poor [9], [7]. To improve the ORR and OER kinetics, catalysts are added to the air electrode. Precious metals, like Pt, Ru, and Ir, enhance the ORR and OER kinetics, but they inhibit large scale application due to their significant cost, material scarcity, and poor cyclability [13], [21], [57]. This has led to investigation into low cost, alternative bifunctional electrocatalysts.

Transition metal oxides (TMOs), based on metals such as Mn, Co, Ni, and Fe, are attractive alternatives to precious metals as they are less costly, abundant, and possess high catalytic activity [13], [22], [57]. Many TMOs form a spinel oxide structure (AB_2O_4, where A and B are metals with 2+ and 3+ cations, respectively) which is stable in alkaline electrolytes [13], [25],

[26]. Mn-based and Co-based oxide spinels are good ORR catalysts since they possess variable valence states and coordination structures [57]. NiFe-, CoFe-, and NiCoFe-based spinel oxides are well known OER catalysts [57], [95], [91]. However, TMOs suffer from poor electronic conductivity. To enhance the conductivity, TMOs can be coupled with nanocarbon structures, like carbon nanotubes (CNTs), carbon black (CB), and graphene [33], [37], [46], [95]. Additionally, doping the carbon structures with heteroatoms (e.g., N, S, P, and B) can increase the number of active sites available for the TMO catalyst, thereby improving the ORR and OER performance [22]. Since N-doped carbon structures exhibit both n- and p-type doping, which benefit ORR and OER respectively, nitrogen is most commonly used [42]. Huang *et al.* [42] created Mn_3O_4 quantum dots anchored onto nitrogen-doped carbon nanotubes (N-CNTs) that had better stability and comparable ORR performance to Pt/C. Another group used N-CNTs as a support for Co-Mn oxide that had a potential difference of 0.57 V (between the ORR and OER potentials) after 12 h of cycling at 7 mA/cm^2 [48]. A smaller potential difference corresponds to a more efficient battery.

Wang *et al.* [96] fabricated Co-Mn-Ni ternary spinel nanorods through a co-precipitation and annealing method. The resulting air electrode had a potential difference of 0.88 V and a round trip efficiency (ratio of the ORR potential to the OER potential) of 57.4% for 100 cycles at 10 mA/cm^2. The stability was improved relative to similar batteries with Pt/C electrodes. Zhong *et al.* [37] modified MnO_2 nanosheets with Co, Ni, and Fe. The results showed that Co-MnO_2 (ΔE= 0.95 V) and Ni-MnO_2 (ΔE=1.01 V) had comparable LSV potential differences to Pt/C + IrO (ΔE= 0.88 V). Lu *et al.* [97] fabricated several tri-metallic spinel oxides with the composition $M_{0.1}Ni_{0.9}Co_2O_4$, where M = Mn, Fe, Cu, Zn. Among these tri-metallic oxides, $Fe_{0.1}Ni_{0.9}Co_2O_4$ (FNCO) had the best bifunctional results with a discharge potential of 1.18 V and a charge potential of 2.03 V (58% efficiency) when cycled for 95 cycles at 10 mA/cm^2. $Mn_{0.1}Ni_{0.9}Co_2O_4$ (MNCO) and $Zn_{0.1}Ni_{0.9}Co_2O_4$ (ZNCO) had comparable OER performance to FNCO. Aasen *et al.* [95] studied tri-metallic Ni-Co-Fe oxides, anchored onto N-CNTs (FNCO/N-CNT), which were impregnated into a porous carbon substrate (gas diffusion layer or GDL) using vacuum infiltration. By combining FNCO with N-CNTs the OER potential decreased, improving the overall bifunctional efficiency of the catalyst compared with Lu *et al*. [97]. The resultant air electrode had a final discharge and charge potential of 1.14 V and 1.95 V, respectively (58.5% efficiency after 200 cycles at 10 mA/cm^2) [95]. Li *et al.* [57] created a $(FeCoNi)_3O_4/Mn_3O_4$

nanocomposite, which had a potential gap of 0.7 V and good electrode stability when cycled for 400 h at 2 mA/cm^2. Aasen *et al.* [98] also investigated the effects of adding Zn to TMO catalysts on air electrode and battery performance. Zinc is incorporated into the TMOs during battery cycling, so including Zn in the TMOs during their fabrication was considered as a means of improving stability. Zn incorporation into TMOs induced the transition metals to move to higher oxidation states. Zn-Mn, Zn-Co, and Zn-Mn-Co oxide catalysts compared favourably with the benchmark Pt-Ru/C (55.3%) catalyst during battery cycling tests (100 h at 10 mA/cm^2) with final efficiencies of 56.6%, 55.8%, and 54.2%, respectively [98]. Although Zn-Mn-Co oxide had the lowest final efficiency, it was the most stable catalyst under the cycling conditions. Additionally, Xu *et al.* [33] formulated a $ZnCo_2O_4$ spinel on CNTs that outperformed a Pt/C catalyst. The Zn-Co spinel oxide had a power density of about 249 mW/cm^2 and a potential gap of 1.43 V at 65 mA/cm^2, while the Pt/C catalyst had a power density of 221 mW/cm^2 and a potential gap of 1.52 V at 35 mA/cm^2 before failing [33].

This chapter investigates Ni-Mn-Co tri-metallic oxides and Ni-Mn-Co-Zn tetra-metallic oxides anchored onto N-CNTs impregnated into a GDL made from porous carbon paper. This synthesis method has been demonstrated to deposit the catalyst throughout the microporous layer of the GDL, thereby improving battery performance [46], [95]. The combinations of the tri- and tetra-metallic oxides were chosen based on previous studies and statistical design, with the goal of optimizing catalyst composition and battery performance. Based on analysis of the previously mentioned studies, it was thought that anchoring various Ni-Mn-Co oxides onto N-CNTs would improve the electrochemical results. Zinc was selected as one of the components with the Ni-Mn-Co oxide to improve cyclability. Anchoring Ni-Mn-Co and Zn-Ni-Mn-Co oxides onto N-CNTs coupled with impregnation into GDL has not been studied previously.

3.2. Experimental

3.2.1. Synthesis of Electrocatalysts and Electrode Preparation

The method for generating electrocatalysts is based on the procedure developed previously in our group [46]. A catalyst precursor was prepared by mixing 50 mg of N-CNTs and 210 mg of a metal salt mixture, consisting of $NiO_4S\bullet7(H_2O)$, $Mn(CH_3COO)_2\bullet4(H_2O)$, $Co(CH_3COO)_2\bullet4(H_2O)$, and/or $Zn(CH_3COO)_2\bullet4(H_2O)$, with ~80 mg of NaOH and 10 mL of ethanol in a glass vial. The catalyst mixture was then mechanically stirred at about 800 rpm for

10 min before undergoing sonication (bath sonicator) for 5 h. The porous carbon paper substrate (GDL) was sectioned into circles with a diameter of 4.5 cm. The GDL circles were placed into beakers with the catalyst mixture, 1 mL of Nafion 5%, and 15 mL of ethanol. The total mixture was sonicated for 20 min and then air dried for 5 min. The catalyst soaked GDL was essentially used as a filter paper; ~5 mL of the catalyst suspension was vacuum filtered through the GDL. Selected samples were annealed at 300°C for 30 min. Previous studies showed that annealing improved electrochemical performance [46], [95]. For simplicity, each sample was labeled based on the elements included and the metal salt mass ratio in the suspension. For example, Ni-Mn-Co oxide with a metal salt mass ratio of [1:1:1] anchored onto nitrogen doped carbon nanotubes is denoted as NMCO/N-CNT-[1:1:1]. It should be noted that the metal salt ratios represent the amount of metal salt added into the catalyst suspension and not actual metal ratios in the synthesized catalyst. Annealed samples include the suffix 'An'. The ratio of metals added during synthesis is very close to the ratio of metal salts added. The difference in mass for the GDL samples (mass after synthesis – mass before synthesis) was divided by the area of the GDL disc (15.9 cm^2) to obtain the catalyst mass loading for each sample.

Pt-RuO_2/C catalysts were also prepared for a baseline comparison. A spray coating method was used to prepare the electrode. The catalyst solution consisted of 50 mg of Pt-RuO_2/C (30% Pt and 15% RuO_2 on carbon black; from Alfa Aesar), 2 mL of deionized water, 1 mL of ethanol, and 0.1 mL of Nafion (5 wt%). A 3 cm x 7 cm piece of GDL was sprayed with an air brush. In order to activate the Nafion and improve the adhesion of the Pt-RuO_2/C to the GDL, the spray coated GDL was placed in a vacuum oven heated to 60°C for 0.5 h. The Pt-RuO_2/C on GDL is denoted as Pt-Ru/C and the mass loading is 0.5 mg/cm^2.

3.2.2. Design of Experiments

A design of experiments (DOE) approach, using Design-Expert (StatEase), was utilized as a guide towards determining metal salt ratios for both the tri- and tetra-metallic oxides. There are different designs that can be used to analyze experiments. Since the goal of this work was to optimize the catalyst composition, a mixture design was chosen. The mixture design included up to four components (Zn, Ni, Mn, Co) with a total mass of 210 mg. One factor (annealed or unannealed) was included, as well as two responses (potential gap and efficiency at 20 mA/cm^2). The aim was to predict compositions that would minimize the potential gap and maximize the

efficiency. Previous electrochemical performance information gleaned from the literature for monometallic (Mn, Co, Ni), bimetallic (Mn-Co, Ni-Co, Mn-Co, etc.), and tri-metallic (Zn-Mn-Co) oxides was included in the analysis (Table S3-5) [46], [95], [98], as well as several tri-metallic (Ni-Mn-Co) and tetra-metallic (Zn-Ni-Mn-Co) oxide compositions that were tested in our laboratory (Table S3-6). The additional metallic oxide compositions tested (Table S3-6) were chosen based on previous studies that used similar metal salt ratios (e.g., Assen *et al.* [46], [95], [98] used a [1:1] Mn-Co ratio and a [5:1] Co-Fe ratio). These compositions (e.g., Zn-Ni-Mn-Co ratio [1:1:1:1]) were tested to provide additional information to improve the DOE results for the specific metal oxide compositions. Anderson *et al.* [99] provide further detail explaining the analysis and optimization process for the DOE. Optimization allowed for importance and constraints to be controlled for each component, response, and factor; e.g., the minimum/maximum amount of each metal salt, maximum efficiency, and minimum potential gap. For the tri-metallic oxide study, Zn was excluded from the DOE. The best compositions based on DOE predictions are shown in Table 3-1 and Table 3-2 and are ranked according to predicted potential gap and efficiency, with a ranking of 1 representing the best value. The NMCO/N-CNT-[1:1:12] electrode was not predicted by the DOE; however, to maintain consistency it was tested and classified as a DOE predicted electrode. Note that all the tri-metallic oxide compositions contained only a small amount of Ni, with Mn being the main metallic constituent. The main metallic elements for the tetra-metallic oxides were Mn and Zn, with only small amounts of Ni and Co.

Table 3-1 DOE Predictions for Ni-Mn-Co oxides

Predicted Metal Salt Ratios	Relative Predicted Efficiency*	Relative Predicted Potential Gap*
NMCO/N-CNT [1:9:4]	4	4
NMCO/N-CNT [1:24:17]	1	2
NMCO/N-CNT [1:23:18]	1	1
NMCO/N-CNT [1:29:12]	2	3
NMCO/N-CNT [12:1:1]	5	6
NMCO/N-CNT [1:12:1]	6	7
NMCO/N-CNT [1:1:12]	N/A	N/A
NMCO/N-CNT [1:40:1]	3	5

* A value of 1 represents the best predicted value for the category

Table 3-2 DOE Predictions for Zn-Ni-Mn-Co oxides

Predicted Salt Composition	Relative Predicted Efficiency*	Relative Predicted Potential Gap*
ZNMCO/N-CNT [16:1:24:1]	1	1
ZNMCO/N-CNT [19:1:20:1]	2	2

* A value of 1 represents the best predicted value for the category.

3.2.3. Microstructural Characterization

Scanning electron microscopy (Tescan VEGA3 SEM and Zeiss Sigma Field Emission SEM), including energy dispersive X-ray (EDX) spectroscopy, was done at accelerating voltages

of 5 kV and 20 kV (EDX analysis), while transmission/scanning transmission electron microscopy (JEOL JEM-ARM200CF TEM/STEM), coupled with EDX analysis, was done at 200 kV. For SEM sample preparation, a 1 cm x 1 cm section of the prepared electrode was placed onto double-sided carbon tape mounted on an aluminum stub. TEM samples were prepared by scraping the catalyst material from the GDL and combining with 2 mL of ethanol. The catalyst suspension was then sonicated for ~20 min, dropped onto a carbon-coated, Cu grid, and air dried. X-ray photoelectron spectroscopy (Versa Probe III (PHI 500) XPS) was done using a monochromatic Al-K_α x-ray source and a pass energy of 20 eV. The XPS samples were prepared by cutting the catalyst impregnated GDL into small pieces. Spectra were calibrated using the C 1s peak at a binding energy of 284.8 eV.

3.2.4. Electrochemical Testing

Linear sweep voltammetry (LSV) was done, using a BioLogic SP300 potentiostat, at a scan rate of 5 mV/s in oxygen saturated 1 M KOH with the catalyst impregnated electrode as the working electrode, Pt as the counter electrode, and Hg/HgO as the reference electrode. Battery testing was performed using homemade cells. The electrolyte was 6 M KOH + 0.25 M ZnO. Zinc sheet metal (2 cm x 6 cm x 0.1 cm) was used as one electrode and the catalyst impregnated GDL (1 cm x 1 cm exposed to electrolyte) was used as the air electrode, with a Ni current collector. Rate testing was done using various potentiostats (BioLogic VSP-100 and SP300) with a homemade vertical cell at current densities of ± 2 mA/cm^2, ± 5 mA/cm^2, ± 10 mA/cm^2, and ± 20 mA/cm^2 for 10 min each. The samples that performed the best at 20 mA/cm^2 during rate testing were then cycled in a battery configuration. Cycling tests were carried out using an Arbin LBT20084 potentiostat, at 10 mA/cm^2 in ambient air, with a homemade horizontal cell. Each test consisted of 200 cycles, where an individual cycle was a total of 30 min (a rest period of 5 min, a discharge period of 10 min, another 5 min rest period, and a charge period of 10 min). Different cell configurations were used for cycling and rate tests because of the nature of each test. The vertical cell design was easier to setup and dismantle. All full cell electrochemical tests used Zn/Zn^{2+} as the reference electrode. The potential difference was determined by subtracting the ORR potential from the OER potential, while the efficiency was obtained by dividing the OER potential by the ORR potential.

3.3. Results and Discussion

3.3.1. Ni-Mn-Co Tri-Metallic Oxides

Several combinations of Ni-Mn-Co oxides anchored onto N-CNTs were tested. Table S3-6 shows the base compositions tested to provide additional information for the DOE, while Table S3-7 provides the compositions tested based off the DOE results, as explained in Section 3.2.2.

3.3.1.1. Electrochemical Results

Half-cell and full-cell configurations were tested (Figure 3-1) for several NMCO/N-CNT samples with different metal salt ratios. The samples shown in Figure 3-1 were chosen to show how the results vary based on metal salt composition, as well as the effect of annealing. The full list of samples tested, and their corresponding compositions, is shown in Table S3-6 and Table S3-7. Table S3-7 includes catalyst mass loading, ORR and OER potentials, the potential gap, and battery efficiency for the DOE predicted compositions. It has been previously shown that there are discrepancies between the half-cell performance and the full-cell performance due to the electrode preparation technique [98]. Since the preparation technique has a more significant influence on the full-cell performance than the half-cell performance, comparing the different electrodes based off of the full-cell performance will provide both catalytic and electrode performance information [46], [95], [98]. The onset potentials for ORR and OER LSV testing were determined from the potentials corresponding to a current density of ±10 mA/cm^2. The NMCO/N-CNT-[1:29:12]-An sample has the best ORR activity (Figure 3-1a) with an onset potential of -0.071 V, which is comparable to Pt-Ru/C (-0.064 V). The addition of Ni to Mn-Co significantly improves the ORR activity from -0.160 V (Mn-Co oxide) to a range of values from -0.130 to -0.071 V (Ni-Mn-Co oxides) [95]. It has been previously found that ORR performance improves when adding a third metal into the metal-nitrogen-carbon mix as it creates more active sites [95]. The good ORR activity of NMCO/N-CNT-[1:29:12]-An is due to the high amount of Mn. NMCO/N-CNT-[1:5:1] and NMCO/N-CNT-[1:9:4]-An have the best OER activity with onset potentials of 0.65 V and 0.67 V, respectively (Figure 3-1b). These values are comparable to Pt-Ru/C which has an OER onset potential of 0.62 V. When comparing the OER activity of bi-metallic oxides with Ni-Mn-Co tri-metallic oxides, there is little to no improvement in behavior. This is likely due to the high amount of Mn, which is ORR active but not particularly OER active.

Figure 3-1c shows the difference in ORR potential for the samples. Annealing samples with higher Mn to Ni ratios tends to improve the ORR performance, while the OER performance is unaffected. At low current densities, such as 2 mA/cm^2 and 5 mA/cm^2, the samples have similar electrochemical performance, with the exception of the NMCO/N-CNT-[1:29:12] unannealed electrode which deviates at 5 mA/cm^2. The NMCO/N-CNT-[1:9:4]-An sample was one of the best materials in terms of electrochemical performance. Multiple electrodes (four) of this material were fabricated and tested to ensure reproducibility. At 20 mA/cm^2, NMCO/N-CNT-[1:9:4]-An has an average efficiency and a potential gap of 58.4% and 0.85 V (Figure 3-1c), respectively, which are comparable to the values for Pt-Ru/C (60% and 0.82 V). When compared with $MnCoO_x$/N-CNT, $NiCoO_x$/N-CNT, and $NiMnO_x$/N-CNT from Assen *et al.*, with efficiencies of 52.1%, 57.1% and 57.8% at 20 mA/cm^2, respectively, the combination of the three elements has a synergistic effect, resulting in better electrochemical performance [95]. The Mn to Co metal salt ratio in $MnCoO_x$/N-CNT was [1:1], while the Ni to Co and Ni to Mn metal salt ratios in $NiCoO_x$/N-CNT and $NiMnO_x$/N-CNT samples were [5:1] and [1:7], respectively [95]. Additionally, a $MnCoO_x$/N-CNT sample with a Mn:Co ratio of 5:1 was fabricated to provide further evidence of the beneficial effect of Ni (Fig. S1). The $MnCoO_x$/N-CNT-[5:1]-An sample had an efficiency of 53.7% at 20 mA/cm^2, which compares poorly to the NMCO/N-CNT-[1:5:1] electrode (57.8% at 20 mA/cm^2). Further comparison of the NMCO/N-CNT-[1:1:1] and NMCO/N-CNT-[1:9:4]-An samples (efficiencies of 57.1%, and 58.4% at 20 mA/cm^2, respectively) with the bimetallic $MnCoO_x$/N-CNT shows an improvement of almost 5% in the electrochemical performance with the addition of various amounts of Ni. Similarly, the NMCO/N-CNT-[1:29:12]-An sample (57.8% at 20 mA/cm^2) has the same electrochemical performance improvement, but with the smallest amount of Ni. This confirms that the addition of Ni to Mn-Co oxide improves the electrochemical performance, despite the amount of Mn in the tri-metallic oxide.

Power density curves were obtained for the best performing electrodes, NMCO/N-CNT-[1:9:4]-An, [1:29:12]-An, and [1:5:1] (Figure 3-1d). The maximum power densities of the catalysts decrease in the following order: NMCO/N-CNT-[1:5:1] > NMCO/N-CNT-[1:29:12]-An > NMCO/N-CNT-[1:9:4]-An. The best catalyst in terms of maximum power density, NMCO/N-CNT-[1:5:1] (116 mW/cm^2), is comparable to Pt-Ru/C (120 mW/cm^2). The amount of Mn correlates with power density; NMCO/N-CNT-[1:5:1] has the best power density and has the

highest amount of Mn, while NMCO/N-CNT-[1:9:4]-An has the lowest amount of Mn added. Although NMCO/N-CNT-[1:9:4]-An had the best ORR potential during rate testing, its power density performance was the poorest of the three tri-metallic oxides. From the LSV ORR results, the most positive onset potential was obtained with the NMCO/N-CNT-[1:29:12]-An electrode, despite containing slightly less Mn compared with NMCO/N-CNT-[1:5:1]. LSV and rate testing are affected by the synergism between the composition of the three metal salts.

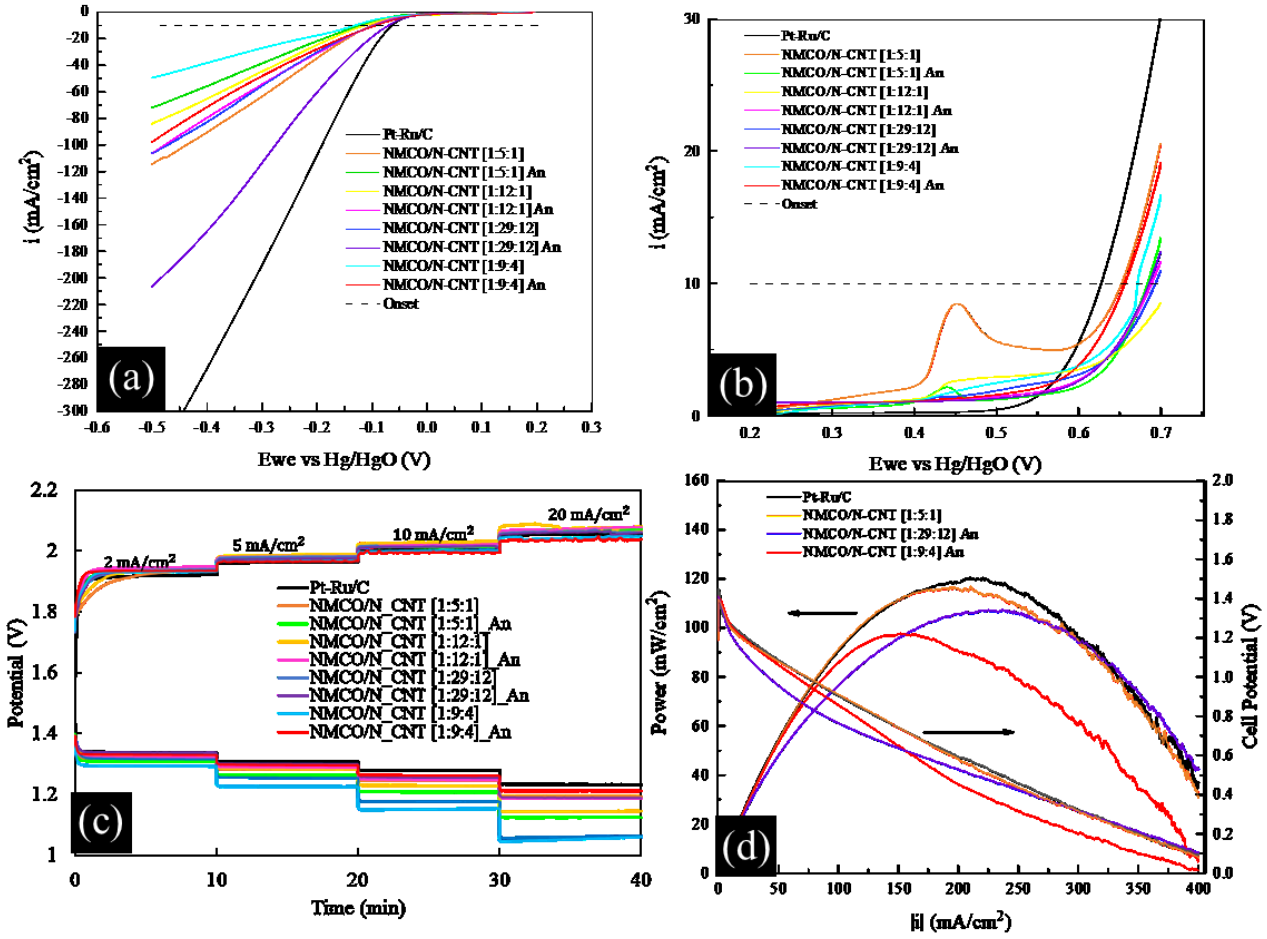

Figure 3-1 Electrochemical results for tri-metallic catalysts. (a) ORR LSV measurements, (b) OER LSV measurements, (c) battery rate tests, (d) power curves; some electrodes have been annealed while others are in the as fabricated condition.

The electrochemical results for all the electrodes tested are summarized in Figure 3-2; the various electrodes are compared at a relatively high current density of 20 mA/cm^2. In general, a higher Mn to Ni salt ratio coupled with annealing generally improves ORR performance.

Conversely, a higher Ni to Mn salt ratio and annealing negatively impacts ORR performance. Annealing tends to improve ORR performance for samples with large amounts of Mn. Since NaOH is added during synthesis, it is possible that a thin Na-rich layer forms over the surface of the GDL [46]. Annealing eliminates this layer leaving just the N-CNTs and catalyst material. Compositional changes and heat treatment did not have a significant effect on OER performance (Table S3-7).

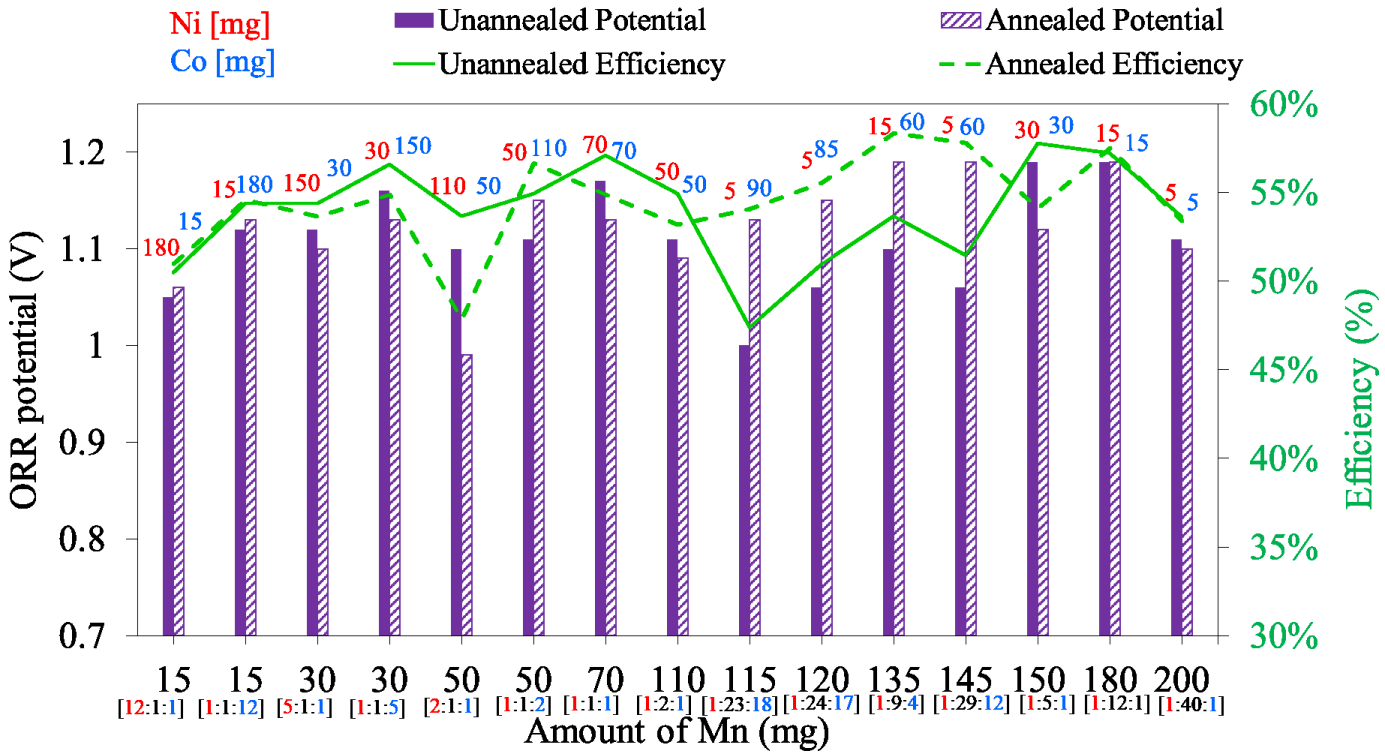

Figure 3-2 ORR potential and efficiency as a function of Mn salt composition in the catalyst suspension. Electrochemical results obtained from full cell battery rate tests at 20 mA/cm^2 for Ni-Mn-Co tri-metallic oxides. The amount of Ni salt used in the samples is shown above the bars in red and the amount of Co salt used is shown in blue. The corresponding metal salt ratio is shown below the Mn salt composition.

Since NMCO/N-CNT-[1:9:4]-An and NMCO/N-CNT-[1:5:1] were the best performing samples during rate testing, battery cycling tests were performed for 200 cycles (30 min per cycle) at a current density of 10 mA/cm^2 (Figure 3-3). The first ten cycles during bifunctional cycling are essentially conditioning cycles, and correspond with the amount of time needed to

completely wet the GDL. The effective initial (cycle 11) efficiency of NMCO/N-CNT-[1:9:4]-An is 52% and the final efficiency is 52.3%, which represents a slight gain (0.3%) in performance. The initial (cycle 11) efficiency of NMCO/N-CNT-[1:5:1] is 56% and the final efficiency is 53.3%; a 2.7% loss in performance.

During cycling the ORR potential remains constant for NMCO/N-CNT-[1:5:1] (1.16 V), while it slightly decreases at about the 125th cycle for NMCO/N-CNT-[1:9:4]-An (1.13 V). The initial drop in ORR potential during conditioning may be related to incomplete wetting of the catalyst infused GDL as mentioned above; wetting improves after several cycles. The slight decrease in ORR during the later cycles is likely due to the formation of K_2CO_3 blocking some of the catalyst sites. Evidence of K_2CO_3 forming during cycling was confirmed during microstructural characterization (3.3.1.2). The OER potential for NMCO/N-CNT-[1:9:4]-An stabilizes at 2.17 V after the conditioning cycles, whereas the OER potential for the NMCO/N-CNT-[1:5:1] electrode increases steadily until about the 80th cycle stabilizing at 2.16 V. The OER potential curve is not as smooth as the ORR potential, because oxygen bubbles form, coalesce, and are released from the GDL during charging. Oxygen bubbles forming on the electrode is a problem as they block active sites and increase the OER potential. Although the NMCO/N-CNT-[1:5:1] electrode had the better initial efficiency, the overall electrode stability is poorer compared with the NMCO/N-CNT-[1:9:4]-An electrode, which had 0.3% difference between initial and final efficiencies. However, both samples outperform Pt-Ru/C in terms of stability and electrochemical performance during long term cycling. Pt-Ru/C has an initial efficiency of 61% and a final efficiency of 38%.

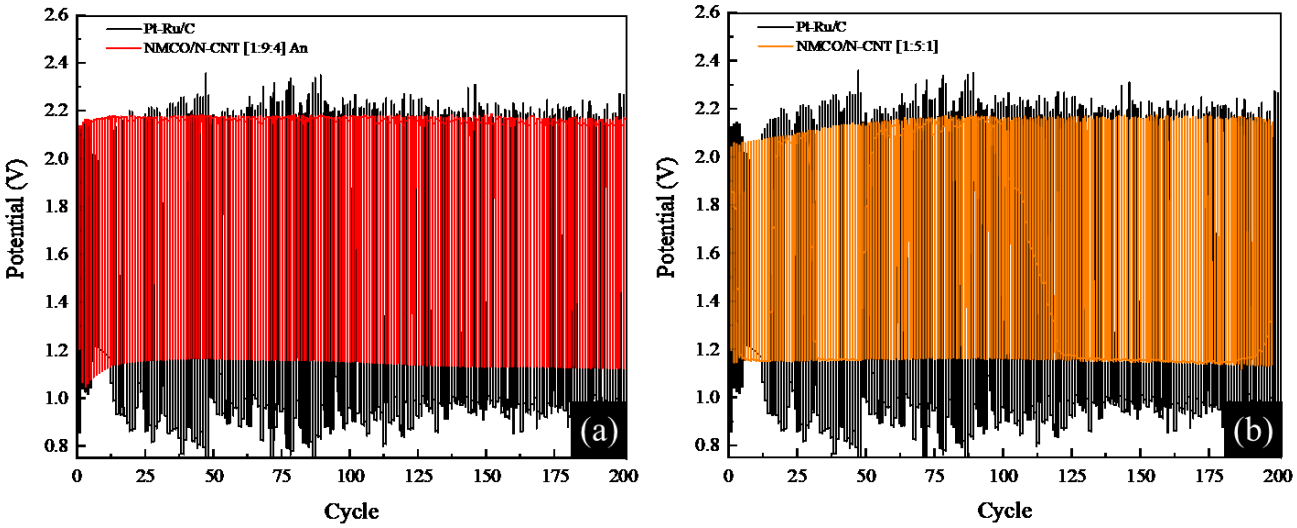

Figure 3-3 Bifunctional cycling of (a) NMCO/N-CNT-[1:9:4]-An, and Pt-Ru/C, and (b) NMCO/N-CNT-[1:5:1], and Pt-Ru/C. Bifunctional cycling was done using a homemade Zn-air battery at a current density of 10 mA/cm^2 for 200 cycles (30 min per cycle) in 6 M KOH + 0.25 M ZnO.

3.3.1.2. Microstructural Characterization

Several samples, before testing, were examined using SEM; an example is shown in Figure 3-4 for the NMCO/N-CNT-[1:9:4]-An sample. The images (Figure 3-4a-c) show nanoparticles, which appear as bright spots, anchored onto N-CNTs (yellow arrows), as well as clusters of oxide particles on the GDL surface (green arrows). The N-CNTs (blue arrows) have a bamboo like structure created by nitrogen doping (red square) [100]. The EDX spectrum in Figure 3-4d, from the overall area, shows strong peaks from the three metallic species, Mn, Co, and Ni. The carbon peak is attributed to the GDL and the N-CNTs, while the strong oxygen peak is from the metal oxide nanoparticles. The F peak is due to the PTFE used in the GDL to make it somewhat hydrophobic, while the small Na and S peaks are likely residual Na and S remaining from NaOH and $NiO_4S{\cdot}7(H_2O)$ used during synthesis. Figure 3-5 compares the Mn:Co metal ratios (in the metal salts) added during synthesis with the actual metal ratios in the electrodes determined through SEM EDX analysis. Nickel is not included in the comparison, since there is Ni present in the CNTs, so the Ni composition would be misleading. The Mn:Co ratios in the salts are very similar to the metal salt ratios.

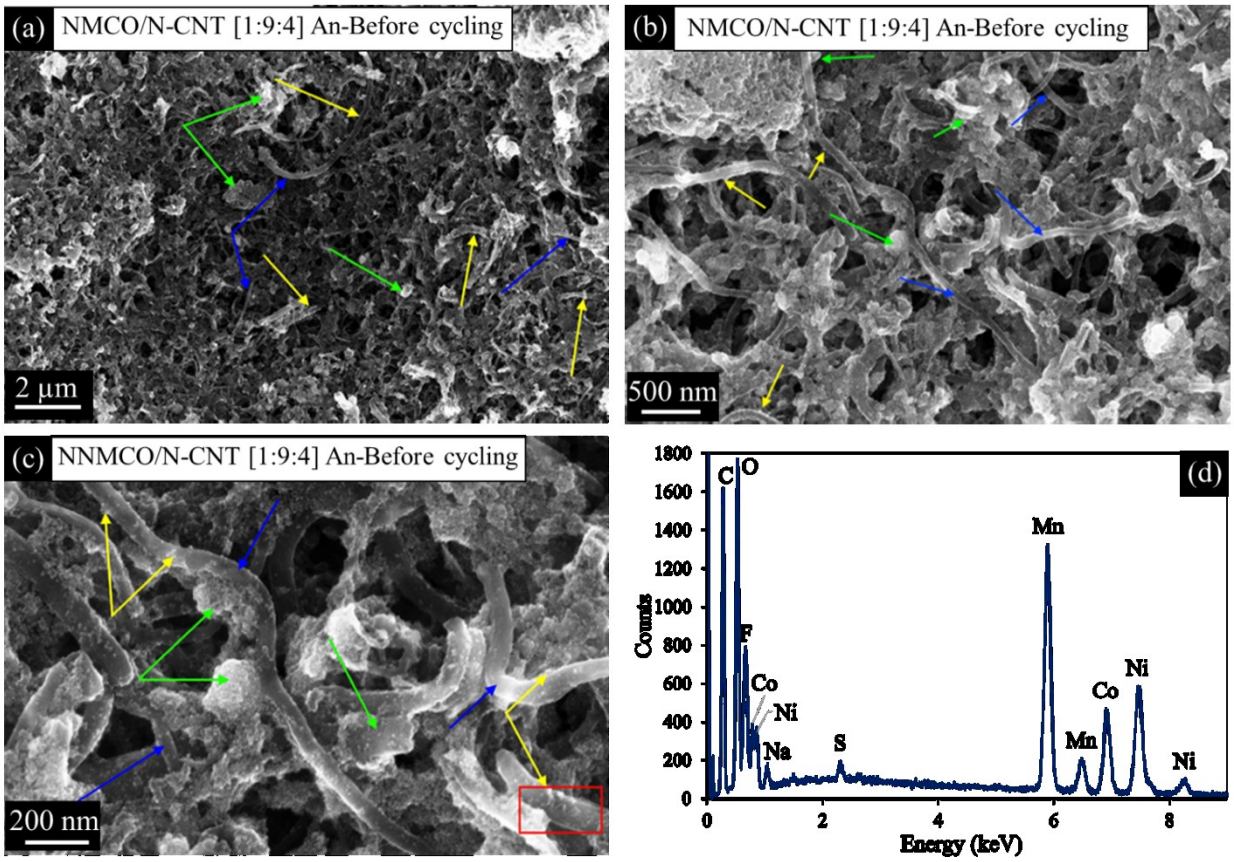

Figure 3-4 SEM and EDX analysis of NMCO/N-CNT-[1:9:4]-An after fabrication and before cycling. (a)-(c) Secondary electron (SE) images. Blue arrows indicate N-CNTs, green arrows indicate clusters of precipitates on the GDL surface, and yellow arrows indicate nanoparticles decorated on the N-CNTs. The red box in (c) shows flaws created by N doping of CNTs. (d) EDX spectrum from red box region in (c).

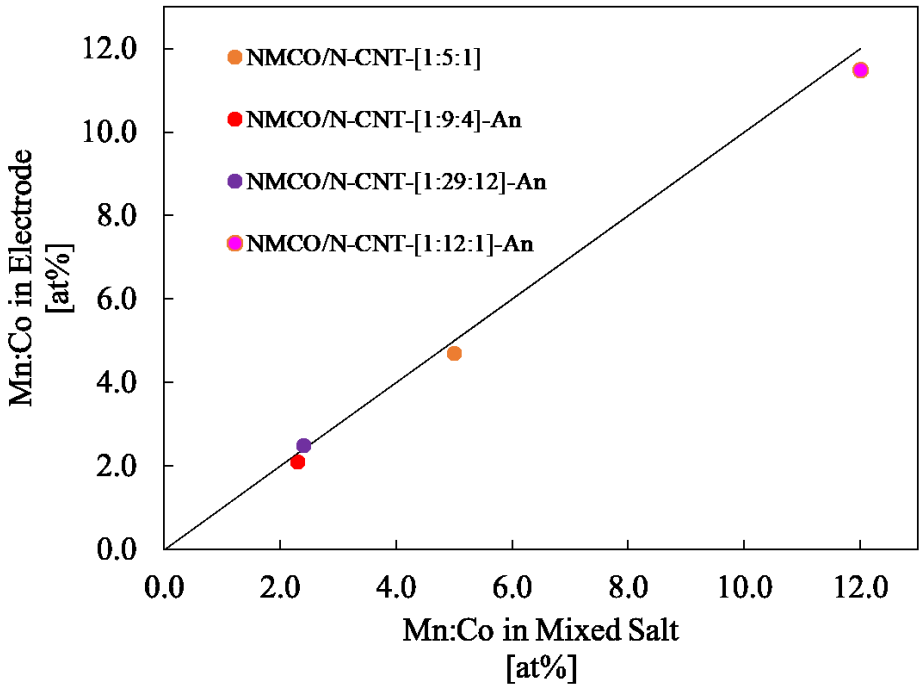

Figure 3-5 Mn:Co atomic ratio comparison between the mixed salts and fabricated catalysts within the electrode. The mixed salt ratio is prior to synthesis, while the electrode metal ratio is after synthesis as determined by EDX analysis. The black line represents a one-to-one correspondence between the electrode composition and the mixed salt composition.

Further microstructural characterization was done using TEM/STEM analysis. The NMCO/N-CNT-[1:9:4]-An sample, which is one of the better performing electrodes, is shown in Figure 3-6; other samples are similar. The high resolution TEM (HRTEM) image (Figure 3-6b) illustrates through the lattice fringes present that the metal oxides on the nanotubes are crystalline. The STEM high angle annular dark field (HAADF) image of the NMCO/N-CNT-[1:9:4]-An sample shows oxide nanoparticles anchored onto the N-CNTs as well as clusters of nanoparticles (Figure 3-6c). This confirms the SEM observations. EDX maps for Ni, Mn and Co are also provided (Figure 3-6e-g). The nanoparticle clusters contain all three metals, while the composition of the anchored nanoparticles is less clear. The anchored nanoparticles definitely contain Mn and Co; however, they do not appear to contain Ni. Nickel is present over the entire nanotube, which is a consequence of Ni being used as a catalyst during CNT synthesis (Figure 3-6e). The anchored nanoparticles do not show higher Ni levels relative to the CNTs, which indicates that Ni is either not present in the nanoparticles or is present in low concentrations, less

than the Ni concentration in the nanoparticle clusters. The relative amounts of each metal deposited in the GDL for NMCO/N-CNT-[1:9:4] are 7 at%, 62 at%, and 31 at%, for Ni, Mn, and Co, respectively. The TEM EDX results confirm the SEM EDX composition analysis.

A selected area diffraction (SAD) pattern (Figure 3-6h) was obtained from the TEM bright field (BF) image shown in Figure 3-6a. There are two sets of rings in the SAD pattern; one set from carbon and the other set from the metal oxide. The carbon rings, faint and continuous, are from the CNT, while the metal oxide rings are spotty and discontinuous. The metal oxide pattern was indexed to a cubic Mn-Co oxide spinel phase (PDF #23-1237 and a = 8.269 nm). The spinel phase in this sample has an overall Mn to (Co+Ni) ratio of about 2:1, which correlates to a composition of $(Ni,Co)Mn_2O_4$. To balance the O^{2-} ions, 2 of the 3 metals must have a valence of 3+ while the other metal has a valence of 2+. This will be addressed further during the XPS analysis.

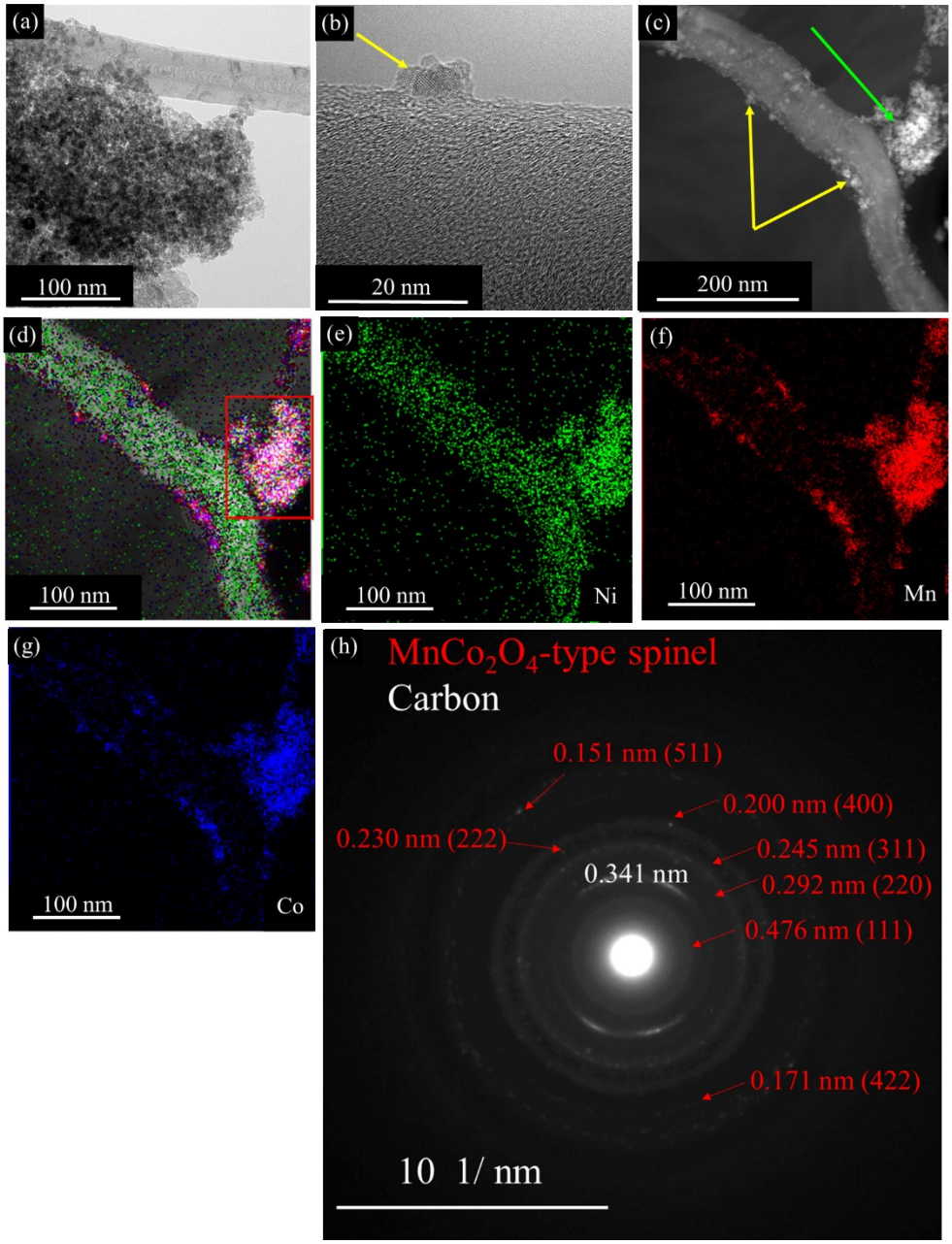

Figure 3-6 TEM/STEM analysis of NMCO/N-CNT-[1:9:4]-An before cycling. (a) TEM BF image of a cluster of nanoparticles, (b) HRTEM image, (c) STEM HAADF image, (e)-(g) EDX elemental maps for Ni, Mn, and Co with the Ni, Mn, and Co signals superimposed on the HAADF image in (d), and (h) SAD pattern from entire region shown in (f). Yellow arrows indicate nanoparticles decorated on the N-CNTs and green arrows indicate precipitate clusters on the GDL surface.

Further analysis of NMCO/N-CNT-[1:9:4]-An was done through XPS (Figure 3-7). The survey spectrum shows peaks corresponding to C, O, F, Na, Ni, Mn, and Co (Figure 3-7a). As mentioned earlier, F is from the PTFE in the GDL and the Na peak is likely from the NaOH used during synthesis of the electrode. O is present due to the metal oxide particles, while the C peak comes from the GDL and the N-CNTs. High resolution spectra for Ni 2p, Co 2p, and Mn 2p peaks are shown in Figure 3-7b –d. Deconvolution of the Ni $2p_{3/2}$, Co $2p_{3/2}$, Mn $2p_{3/2}$, Mn 3s, and O 1s spectra is shown in Figure S3-18. The O 1s spectrum (Figure S3-18) can be fit to 4 peaks, lattice oxygen (~529-530 eV), hydroxide bonds (~531 eV), carbon-oxygen bonds (~533 eV), and Na KLL Auger peak (~335 eV). Lattice oxygen (M-O-M bonds) and hydroxide bonds (M-O-H and H-O-H bonds) are the main contributions to the O 1s spectrum. It should be noted that the Ni $2p_{3/2}$ peak is quite weak, which is expected given the small amount of Ni in the sample, and there is interference with the F Auger peak at a binding energy of 861 eV. The F Auger peak makes up about 95 at% of the high-resolution Ni $2p_{3/2}$ spectrum. As such, the Ni analysis has a high degree of uncertainty. The Ni peaks at around 854 eV and 865 eV are due to Ni 2+, while the peaks at around 856 and 860 eV are from Ni 3+ (Figure S3-18) [97]. Ni $2p_{3/2}$ has an estimated valence of about 2.1 (Table 3-3). Deconvolution of Co $2p_{/32}$ high resolution spectrum (Figure S3-18, Table 3-3) suggests that Co 2+ is primarily present [95], [97]. To determine the valence of Mn, both the Mn $2p_{3/2}$ and Mn 3s high resolution spectra were used. The Mn $2p_{3/2}$ peak can be fit to Mn 2+, Mn 3+ and Mn 4+ multiplet peaks; however, Mn is present mainly as the 3+ and 4+ valences (Figure S3-18) [97] with an average valence of 3.5. The peak splitting of the Mn 3s spectrum indicates a valence of 3.0, since the difference between the peaks is 5.3 eV (Table 3-3) [95], [97], [101], [102]. There is some discrepancy between the Mn 3s and the Mn $2p_{3/2}$ peak analyses, but the valence is likely close to 3.0.

Based on the XPS and TEM/STEM analysis the tri-metallic oxide is a spinel phase. Spinel oxides have the structure of AB_2O_4, where A and B are divalent and trivalent cations, respectively. Typically, the divalent cations occupy the tetrahedral lattice sites, while the trivalent cations occupy the octahedral lattice sites [103]. The STEM EDX results show a Mn:(Co+Ni) ratio of ~2:1 while the SEM results give a Mn:Co ratio of ~2.1:1. The differences between the STEM and SEM results are small and are likely from the sampling volume. SEM EDX analysis is done over a much larger area of the GDL surface than the STEM EDX analysis. In addition, the EDX results for both analyses are semi-quantitative. In any case, the

Mn:(Co+Ni) ratio is close to 2, and combined with the XPS results, the Mn valence is 3+ while the Ni and Co valences are 2+. As such, Ni 2+ and Co 2+ occupy the tetrahedral sites and Mn 3+ occupies the octahedral sites giving a spinel composition corresponding to $(Ni,Co)Mn_2O_4$.

Table 3-3 XPS analysis from high resolution spectra

	Ni 2p 3/2			**Co 2p 3/2**			**Mn 2p 3/2**				**Mn 3s**	
Sample	2+ (at%)	3+ (at%)	Average Valence	2+ (at%)	3+ (at%)	Average Valence	2+ (at%)	3+ (at%)	4+ (at%)	Average Valence	Peak Splitting (eV)	Average Valence
NMCO/N-CNT-[1:9:4]-An	91.6	8.4	**2.1**	97.3	2.8	**2.0**	11.8	29.5	58.9	**3.5**	5.3	**3.0**

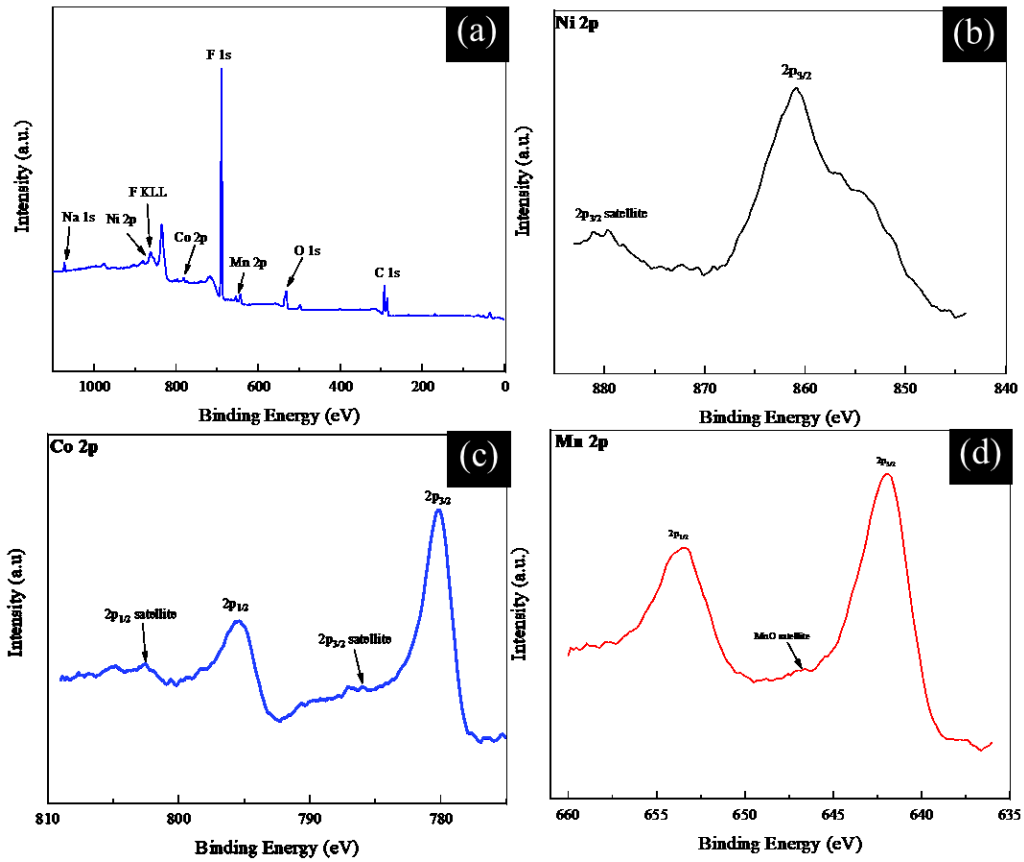

Figure 3-7 XPS spectra for NMCO/N-CNT-[1:9:4]-An. (a) Survey spectrum, (b) Ni 2p, (c) Co 2p, and (d) Mn 2p high resolution spectra.

SEM analysis was done after cycling of the NMCO/N-CNT-[1:9:4]-An sample (Figure 3-8). The electrode surface is partially covered by a fairly dense layer (Figure 3-8a-b – indicated by red arrows), which is K-, O- and C-rich (EDX spectrum in Figure 3-8c). The layer is likely K_2CO_3, with K coming from the electrolyte (6 M KOH + 0.25 M ZnO). The N-CNTs (blue arrows) and nanoparticle clusters (green arrows) are still visible, as are the anchored nanoparticles (yellow arrows - Figure 3-8b). The EDX spectrum (Figure 3-8c) shows the three metal peaks (Ni, Mn and Co). There is a small amount of Zn present as well, which may be incorporated into the metal oxide during testing. This will be addressed further in the next paragraph. The S peak is due to residual S remaining from the Ni salt ($NiO_4S{\cdot}7(H_2O)$) utilized during synthesis, while the F peak is from PTFE in the GDL.

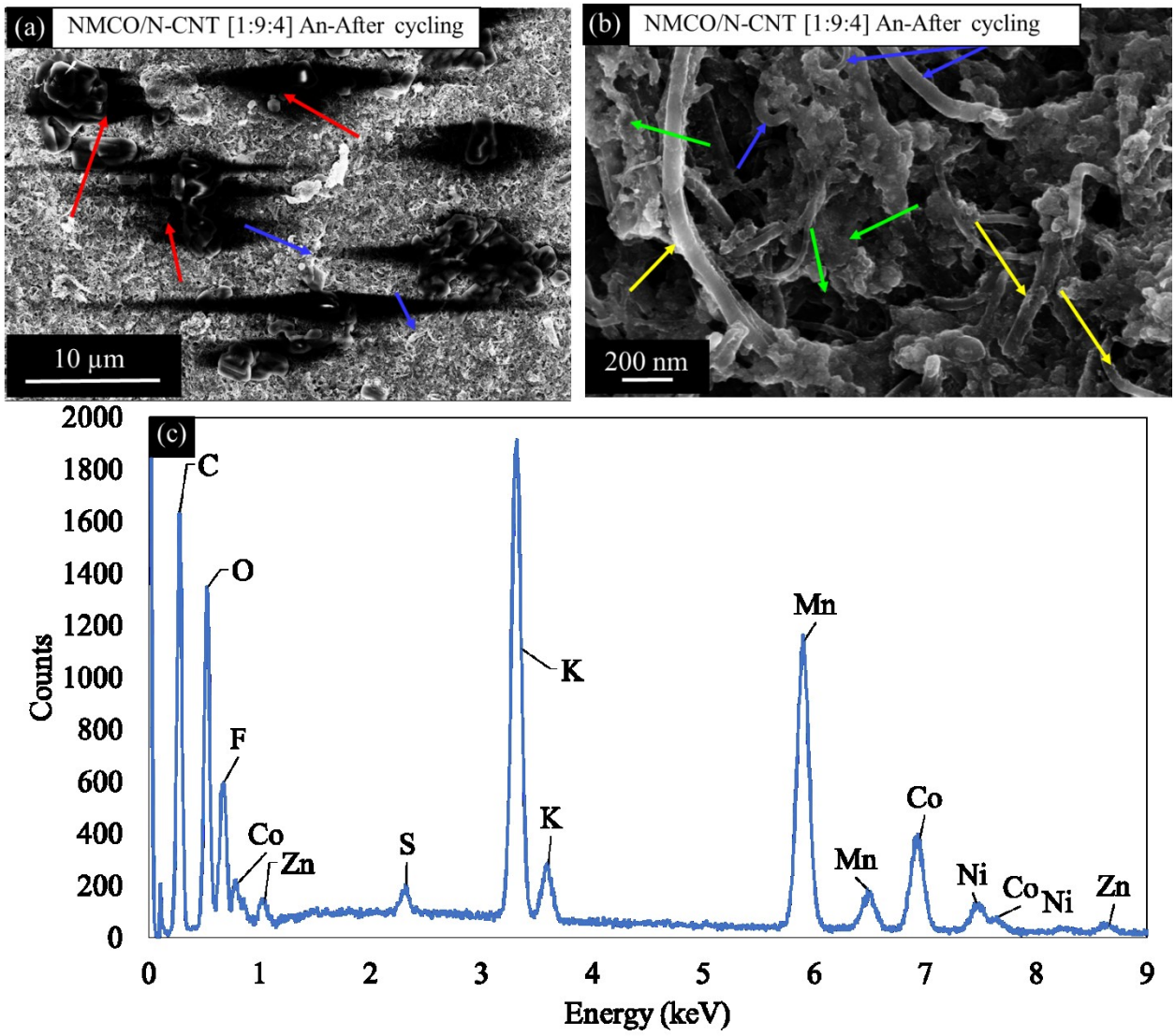

Figure 3-8 (a), (b) SEM SE images of NMCO/N-CNT-[1:9:4]-An after cycling, (c) EDX spectrum from entire GDL surface. Blue arrows indicate CNTs, green arrows indicate precipitate clusters on the GDL surface, yellow arrows indicate the nanoparticles decorating the N-CNTs, and red arrows indicate K-rich areas (likely K_2CO_3).

TEM/STEM analysis was done on the NMCO/N-CNT-[1:9:4]-An sample after cycling (Figure 3-9). A few N-CNTs are visible in the image, as well as nanoparticle clusters. EDX mapping shows that in addition to three metals (Ni, Mn and Co) and O, Zn and K are present. Potassium is essentially everywhere and is likely in the form of K_2CO_3, while Zn corresponds to the same positions as Mn and Co. Zinc appears to be incorporated into the metal oxide, which

has been previously reported in other studies [95], [98]. Nickel is present along the N-CNTs (as with the as fabricated samples) and in the metal oxide nanoparticles. In addition, a Ni particle is visible in Figure 3-9a-c; this is a catalyst particle from CNT synthesis. An SAD pattern (Figure 3-9j) was obtained from the metal oxide cluster shown in Figure 3-9i and was indexed to the same spinel phase as that in the as fabricated sample. This indicates that the particles do not undergo a phase change during cycling. However, as mentioned above, Zn is incorporated into the spinel structure. Since Zn has a valence of 2+, the likely spinel formula is $(Zn,Ni,Co)Mn_2O_4$.

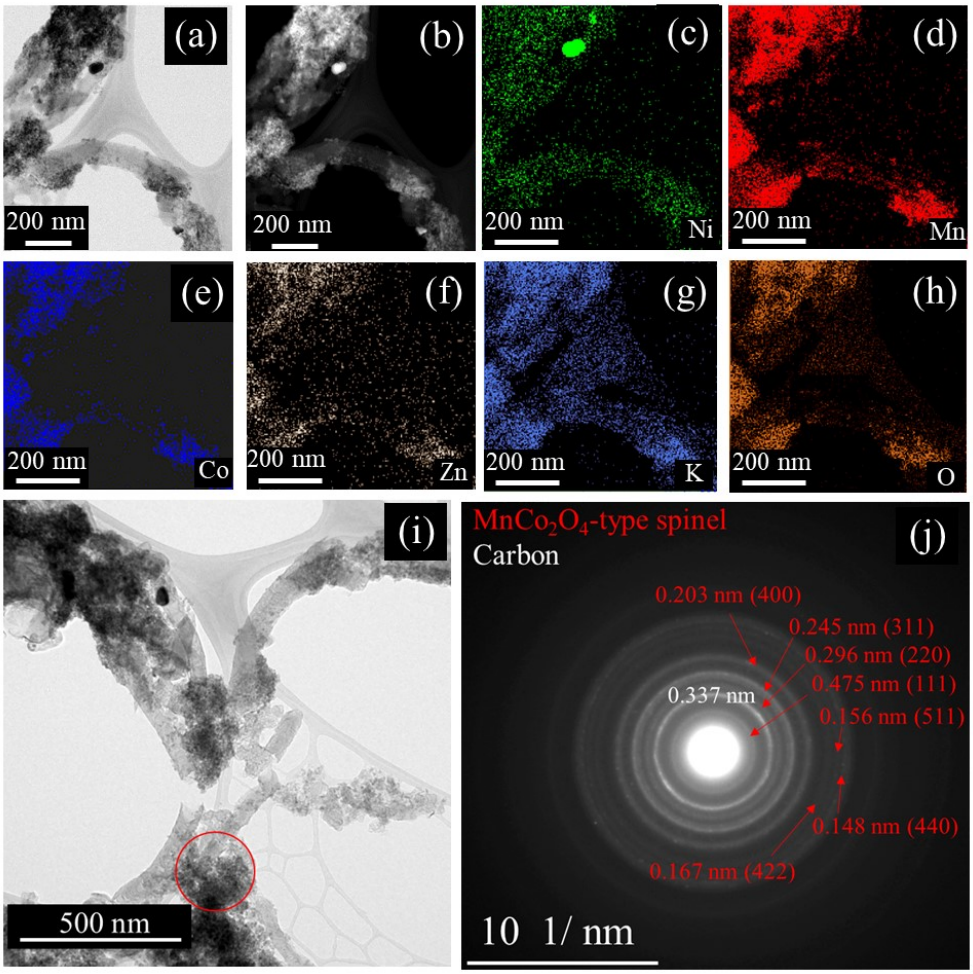

Figure 3-9 STEM analysis of NMCO/N-CNT [1:9:4] An after cycling. (a), (i) STEM BF images; (b) STEM HAADF image; (c)-(h) EDX maps for Ni, Mn, Co, Zn, K, and O, respectively; (j) indexed SAD pattern from the area outlined by the red circle in **i**. Bifunctional cycling was done using a homemade Zn-air battery at a current density of 10 mA/cm^2 for 200 cycles (30 min per cycle) in 6 M KOH + 0.25 M ZnO.

3.3.2. Zn-Based Tetra-Metallic Oxides

Zn was added to the Ni-Mn-Co oxides to form tetra-metallic ZNMCO/N-CNT with the aim of improving cycling performance.

3.3.2.1. Electrochemical Results

Compositions for ZNMCO/N-CNTs were chosen based on the DOE approach previously explained. Table S4 contains the full-cell test results for all the ZNMCO/N-CNT compositions tested, including the mass loading of each electrode. Half-cell and full-cell configurations were tested for three compositions (Figure 3-10). The compositions were somewhat arbitrarily chosen to show the DOE compositions and the effect of composition on the electrochemical results. ZNMCO/N-CNT-[1:1:5:1] sample was a baseline composition chosen to improve DOE accuracy, while the ZNMCO/N-CNT-[16:1:24:1] and –[19:1:20:1] samples were predicted from the DOE. Full-cell testing (Figure 3-10c) was used to compare the different electrodes as it provides both catalytic and electrode performance. The onset potential during LSV testing was taken at a current density of ±10 mA/cm^2. The ZNMCO/N-CNT-[16:1:24:1]-An sample has the best ORR activity with an onset potential of -0.107 V, while ZNMCO/N-CNT-[1:1:5:1] has an onset potential of -0.113 V (Figure 3-10a). These ORR activities are about 0.03 to 0.035 V lower than that of Pt-Ru/C, which has an ORR onset potential of -0.064 V. The best OER onset potential is 0.68 V for ZNMCO/N-CNT-[1:1:5:1], while the samples with higher amounts of Zn have OER onset potentials of ~0.80 V (Figure 3-10b). The OER activity of ZNMCO/N-CNT-[1:1:5:1] is comparable to that of Pt-Ru/C (0.623 V). The addition of Zn with Ni, Mn, and Co does not significantly change the OER LSV results; ZNMCO/N-CNT-[1:1:5:1] and NMCO/N-CNT-[1:5:1] have OER onset potentials of 0.68 V and 0.65 V, respectively. Comparing the Zn-Ni-Mn-Co oxides with previously studied Zn-Mn-Co oxides, the ORR activity is slightly improved (-0.107 V vs. -0.113 V) [98].

Figure 3-10c shows the effect of composition on rate testing. Annealing has a greater and positive influence on ORR potential compared with OER potential. Like the tri-metallic oxides, the ORR potential for the tetra-metallic oxides start to vary at 5 mA/cm^2. At 20 mA/cm^2, ZNMCO/N-CNT-[16:1:24:1] and ZNMCO/N-CNT-[19:1:20:1] have the lowest OER potential (~2.02 V) and are still able to maintain a reasonably high ORR potential, i.e., ~1.1 V to ~1.15 V, in the annealed condition. ZNMCO/N-CNT-[16:1:24:1]-An and ZNMCO/N-CNT-[1:1:5:1]-An

electrodes have efficiencies of 57.2% and 56.8%, and potential gaps of 0.88 V and 0.89 V, at 20 mA/cm^2, respectively. These two samples are comparable to Pt-Ru/C, which has an efficiency of 60% and a potential gap of 0.82 V at 20 mA/cm^2. The presence of Ni and lowering the Co amount improves the OER performance. This can be seen by comparing ZNMCO/N-CNT-[16:1:24:1]-An (2.01 V OER and 1.15 V ORR at 20 mA/cm^2) with tri-metallic Zn-Mn-Co oxide (2.07 V OER and 1.20 V ORR at 20 mA/cm^2) [98]. The Zn-Mn-Co oxide had a metal salt ratio of [1:1:1] [98].

Power density analysis of the best performing samples was done and compared with Pt-Ru/C (Figure 3-10d). The power densities of both ZNMCO/N-CNT-[16:1:24:1]-An (maximum value of 124 mW/cm^2) and ZNMCO/N-CNT-[1:1:5:1]-An (maximum value of 134 mW/cm^2) electrodes exceed that of Pt-Ru/C (maximum value of 120 mW/cm^2). ZNMCO/N-CNT-[19:1:20:1]-An has the lowest maximum power density of 110 mW/cm^2. Similar to the tri-metallic oxides, the power density appears to increase as the amount of Mn in the oxide increases. The ZNMCO/N-CNT-[1:1:5:1]-An electrode has the best ORR performance during rate testing and the highest maximum power density. Mn oxide is a well-known ORR catalyst and since the power density is determined during discharge, this could explain the increase in power density with increasing Mn content.

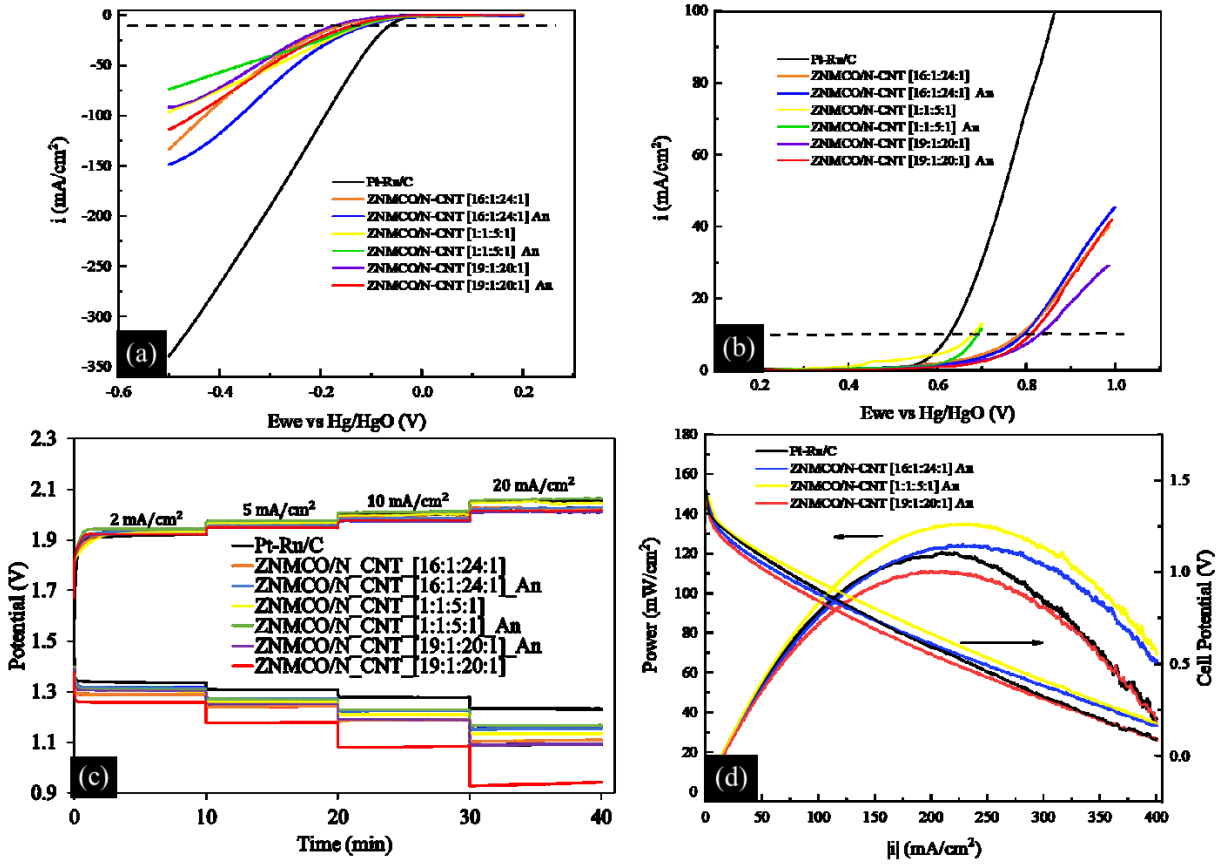

Figure 3-10 (a) ORR LSV curves, (b) OER LSV curves, (c) full cell battery rate testing for three tetra-metallic oxide compositions, and (d) power curves.

Figure 3-11 shows the effect of composition on the ORR potential and efficiency. The compositions shown are samples tested to increase the accuracy of the DOE (Table S3-6) and the best samples predicted by the DOE (Table S3-8). Most of the samples with a lower Ni salt content relative to the Mn salt amount, as well as being in the annealed condition, have higher ORR potentials and efficiencies. Larger Zn to Ni ratios also improve the electrochemical results.

Annealing tends to improve the ORR performance when both Zn and Mn salt amounts are higher than that of the Ni salt.

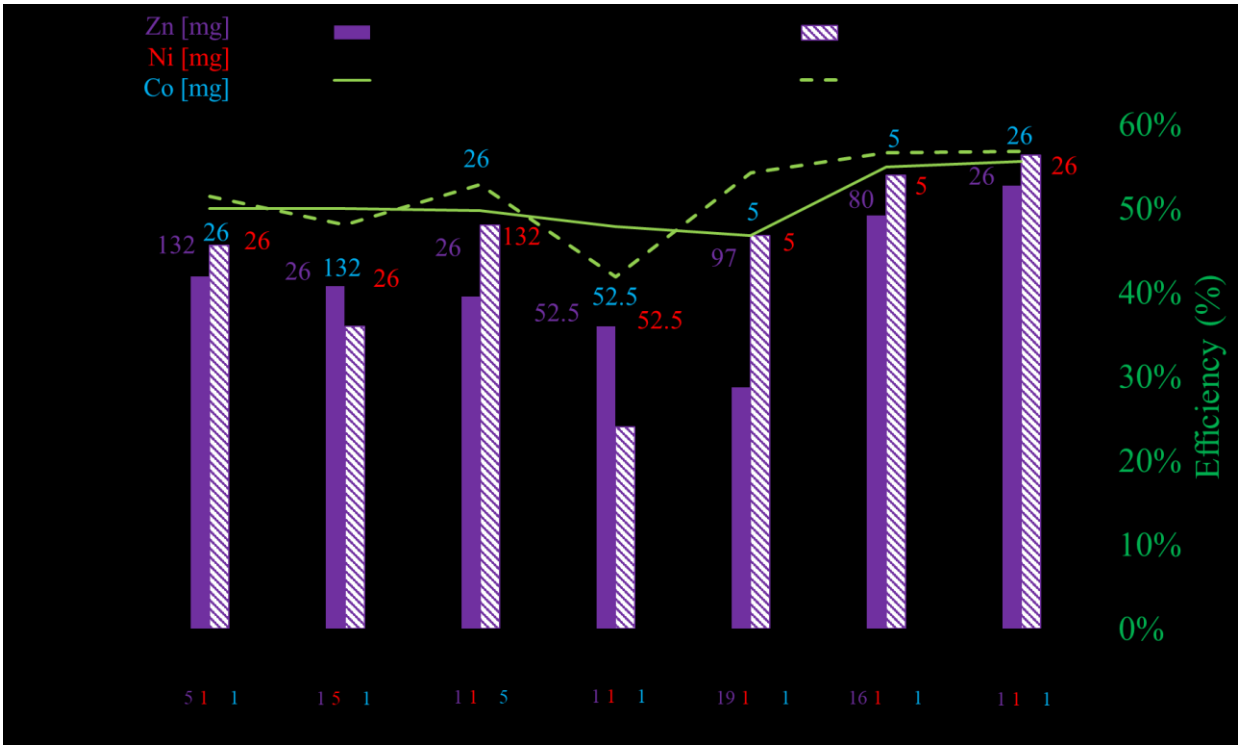

Figure 3-11 Mn amount vs. ORR potential and efficiency for full cell battery rate tests at 20 mA/cm^2 for Zn-Ni-based tetra-metallic oxides. The amount of Ni-salt, Zn-salt, and Co-salt used during synthesis is shown above the bars in red, purple, and black, respectively.

Since both ZNMCO/N-CNT-[1:1:5:1]-An and ZNMCO/N-CNT-[16:1:24:1]-An samples had the best efficiencies at 20 mA/cm^2, 56.8% and 56.9%, respectively, they were selected for cycle testing (Figure 3-12). The first approximately ten cycles during bifunctional cycling are essentially conditioning cycles, as discussed previously. The initial efficiencies (cycle 11) for ZNMCO/N-CNT-[1:1:5:1]-An and ZNMCO/N-CNT-[16:1:24:1]-An during cycling (200 cycles at 10 mA/cm^2) were 52.7% and 53.5%, respectively, while the final efficiencies were 55.8% and 56.4%, respectively. As previously discussed in Section 3.3.2.1, Pt-Ru/C is unstable and degrades quickly during bifunctional cycling. The initial efficiency (cycle 11) is 61%, while final efficiency is 38% at 10mA/cm^2 (200 cycles). The instability and poor overall performance of the Pt-Ru/C electrode can be partially attributed to bubble formation. However, after about the 50th

cycle no bubbles were detected on the surface of the GDL and the electrolyte did not leak, so that the unstable nature is due to degradation of the catalyst material.

The ZNMCO/N-CNT-[19:1:20:1]-An electrode had poor cycling stability and only has a 5.6% better overall efficiency compared with Pt-Ru/C (Figure S3-20). The ZNMCO/N-CNT-[1:1:5:1]-An and ZNMCO/N-CNT-[16:1:24:1]-An electrodes outperform the Pt-Ru/C electrode for overall efficiency as well as electrode stability. The final efficiencies for both samples are comparable to the tri-metallic samples (e.g., NMCO/N-CNT-[1:9:4]-An had a final efficiency of 52.3% - Figure 3-3), but the final OER potentials at 10 mA/cm^2 for the tetra-metallic oxide samples are in the 2.04 - 2.06 V range, which is better than the OER potentials the tri-metallic oxides (e.g., NMCO/N-CNT-[1:9:4]-An with an OER potential value of 2.12 V). In summary, the addition of Zn to Ni-Mn-Co improved the stability and OER potential of the electrode during bifunctional cycling.

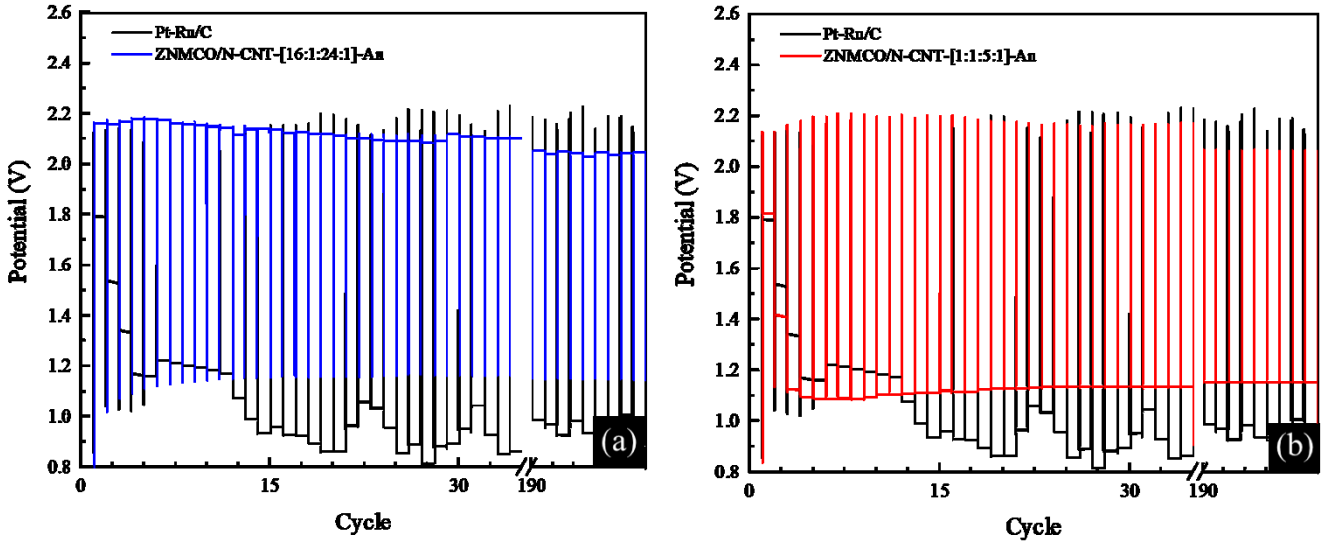

Figure 3-12 Bifunctional cycling data for (a) ZNMCO/N-CNT-[16:1:24:1]-An and Pt-Ru/C, and (b) ZNMCO/N-CNT-[1:1:5:1]-An and Pt-Ru/C. Bifunctional cycling was done using a homemade Zn-air battery at a current density of 10 mA/cm^2 with 200 cycles (30 min per cycle) in 6 M KOH + 0.25 M ZnO.

3.3.2.2. Microstructural Characterization

SEM analysis was done on ZNMCO/N-CNT-[16:1:24:1]-An before and after cycling (200 cycles at 10 mA/cm^2) (Figure 3-13). The SE image of the sample before cycling (Figure 3-13a) shows several N-CNTs (blue arrows) with nanoparticles anchored onto the N-CNTs (yellow arrows). There are also clusters of nanoparticles (green arrows) on the surface of the GDL. The N-CNTs are entangled with one another within the pores of the GDL. This observation has been reported previously in other studies that use the same impregnation technique to prepare samples [98]. The impregnation technique allows for the intertwined N-CNTs to be deposited in the pores of the GDL versus other techniques (e.g., spray coating) that deposit the catalyst on the surface of the GDL; thus samples prepared via impregnation have better performance [98]. The sample after cycling (Figure 3-13b) is covered with K_2CO_3 (red arrow) from the electrolyte, which obscures the underlying microstructure. EDX spectra for the samples before and after cycling are shown in Figure 3-13c and Figure 3-13d, respectively. After cycling, there is a significant K peak which is due to K_2CO_3 deposition on the surface of the GDL. The presence of F, Na, and S peaks in both spectra has already been discussed. There is a small Al peak for the cycled sample and this is from the stub used to support the sample in the SEM. The metal peaks in the cycled sample are suppressed because of the K_2CO_3 coating. There is no significant difference between the relative metal ratios before and after cycling. The relative amount of Mn detected after cycling decreases by ~5 at%, while the amount of Zn detected increases by about ~3 at%. The decrease in Mn is likely due to the K_2CO_3 covering the surface of the GDL and possibly from Mn dissolution during cycling. As previously discussed, the increase in the amount of Zn is likely from Zn from the electrolyte being incorporated during cycling.

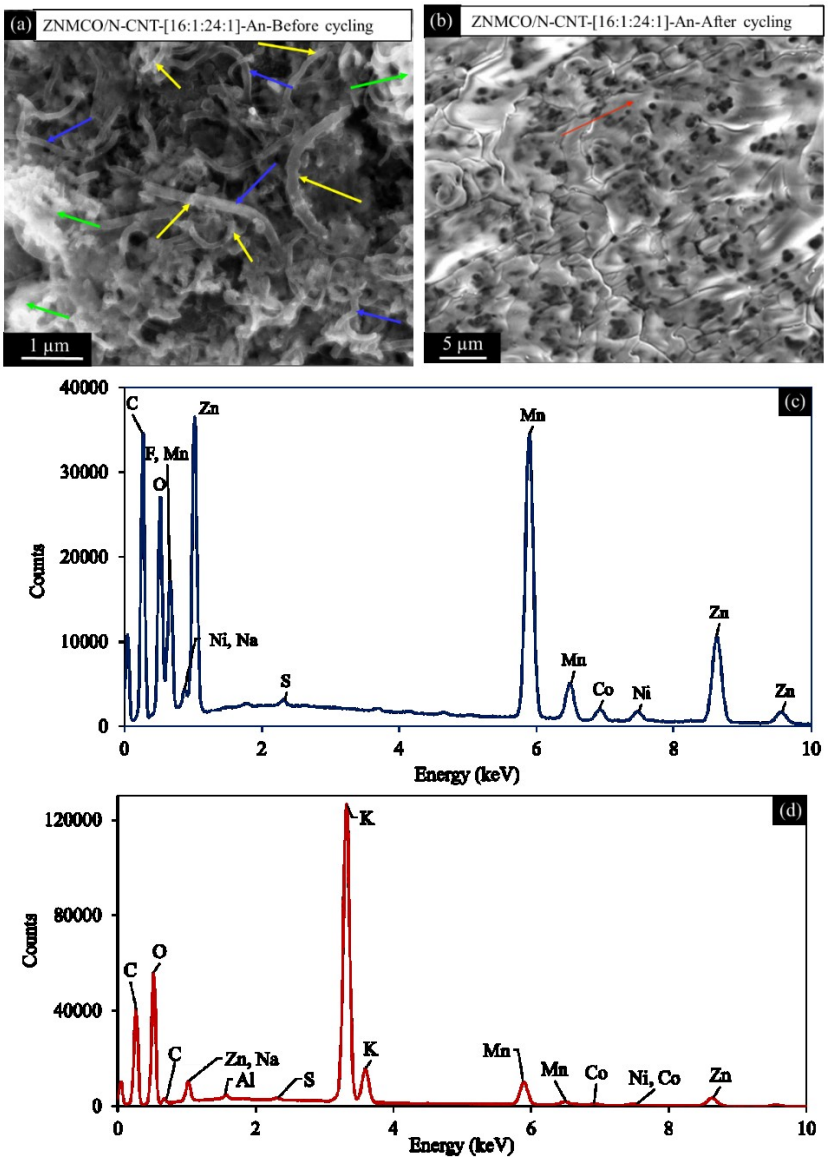

Figure 3-13 SEM and EDX analysis of ZNMCO/N-CNT-[16:1:24:1]-An. (a) SE image before cycling, (b) SE image after cycling, (c) EDX spectrum before cycling, and (d) EDX spectrum after cycling. Blue arrows indicate N-CNTs, green arrows show metal salt clusters on the GDL surface, yellow arrows point out the nanoparticles anchored onto N-CNTs, and red arrows show K-rich areas.

The relative metal ratios do not change significantly after synthesis; i.e., the original mixed salt metal ratios are essentially maintained in the fabricated electrodes (Table S3-9). However, as discussed previously, Ni is present in the purchased N-CNTs; the presence of this Ni may skew the amount of Ni detected. Since the amount of Co added to two of the electrodes

was small, the Mn to Zn metal ratios (in the metal salt) added during synthesis is compared with the metal ratios in the synthesized oxides of the electrodes (Figure 3-14). The ratios for both cases are approximately the same, although the Mn:Zn ratios in the electrodes are consistently larger than those in the added salts (above black line in Figure 3-14), particularly for the ZNMCO/N-CNT-[1:1:5:1]-An sample.

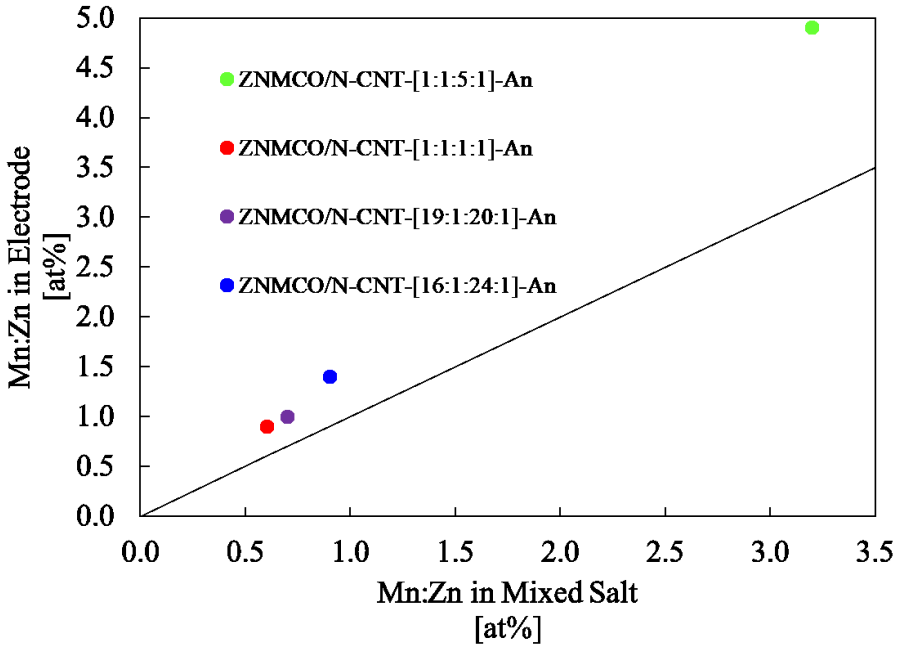

Figure 3-14 Relative Mn to Zn metal ratio for tetra-metallic oxides. The black line represents a one-to-one correspondence between the electrode composition and the mixed salt composition.

STEM BF and HAADF images (Figure 3-15a,b) of ZNMCO/N-CNT-[16:1:24:1]-An before cycling show the oxide nanoparticles and nanoparticle clusters anchored onto the N-CNTs and surrounding them. The Ni EDX map (Figure 3-15d) shows that Ni covers the entire surface of the N-CNTs, which was noted previously and discussed for the tri-metallic oxides. EDX maps for Zn, Mn, and Co (Figure 3-15c, e-f) overlap with one another and correlate with particles anchored to the N-CNTs and nanoparticle clusters. The SAD pattern in Figure 3-15h can be indexed to hetaerolite, $ZnMn_2O_4$, which has a tetragonal spinel structure (a = 0.572 nm and c = 0.925 nm) [104], [105]. Since the Mn:Zn ratio (1.4:1, Figure 3-14) is less than 2, this indicates that a complex spinel composition forms with some partial substitution of Ni and Co for Zn and Mn [106]. This will be discussed further after the XPS results are presented.

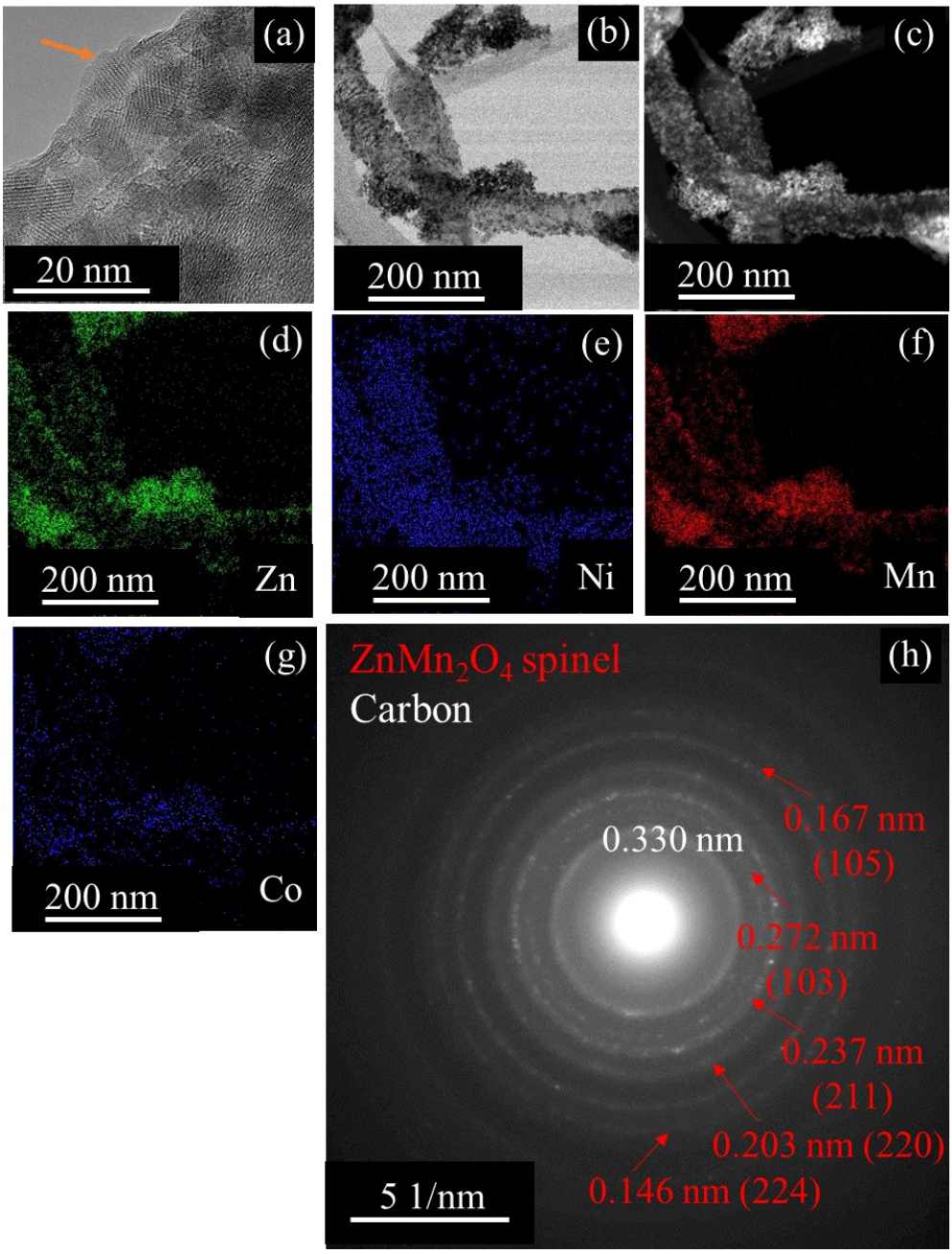

Figure 3-15 TEM/STEM analysis of ZNMCO/N-CNT-[16:1:24:1]-An before cycling. (a) HRTEM image, (b) STEM BF image, (c) STEM HAADF image, (d)-(g) EDX elemental maps for Zn, Ni, Mn, and Co, and (h) SAD pattern. Orange arrow in (a) indicates a nanoparticle on N-CNTs.

XPS analysis of ZNMCO/N-CNT-[16:1:24:1]-An was done to further elucidate the tetra-metallic oxide structure (Figure 3-16). The survey spectrum (Figure 3-16a) shows C, O, Mn, Ni,

F, Co, Na, and Zn peaks. Ni was detected; however, as with Co the amount of Ni present is very low and the F Auger peak (binding energy of 861 eV) overlaps the Ni signal. Thus, the Ni and Co analysis have significant uncertainties. Fluorine and sodium are present due to the PTFE in the GDL and the NaOH used during synthesis, respectively. The high-resolution spectra for Zn 2p, Ni 2p, Mn 2p, Co 2p, Mn 3s, and O 1s are shown in Figure 3-16b-e and Figure S3-21d and S3-21g. Four peaks, at approximately 530 eV, 532 eV, 534 eV, and 535 eV can be fit to the O 1s spectrum. Lattice oxygen (M-O-M bonds), hydroxides (M-O-H and H-O-H bonds), carbide (C-O-C bonds), and the Na KLL Auger peak can be attributed to the binding energies, respectively [80], [102], [107], [108]. Determination of valence for each component was done by deconvolution of the Ni $2p_{3/2}$, Co $2p_{3/2}$, Mn $2p_{3/2}$, and Zn $2p_{3/2}$ peaks (Figure S3-21). From the high-resolution spectra the valences can be estimated (Table 3-4). To determine the valence of Zn, both the Zn LMM (Auger) and 2p peaks were analyzed (Figure S3-21a-b). The kinetic energy for the Zn LMM Auger peak corresponds to ~988 eV. The Zn LMM Auger peak and the Zn $2p_{3/2}$ peak (binding energy of ~1022 eV) confirm that these peaks correspond to Zn-O bonds, meaning Zn has a valence of 2+ [33], [109]. Due to the large interference from the F Auger peak, the Ni valence was determined by the relative percentage of each valence from the high-resolution spectrum (Figure S3-21e), leading to an average valence of 2.4 (Table 3-4). Additionally, the high-resolution spectrum of Co $2p_{3/2}$ (Figure S3-21f) can be fit to 3+ multiplet peaks, resulting in a valence of 3.0 for Co. To determine the valence of Mn, both Mn $2p_{3/2}$ and Mn 3s high resolution spectra were used (Figure S3-21c-d). Deconvolution of the Mn $2p_{3/2}$ peak gives an average valence of 3.4. The Mn 3s peak has a peak splitting of 4.7 eV, which correlates to an average valence of 3.7 (Table 3-4) [95], [97], [101], [102]. Taking the average between both approaches gives an average valence of ~3.5.

Table 3-4 XPS analysis from high resolution spectra; average valences are calculated based on at% of each valence

Sample	Ni 2p 3/2			Co 2p 3/2			Mn 2p 3/2				Mn 3s	
	2+ (%)	3+ (%)	Average Valence	2+ (%)	3+ (%)	Average Valence	2+ (%)	3+ (%)	4+ (%)	Average Valence	Peak Splitting (eV)	Average Valence*
ZNMCO/N-CNT-[16:1:24:1]-An	58.1	41.9	**2.4**	0.0	100.0	**3.0**	0.0	57.0	43.0	**3.4**	4.7	**3.7**

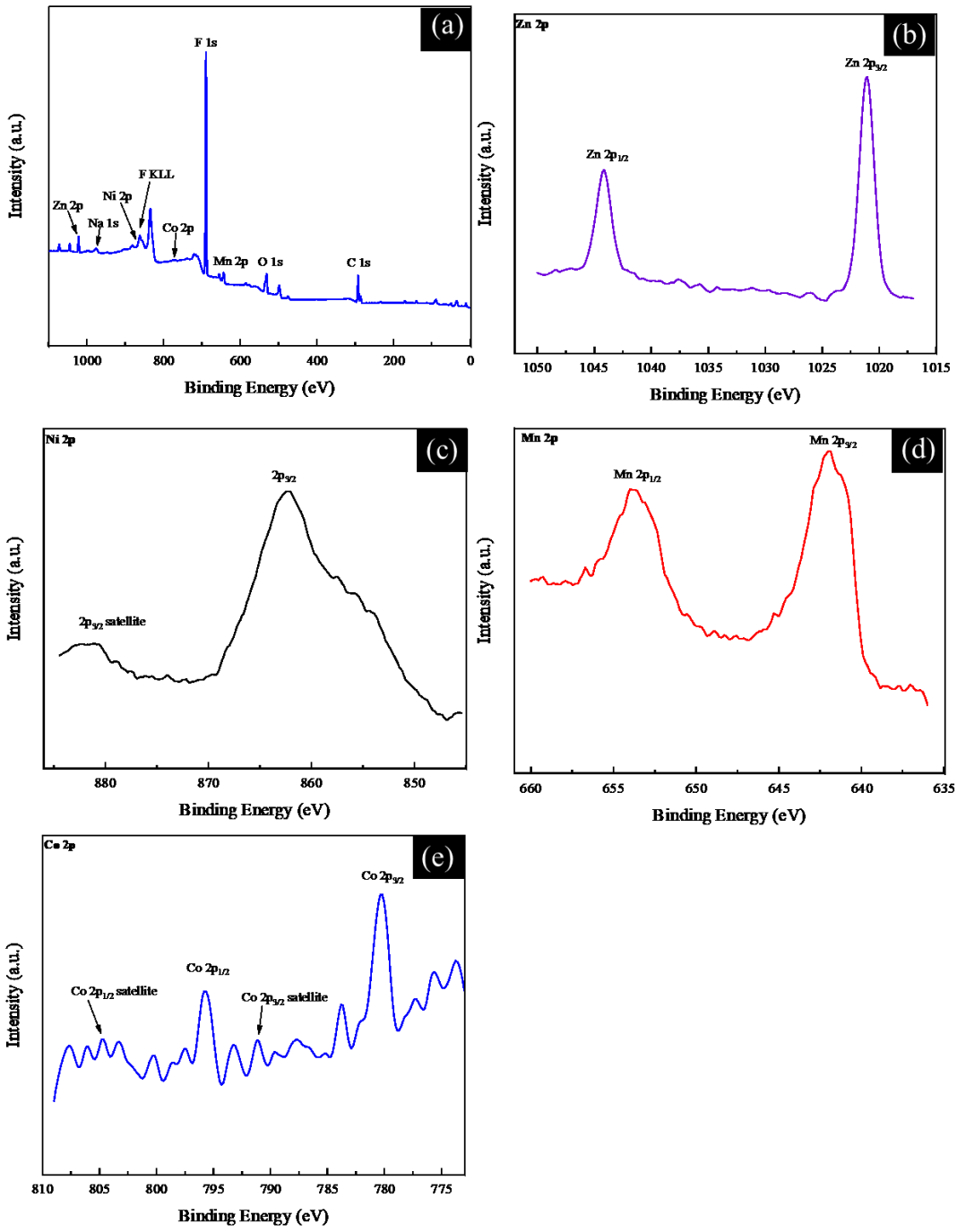

Figure 3-16 XPS spectra for ZNMCO/N-CNT-[16:1:24:1]-An. (a) Survey spectrum, (b) Zn 2p, (c) Ni 2p, (d) Mn 2p, and (e) Co 2p high-resolution spectra.

Based on the XPS and TEM/STEM analysis, the metallic oxide anchored onto the N-CNTs is a spinel phase. TEM analysis shows a tetragonal spinel phase, meaning that for every four oxygen atoms, three metal atoms are needed. The SEM EDX and STEM analysis show

good agreement, with a Mn:Zn ratio of 1.4 from SEM EDX analysis and a ratio of 1.2-1.5 from STEM analysis. The margin of error is likely from the sampling volume. SEM analysis was done over the total GDL surface, while STEM analysis investigated the local composition on N-CNTs. From the XPS analysis, Zn and Ni have a 2+ valence state while Co has a valence of 3+. Mn has a mixed oxidation state of 3+ and 4+. The oxide structure is likely $(Zn,Ni)(Co,Mn)_2O_4$, with Ni partially substituting for Zn and Co partially substituting for Mn. This structure is further confirmed by SEM analysis as the (Mn+Co):(Zn+Ni) ratio is 1.4:1. As explained earlier, the lower ratio is due to the Mn having a mixed valence of 3+ and 4+ [110]. Zn 2+ and Ni 2+ are likely in tetrahedral sites, while the Co 3+ and Mn species are in octahedral sites [104].

3.4. Conclusions

Tri-metallic, Ni-Mn-Co oxides (NMCO) and tetra-metallic, Zn-Ni-Mn-Co oxides (ZNMCO) anchored onto N-CNTs were successfully synthesized and impregnated into a porous, carbon-based gas diffusion layer (GDL) using a simple one-step method. The best performing tri-metallic oxides were NMCO/N-CNT-[1:9:4]-An, with an efficiency of 58.4% at 20 mA/cm^2, and NMCO/N-CNT-[1:5:1] with a maximum power density of 116 mW/cm^2. ZNMCO/N-CNT-[16:1:24:1]-An was the best tetra-metallic oxide with an efficiency of 57.2% (at 20 mA/cm^2) and a maximum power density of 134 mW/cm^2. These performance specifications compare quite favorably with the baseline Pt-Ru/C catalyst. The addition of Zn to Ni-Mn-Co oxides improved stability as well as the OER potential during bifunctional cycling. ZNMCO/N-CNT-[16:1:24:1]-An maintained an efficiency of 56.4% after 200 charge/discharge cycles at 10 mA/cm^2. Both tri-metallic and tetra-metallic oxides outperformed Pt-Ru/C during cycle testing.

3.5. Supporting Information

Table S3-5 Reference data used in the DOE for determination of Ni-Mn-Co and Zn-Ni-Mn-Co oxide compositions

$Zn(CH_3COO)_2 \bullet 4(H_2O)$ [mg]	**$NiO_4S \bullet 7(H_2O)$ [mg]**	**$Mn(CH_3COO)_2 \bullet 4(H_2O)$ [mg]**	**$Co(CH_3COO)_2 \bullet 4(H_2O)$ [mg]**	**Annealed / Unannealed**	**Potential Gap [V @ 20 mA/cm^2]**	**Efficiency [% @ 20 mA/cm^2]**	**Reference**
0	0	250	0	Unannealed	0.94	56.1	[46]
0	250	0	0	Unannealed	1.11	49.1	[95]
0	105	105	0	Unannealed	0.97	54.2	[95]
0	175	35	0	Unannealed	0.98	53.8	[95]
0	35	175	0	Unannealed	0.90	57.1	[95]
0	105	0	105	Unannealed	0.92	55.6	[95]
0	175	0	35	Unannealed	0.89	56.8	[95]
0	35	0	175	Unannealed	0.95	54.5	[95]
70	0	70	70	Unannealed	0.88	56.7	[98]
70	0	70	70	Annealed	0.87	57.8	[98]

Table S3-6 Baseline data used in the DOE for determination of Ni-Mn-Co and Zn-Ni-Mn-Co oxide compositions

$Zn(CH_3COO)_2 \bullet 4(H_2O)$ [mg]	**$NiO_4S \bullet 7(H_2O)$ [mg]**	**$Mn(CH3COO)2 \bullet 4(H_2O)$ [mg]**	**$Co(CH_3COO)_2 \bullet 4(H_2O)$ [mg]**	**Annealed / Unannealed**	**Potential Gap [V @ 20 mA/cm^2]**	**Efficiency [% @ 20 mA/cm^2]**
0	70	70	70	Unannealed	0.88	57.1
0	70	70	70	Annealed	0.93	54.9
0	150	30	30	Unannealed	0.94	54.4
0	150	30	30	Annealed	0.95	53.7
0	30	150	30	Unannealed	0.87	57.8
0	30	150	30	Annealed	0.95	54.1
0	30	30	150	Unannealed	0.89	56.6
0	30	30	150	Annealed	0.93	54.7
0	110	50	50	Unannealed	0.95	53.5
0	110	50	50	Annealed	1.08	47.8
0	50	110	50	Unannealed	0.91	55
0	50	110	50	Annealed	0.96	53.1
0	50	50	110	Unannealed	0.91	55.0
0	50	50	110	Annealed	0.88	56.7
105	105	0	0	Unannealed	1.07	48.6
105	105	0	0	Annealed	1	51.2
35	175	0	0	Unannealed	1	51.2
35	175	0	0	Annealed	1.06	48.8
175	35	0	0	Unannealed	0.95	53.7
175	35	0	0	Annealed	0.96	53.4
70	70	70	0	Unannealed	0.96	53.6
70	70	70	0	Annealed	1.02	51.9

70	70	0	70	Unannealed	0.94	54.4
70	70	0	70	Annealed	1.13	46.3
105	105	0	0	Unannealed	1.07	48.6
105	105	0	0	Annealed	1	51.2
35	175	0	0	Unannealed	1	51.2
35	175	0	0	Annealed	1.06	48.8
175	35	0	0	Unannealed	0.95	53.7
175	35	0	0	Annealed	0.96	53.4
70	70	70	0	Unannealed	0.96	53.6
70	70	70	0	Annealed	1.02	51.9
70	70	0	70	Unannealed	0.94	54.4
70	70	0	70	Annealed	1.13	46.3
52.5	52.5	52.5	52.5	Unannealed	1.09	47.8
52.5	52.5	52.5	52.5	Annealed	1.25	41.9
131.25	26.25	26.25	26.25	Unannealed	1.05	50
131.25	26.25	26.25	26.25	Annealed	1.02	51
26.25	131.25	26.25	26.25	Unannealed	1.04	50
26.25	131.25	26.25	26.25	Annealed	1.08	48.1
26.25	26.25	131.25	26.25	Unannealed	0.91	55.6
26.25	26.25	131.25	26.25	Annealed	0.89	56.8
26.25	26.25	26.25	131.25	Unannealed	1.04	49.8
26.25	26.25	26.25	131.25	Annealed	0.98	52.9

Table S3-7 Summary of DOE predicted compositions electrochemical rate tests for tri-metallic oxides at 20 mA/cm^2

Sample	Ni:Mn:Co salt [mg]	ORR [V]	OER [V]	Potential Gap [V]	Efficiency [%]	Mass Loading [mg/cm^2]
#1 NMCO/N-CNT-[1:9:4]*	15:135:60	1.08	2.13	1.05	50.7	2.33
#2 NMCO/N-CNT-[1:9:4]-An*	15:135:60	1.19	2.04	0.85	58.4	2.42
#3 NMCO/N-CNT-[1:24:17]	5:120:85	1.06	2.08	1.02	51.0	1.45
#4 NMCO/N-CNT-[1:24:17]-An	5:120:85	1.15	2.07	0.92	55.6	2.01
#5 NMCO/N-CNT-[1:23:18]	5:115:90	1.00	2.11	1.11	47.4	2.20
#6 NMCO/N-CNT-[1:23:18]-An	5:115:90	1.13	2.09	0.96	54.1	2.20
#7 NMCO/N-CNT-[1:29:12]	5:145:60	1.06	2.06	1.00	51.5	2.39
#8 NMCO/N-CNT-[1:29:12]-An	5:145:60	1.19	2.06	0.87	57.8	2.33
#9 NMCO/N-CNT-[12:1:1]	180:15:15	1.05	2.08	1.03	50.5	2.45
#10 NMCO/N-CNT-[12:1:1]-An	180:15:15	1.06	2.08	1.02	51.0	2.20

#11 NMCO/N-CNT-[1:12:1]	15:180:15	1.19	2.08	0.89	57.2	1.45
#12 NMCO/N-CNT-[1:12:1]-An	15:180:15	1.19	2.07	0.88	57.5	2.77
#13 NMCO/N-CNT-[1:1:12]	15:15:180	1.12	2.06	0.94	54.4	2.52
#14 NMCO/N-CNT-[1:1:12]-An	15:15:180	1.13	2.07	0.94	54.6	1.95
#15 NMCO/N-CNT-[1:40:1]	5:200:5	1.11	2.07	0.95	53.8	2.08
#16 NMCO/N-CNT-[1:40:1]-An	5:200:5	1.10	2.06	0.96	53.4	2.08

*Results are an average of 4 tests

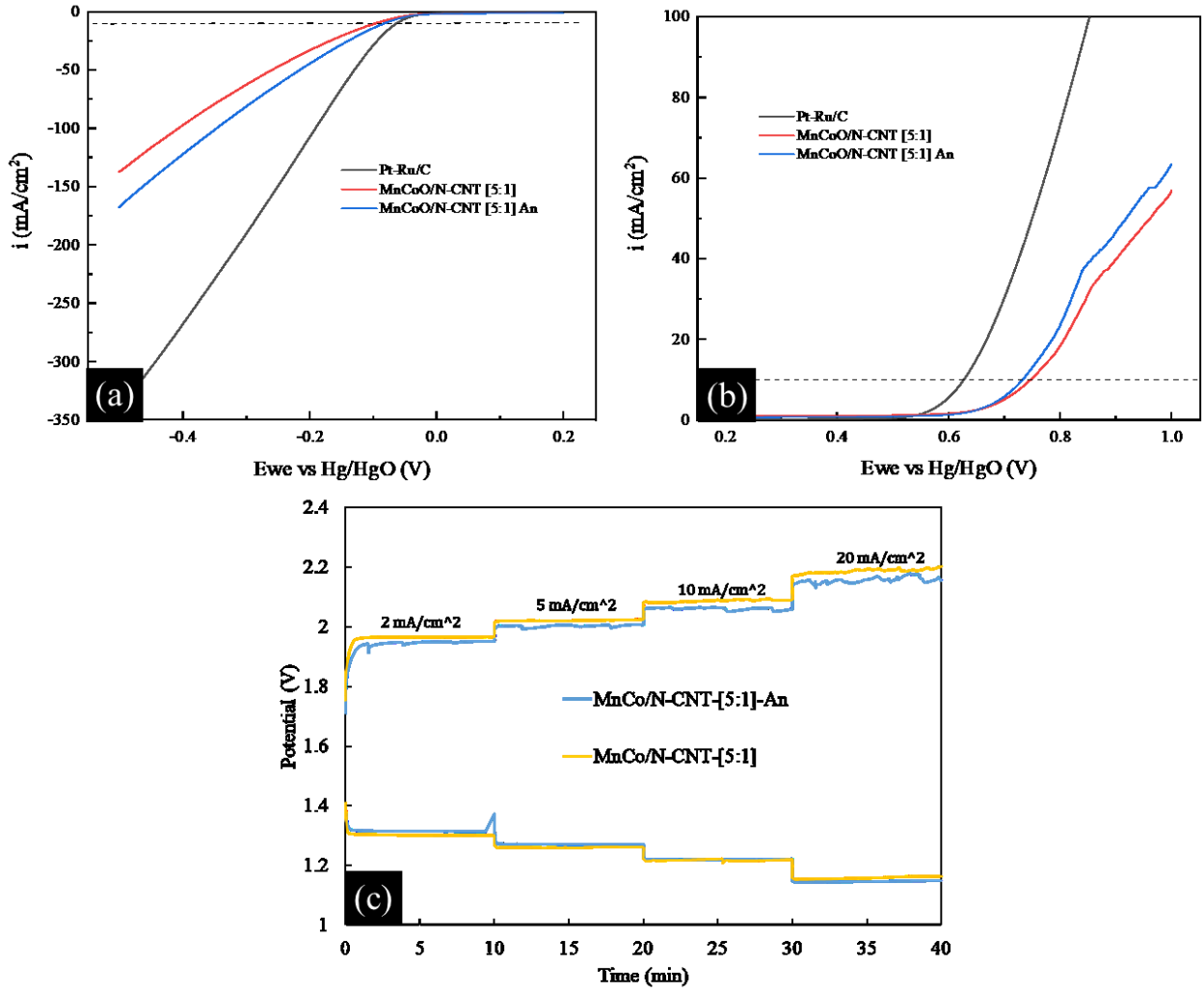

Figure S3-17 Electrochemical testing results for MnCoO/N-CNT samples. (a) ORR LSV measurements, (b) OER LSV measurements, and (c) battery rate tests.

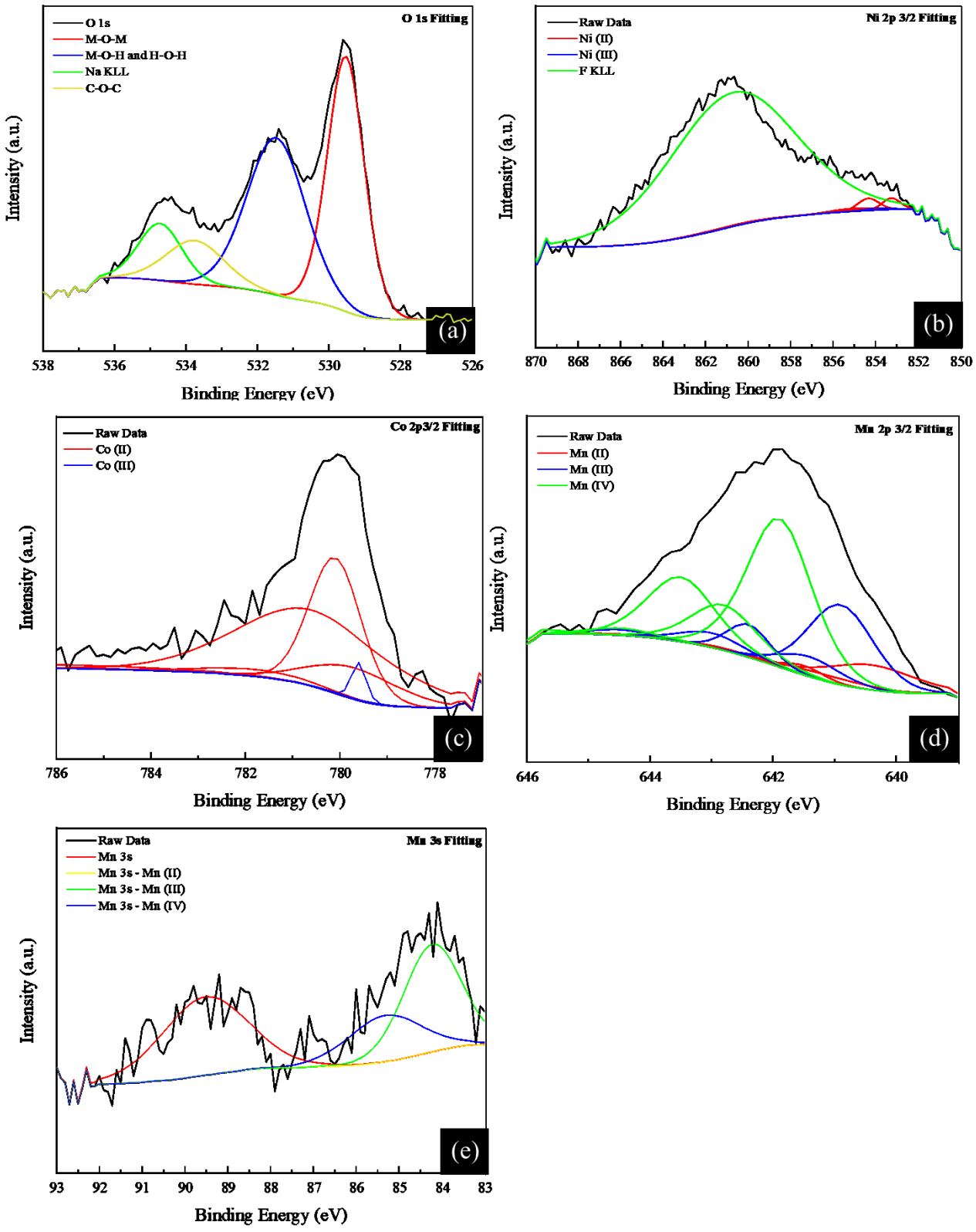

Figure S3-18 XPS fitting data for NMCO/N-CNT-[1:9:4]-An. (a) O 1s, (b) Ni $2p_{3/2}$, (c) Co $2p_{3/2}$, (d) Mn $2p_{3/2}$, and (e) Mn 3s peaks.

Table S3-8 Summary of DOE predicted compositions and electrochemical rate tests for tetra-metallic oxides at 20 mA/cm^2

Sample	Zn:Ni:Mn:Co salt [mg]	ORR [V]	OER [V]	Potential Gap [V]	Efficiency [%]	Mass Loading [mg/cm^2]
#17 ZNMCO/N-CNT-[16:1:24:1]	80:5:120:5	1.11	2.01	0.91	54.9	2.08
#18 ZNMCO/N-CNT-[16:1:24:1]-An	80:5:120:5	1.15	2.01	0.88	57.2	2.45
#19 ZNMCO/N-CNT-[19:1:20:1]	97:5:103:5	0.94	2.01	1.08	46.4	2.33
#20 ZNMCO/N-CNT-[19:1:20:1]-An	97:5:103:5	1.09	2.01	0.92	54.2	2.83

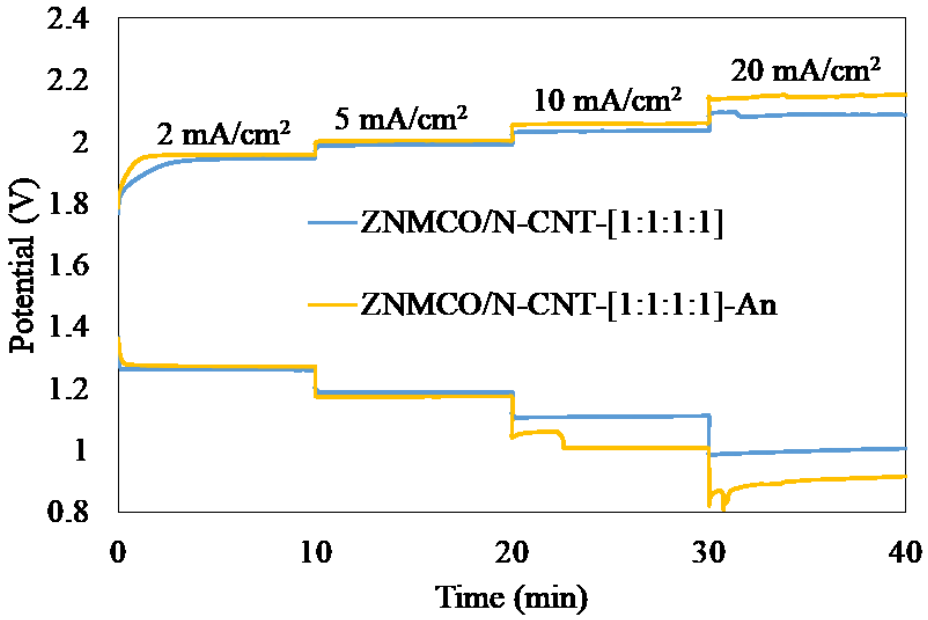

Figure S3-19 Full cell battery testing for ZNMCO/N-CNT-[1:1:1:1] samples.

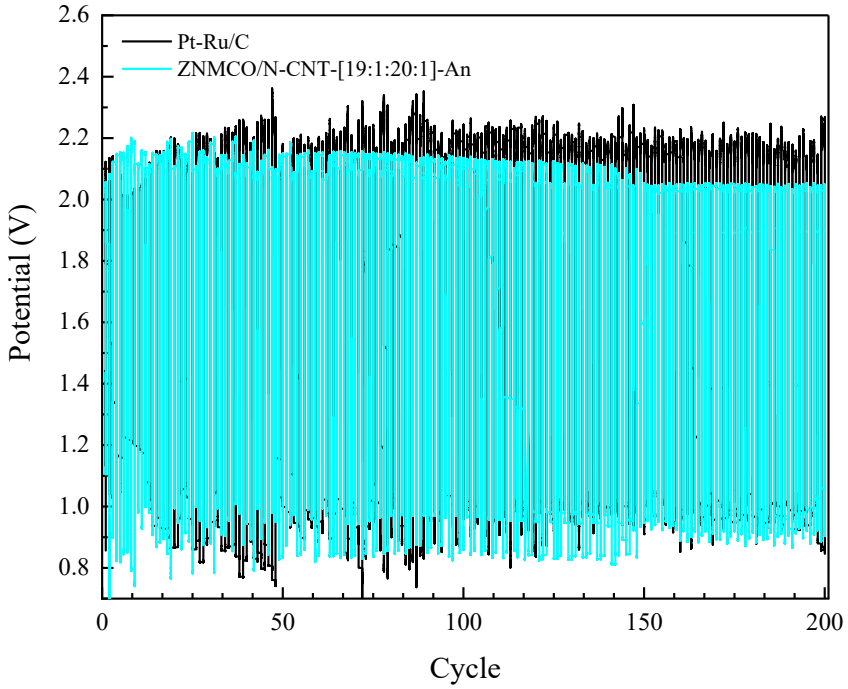

Figure S3-20 Cycling data for ZNMCO/N-CNT-[19:1:20:1]-An, and Pt-Ru/C. Bifunctional cycling was done using a homemade Zn-air battery at a current density of 10mA/cm^2 with 200 cycles (30 min per cycle) in 6 M KOH + 0.25 M ZnO.

Table S3-9 Composition comparison between metal salt added during synthesis and the amount of metal in the prepared electrode

Sample	**Metal Ratio Mixed Salts [Zn:Ni:Mn:Co, at%]**	**Relative Metal Ratio in GDL [Zn:Ni:Mn:Co, at%]**
ZNMCO/N-CNT-[1:1:5:1]-An	[1.6:1:5.1:1.1]	[1.2:1:5.9:1.1]
ZNMCO/N-CNT-[1:1:1:1]-An	[1.6:1:1:1.1]	[1.3:1:1.1:1.3]
ZNMCO/N-CNT-[19:1:20:1]-An	[30.8:1:20.6:1.1]	[13:1:13.3:0.7]
ZNMCO/N-CNT-[16:1:24:1]-An	[25.4:1:24:1.1]	[13.5:1:19.1:1]

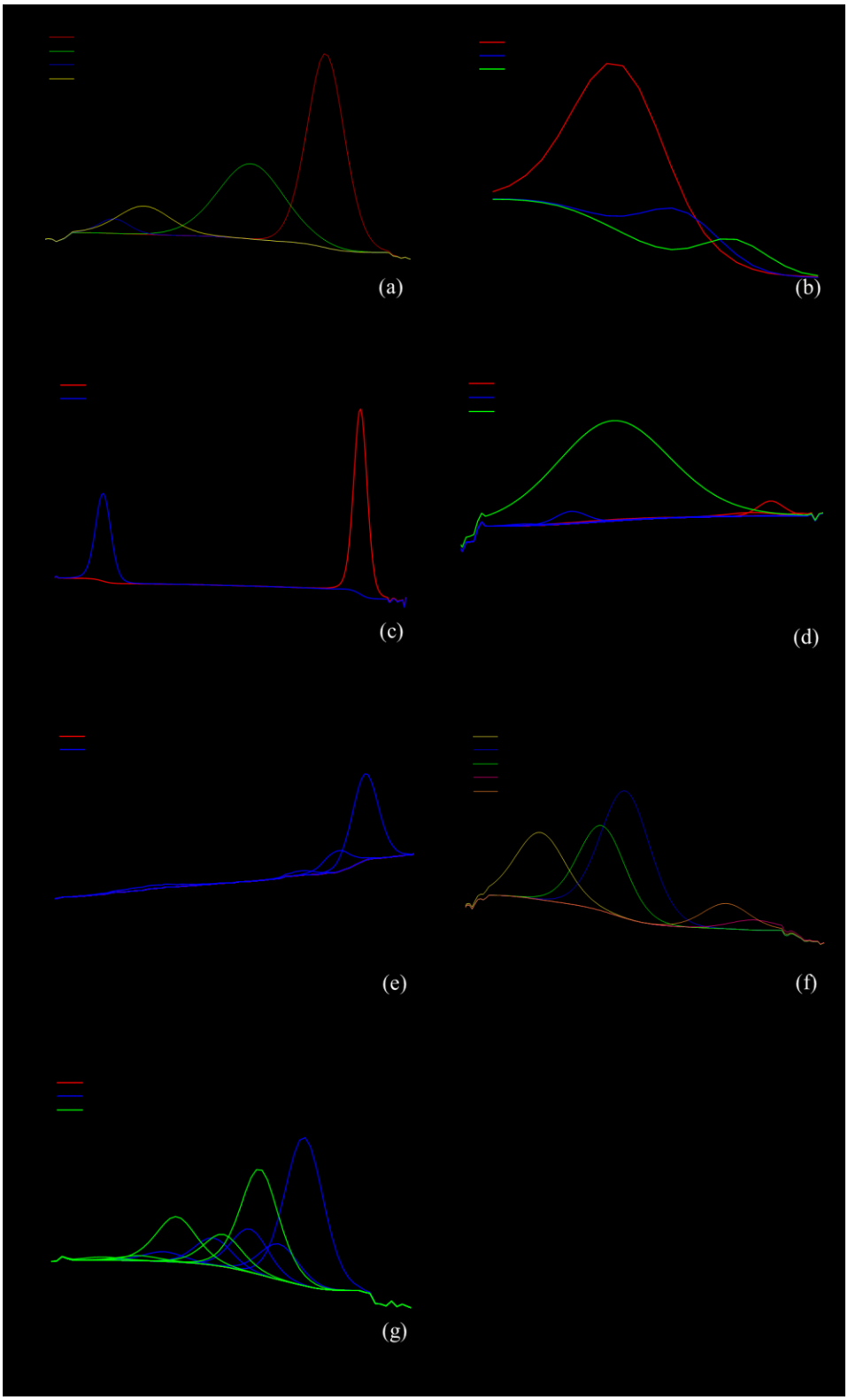

Figure S3-21XPS fitting data for ZNMCO/N-CNT-[16:1:24:1]-An. (a) O 1s, (b)-(c) Zn 2p, (d) Ni $2p_{3/2}$, (e) Co $2p_{3/2}$, (f) Mn $2p_{3/2}$, and (g) Mn 3s peaks.

4.0. Transition Metal Oxides Anchored onto N,S-Co-Doped Carbon Nanotubes as Bifunctional Electrocatalysts for Zinc-Air Batteries

4.1. Introduction

Wind and solar energy are becoming more popular, since traditional energy sources (e.g., oil, natural gas etc.) are not sustainable and cause harm to the environment. However, these renewable energy resources provide intermittent energy requiring a sustainable method of energy storage. A common storage method is batteries. Metal-air batteries, specifically Zn-air batteries (ZABs) have become more popular over the past decade. Compared to commonly used Li-ion and lead acid batteries, ZABs have a higher theoretical energy potential, lower cost, and are environmentally safer [22]. Similar to Li-ion batteries, ZABs have drawbacks. The main issues with ZABs are the slow oxygen reduction and evolution reaction (ORR/OER) kinetics at the air electrode [7], [22]. Catalysts are used to improve ORR and OER kinetics. Precious metals like Pt, Ru, and Ir are commonly used to improve the reaction kinetics [7], [22]. However, precious metals are expensive, have poor cycling stability, and complicate the fabrication process.

A promising alternative to precious metal catalysts are transition metal oxides (e.g., Mn, Co, Zn, Ni, etc.). Transition metal oxides are often combined with nanostructured carbon materials (e.g., carbon nanotubes (CNTs), graphene, and carbon black (CB)) because the synergism between these materials improves the electrochemical properties. Studies have shown that doping the carbon nanostructures with heteroatoms (e.g., N, S, P, and B) improves the ORR and OER performance by providing more active sites for the catalyst [22], [39], [44], [111]. Heteroatoms positively alter the electrochemical properties of carbon [43], [112]. Nitrogen is popular since the N-atom can provide both n- and p-type doping, which is good for donating (ORR) and accepting (OER) an electron, respectively [42]. S is another commonly used dopant as it is thought to maintain charge neutrality of the carbon, polarization of electron pairs, and production of charge positions [44]. Co-doping heteroatoms with N (e.g., N,S-, N,P-, and N,B-) onto carbon materials has shown promising results in further improving reaction kinetics [113]. Co-doping N and S onto carbon materials initiates defect sites (non-neutral electron sites), which

facilitate four electron transfer for efficient ORR activity [23], [44], [114], [115], [116]. Like the N atoms, S atoms can easily substitute for the C atoms when co-doped with nitrogen [115]. Geng *et al.* [114] impregnated a cobalt sulfide into N,S-co-doped graphene which had comparable OER activity to a Pt/C catalyst. Wu *et al.* [43] synthesized N, F, and P doped carbon fibers, which had stable bifunctional cycling and a round trip efficiency (ratio of the ORR potential to the OER potential) of ~57.5% at 10 mA/cm^2 for ~22 h. Another group fabricated a porous 2D Co-Fe composite on N,S doped carbon which had a power density of 169 mW/cm^2 and an overall bifunctional efficiency (ratio of the ORR potential to the OER potential) of 56.8% at 10 mA/cm^2 for 255 cycles [51]. Guan *et al.* [39] synthesized an Fe-Ni catalyst on S and N doped carbon (Fe,Ni-SNC) through pyrolysis. The resulting catalyst had a maximum power density of 291 mW/cm^2, which outperformed Pt-C + IrO_2 (211 mW/cm^2), and maintained a highly stable bifunctional cycling efficiency of 60% for 140 discharge/charge cycles at 5 mA/cm^2. Jiang *et al.* [44] used fish bones as a precursor for producing nitrogen and sulfur co-doped carbon fibers (NSCFs) and embedded a tri-metallic sulfide, $(Fe,Co,Ni)_9S_8$, into the carbon structure. The resulting $(Fe,Co,Ni)_9S_8$/NSCFs had a maximum power density of 138 mW/cm^2 and an overall bifunctional cycling efficiency of 56% at 10 mA/cm^2 for 360 discharge/charge cycles, outperforming Pt/C + RuO_2 precious metal catalyst [44].

Chapter 3 of this thesis explored different tri-metallic (Ni-Mn-Co) oxide and tetra-metallic (Zn-Ni-Mn-Co) oxide compositions anchored onto N-CNTs. The overall bifunctional cycling efficiency (after cycling) was about 53% for the best tri-metallic oxide, while the best tetra-metallic oxide had a bifunctional cycling efficiency of ~56%; both were tested at 10 mA/cm^2 for 200 discharge/charge cycles. The addition of Zn with Ni-Mn-Co transition metals improved the bifunctional efficiency and improved the maximum power density (134 mW/cm^2), which exceeded that of Pt-Ru/C (120 mW/cm^2).

This chapter investigates the effect of anchoring tri-metallic (Ni-Mn-Co) and tetra-metallic oxides onto S doped N-CNTs (N,S-CNTs) impregnated into a gas diffusion layer (GDL) made of porous carbon paper. The impregnation method of electrode fabrication has proven to deposit the catalyst material throughout the gas diffusion layer (GDL), thus increasing the electrode performance [46], [91], [95], [98]. The best Ni-Mn-Co oxide and Zn-Ni-Mn-Co oxide from the previous study were chosen for this study. To the best of the author's knowledge,

no studies have been done on Ni-Mn-Co oxides and Zn-Ni-Mn-Co oxides anchored onto N,S-CNTs in tandem with the impregnation technique for electrode preparation.

4.2. Experimental

4.2.1. Synthesis of S-doped N-CNTs

The method of synthesis was derived from several methods of co-doping heteroatoms onto carbon nanotubes [115], [117], [118]. To synthesize co-doped S and N CNTs, thiourea and pre-purchased N-CNTs were combined together. 200 mg, 400 mg, 600 mg, and 1000 mg of thiourea were combined with 100 mg of N-CNTs and ground into a fine powder using a pestle and mortar. The fine powder was then placed into a tube furnace under Ar flow (0.05 L/min), with a heating rate of 5 °C/min until 700°C was reached and held for 1 h. For simplicity N-CNTs doped with 200 mg of thiourea are denoted as N,S-CNTs-200, 400 mg of thiourea is denoted as N,S-CNTs-400 and so on.

4.2.2. Synthesis of Electrocatalyst and Electrode Preparation

The method of synthesis for creating the electrocatalysts used a procedure previously developed in our group and described in Chapter 3 [46]. This method involved creating a catalyst precursor mixture and vacuum filtering the solution through the catalyst soaked GDL. The catalyst precursor included 50 mg of N,S-CNTs and 210 mg of a metal salt mixture, with ~80 mg of NaOH and 10 mL of ethanol in a glass vial. The metal salt mixtures chosen were based on the best electrochemical results in Section 3.3.1.1 and Section 3.3.2.1. The Ni-Mn-Co oxide was synthesized using 15 mg of $NiO_4S \bullet 7(H_2O)$, 135 mg of $Mn(CH_3COO)_2 \bullet 4(H_2O)$, and 60 mg of $Co(CH_3COO)_2 \bullet 4(H_2O)$; the Zn-Ni-Mn-Co oxide was synthesized using 80 mg of $Zn(CH_3COO)_2 \bullet 4(H_2O)$, 5 mg of $NiO_4S \bullet 7(H_2O)$, 120 mg of $Mn(CH_3COO)_2 \bullet 4(H_2O)$, and 5 mg of $Co(CH_3COO)_2 \bullet 4(H_2O)$. Next the catalyst mixture was mechanically stirred for 10 min at about 800 rpm and then placed in a bath sonicator and sonicated for 5 h. An additional 15 mL of ethanol, a piece of GDL (4.5 cm diameter circle), along with 1 mL of Nafion 5% was further sonicated for 20 min and dried in air for 5 min. The catalyst soaked GDL acted as a filter paper and ~7 mL of the catalyst solution was vacuum filtered through the GDL. Various samples were annealed for 30 min at 300°C. Annealing samples at these conditions showed improved

electrochemical performance in previous studies [46], [95]. For ease of understanding, the samples were labeled based on the elements included and the metal salt mass ratio in the catalyst mixture; e.g., Ni-Mn-Co oxide with a metal salt ratio of [1:1:1] anchored onto N and S co-doped CNTs is denoted as NMCO/N,S-CNT-[1:1:1]. The ratios do not represent the actual amount of metal in the synthesized catalyst but are the amount of metal salt added to the catalyst mixture. The suffix 'An' depicts annealed samples. The mass loading of each sample is based on the difference in the mass of the GDL samples after synthesis and the mass of the GDL samples before synthesis, divided by the area of the GDL (15.9 cm^2).

Using the spray coating method, a Pt-RuO_2/C catalyst was prepared for baseline comparison. 50 mg of Pt-RuO_2/C (30% Pt, 15% RuO_2 on carbon black; from Alfa Aesar), 2 mL of deionized water, 1 mL of ethanol, and 0.1 mL of Nafion (5 wt%) were used for the catalyst suspension. An air brush was utilized to coat a 3 cm x 7 cm piece of GDL with the catalyst suspension. The spray coated GDL was placed in a vacuum and oven heated to 60°C for 0.5 h to activate the Nafion and improve the adhesion of the Pt-RuO_2/C on the GDL. From this point on the Pt-RuO_2/C on GDL is denoted as Pt-Ru/C and had a mass loading of 0.5 mg/cm^2.

4.2.3. Microstructural Characterization

CHNS analysis (Thermofisher Organic Elemental Analyzer, FLASH 2000, CHNS-O analyzer) was done using a thermal conductivity detector (TCD). The gases used were helium as the carrier (140 mL/min), oxygen for combustion (5 s at 250 mL/min), and a helium reference gas (100 mL/min). Each run was 720 s with a 12 s sampling delay. Peak calibration used BBOT, 2.5-Bis(5-tert-butyl-benzoxazol-2-yl)thiophene. Scanning electron microscopy (Tescan VEGA3 SEM and Zeiss Sigma field emission SEM), including energy dispersive X-ray (EDX) spectroscopy, was done at accelerating voltages of 5 kV and 20 kV (EDX analysis), while transmission/scanning transmission electron microscopy (JEOL JEM-ARM200CF TEM/STEM), coupled with EDX analysis, was done at 200 kV. For SEM sample preparation, a 1 cm x 1 cm section of the prepared electrode was placed onto double-sided carbon tape mounted on an Al stub. TEM samples were prepared by scraping the catalyst material from the GDL and combining with 2 mL of ethanol. The catalyst suspension was then sonicated for ~20 min, dropped onto a carbon-coated, Cu grid and air dried. X-ray photoelectron spectroscopy (Versa Probe III (PHI 500) XPS) was done using a monochromatic Al-K_α x-ray source and a pass

energy of 20 eV. The XPS samples were prepared by cutting the catalyst impregnated GDL into small pieces. Spectra were calibrated using the C 1s peak at a binding energy of 248.8 eV.

4.2.4. Electrochemical Testing

Electrochemical testing was done using BioLogic VSP-100, SP300, and Arbin LBT20084 potentiostats. Linear sweep voltammetry (LSV) was done using a three-electrode setup in oxygen saturated 1 M KOH at a scan rate of 5 mV/s. The catalyst impregnated electrode (1 cm x 2 cm) was the working electrode, a Pt coil was the counter electrode, and Hg/HgO (0.098 V vs. RHE) was the reference electrode. Homemade vertical and horizontal cells were used for battery testing. 6 M KOH + 0.25 M ZnO was used as the electrolyte, a piece of Zn sheet metal (2 cm x 6 cm x 0.1 cm) was used as one electrode, and the catalyst impregnated GDL (1 cm x 1 cm exposed to electrolyte) was the air electrode, with Ni as the current collector. Rate testing was done using the homemade vertical cell at various current densities (± 2 mA/cm^2, ± 5 mA/cm^2, ± 10 mA/cm^2, and ± 20 mA/cm^2) for 10 min each. The best performing samples at 20 mA/cm^2 during rate testing also underwent bifunctional cycling. Cycling tests were conducted using the homemade horizontal cell. One cycling test consisted of 200 discharge/charge cycles at ±10 mA/cm^2; each cycle was a total of 30 min (5 min rest period, discharge period of 10 min, another 5 min rest period, and a 10 min charge period). All battery testing used Zn/Zn^{2+} as the reference electrode. The potential difference was determined by subtracting the ORR potential from the OER potential. Battery efficiency was obtained by dividing the OER potential by the ORR potential.

4.3. Results and Discussion

4.3.1. N,S-CNTs Analysis

To ensure that S was doped onto the N-CNTs, (S)TEM, EDX, and CHNS analysis were done. TEM images of purchased pristine CNTs, purchased N-CNTs, N,S-CNTs-200 prepared in this work, and N,S-CNTs from the literature are shown in Figure 4-1. There is an obvious difference in the structure of the pristine CNTs (Figure 4-1a), the N-CNTs (Figure 4-1b), and the N,S-CNTs (Figure 4-1c). The pristine CNTs do not have any defects along the nanotubes, while the N-CNTs have a bamboo structure (green arrows) and the N,S-CNTs have a defect bamboo structure that is a dense, random stacking/layering of the bamboo structure (red arrows). The

defects created from doping the CNTs increase the number of active sites, which could improve the catalytic performance.

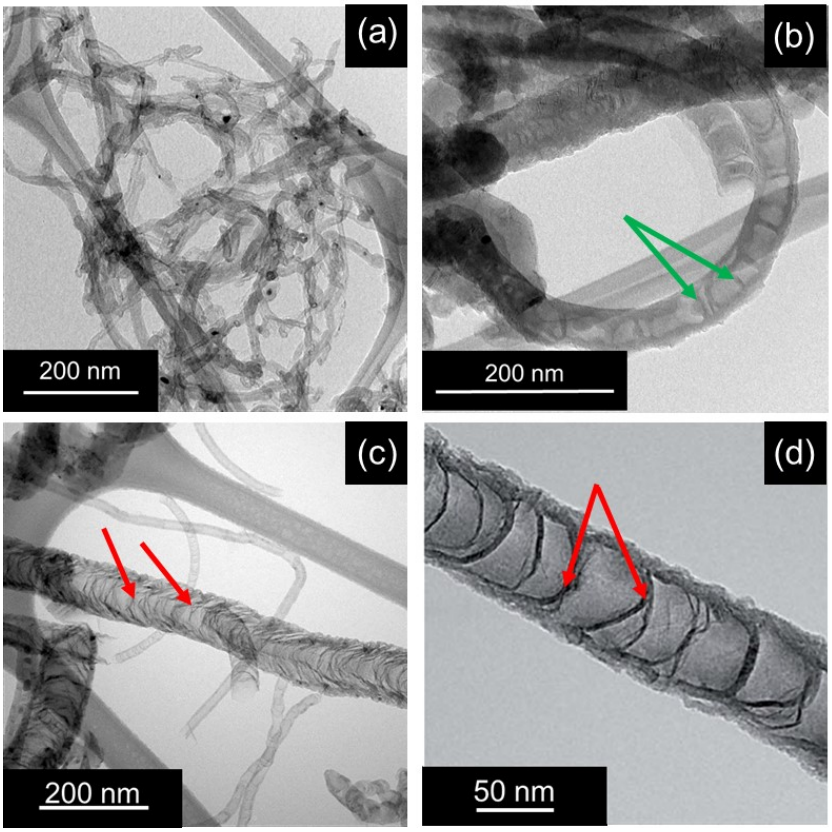

Figure 4-1 TEM BF images. (a) Pristine CNTs, (b) N-CNTs, (c) N,S-CNTs-200 prepared in this work, and (d) N,S-CNTs [23]. The green arrows outline the N induced defect (bamboo) structure and the red arrows outline the N and S induced defect structure on the CNTs.

STEM EDX mapping (Figure 4-2) shows significant overlap between the S and N maps. The relative mass percents of C, N, and S are 96.9 wt%, 2.5 wt%, and 0.6 wt%, respectively. Comparing just the N content to S content there is about four times as much N present as S on the CNTs.

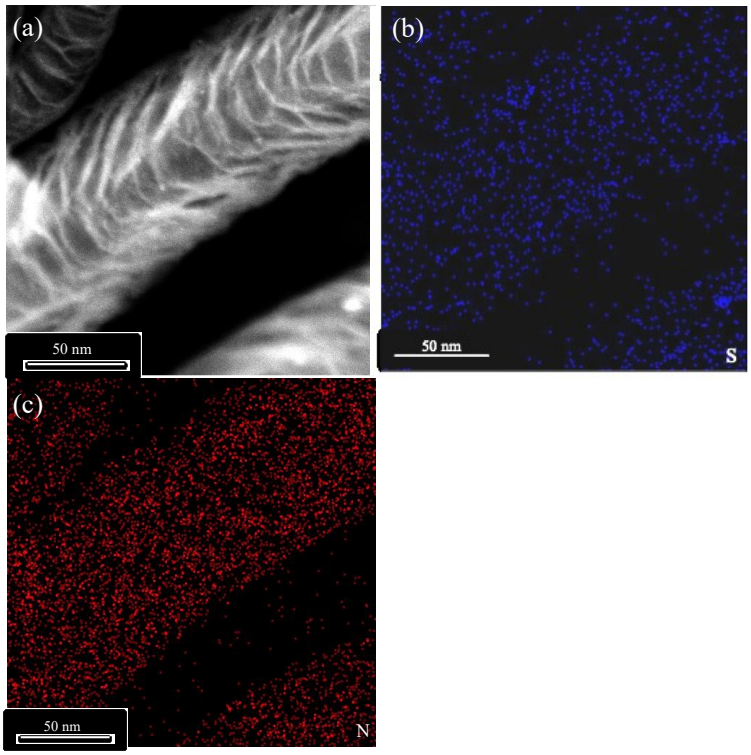

Figure 4-2 (S)TEM EDX images of N,S-CNTs-200. (a) STEM BF image, (b) EDX map of S, and (c) EDX map of N.

CHNS analysis (Table 4-1) was used to compare the sulfur content for the purchased N-CNTs and the S doped N-CNTs (N,S-CNTs). Different amounts of precursor (thiourea) were compared to determine its effect on the sulfur content for the N-CNTs. The amount of precursor is noted in parentheses and the amount of N-CNTs was held constant at 100 mg. The results show the average sulfur content is 0.54 wt% for the synthesized N,S-CNTs and does not vary much with the amount of thiourea, while the purchased N-CNTs contain no sulfur.

Table 4-1 CHNS analysis results comparing N-CNTs with sulfur doped N-CNTs (N,S-CNTs); mass of thiourea added (in g) during synthesis is noted in parentheses

Sample	N [wt%]	C [wt%]	H [wt%]	S [wt%]
N-CNT	4.04	88.15	0.15	0.00
N,S-CNT-200	4.26	90.16	0.05	0.54
N,S-CNT-400	4.28	89.54	0.05	0.58
N,S-CNT-600	4.46	90.08	0.06	0.50
N,S-CNT-1000	4.56	90.23	0.05	0.54

Combining the results from STEM EDX and CHNS analysis, it can be concluded that doping sulfur onto N-CNTs was successful. However, the amount of thiourea added during synthesis did not affect the sulfur content in the N-CNTs.

Figure 4-3 compares electrochemical testing for N-CNT impregnated GDL and N,S-CNT-200 impregnated GDL, with no metal oxide catalyst added. Both onset potentials (defined at 10 mA/cm^2), i.e., ORR and OER, for the N,S-CNT-200 electrode are better than those for the N-CNT electrode (Figure 4-3a-b). In addition, the ORR current density obtained at -0.50 V is about 40 mA/cm^2 higher for the N,S-CNTs. The OER current density at 0.9 V for the N,S-CNTs is also significantly better (~60 mA/cm^2 higher). For rate testing, the N-CNT electrode has a potential gap of 1.03 V, while the N,S-CNT-200 electrode has a potential gap of 0.97 V (Figure 4-3c). As with the half-cell and full-cell tests, the maximum power density is slightly better when S is co-doped with N on CNTs and the N,S-CNT-200 electrode has a larger maximum current

density (Figure 4-3d). Overall, the electrochemical performance is improved by co-doping CNTs with S and N versus doping CNTs with N only.

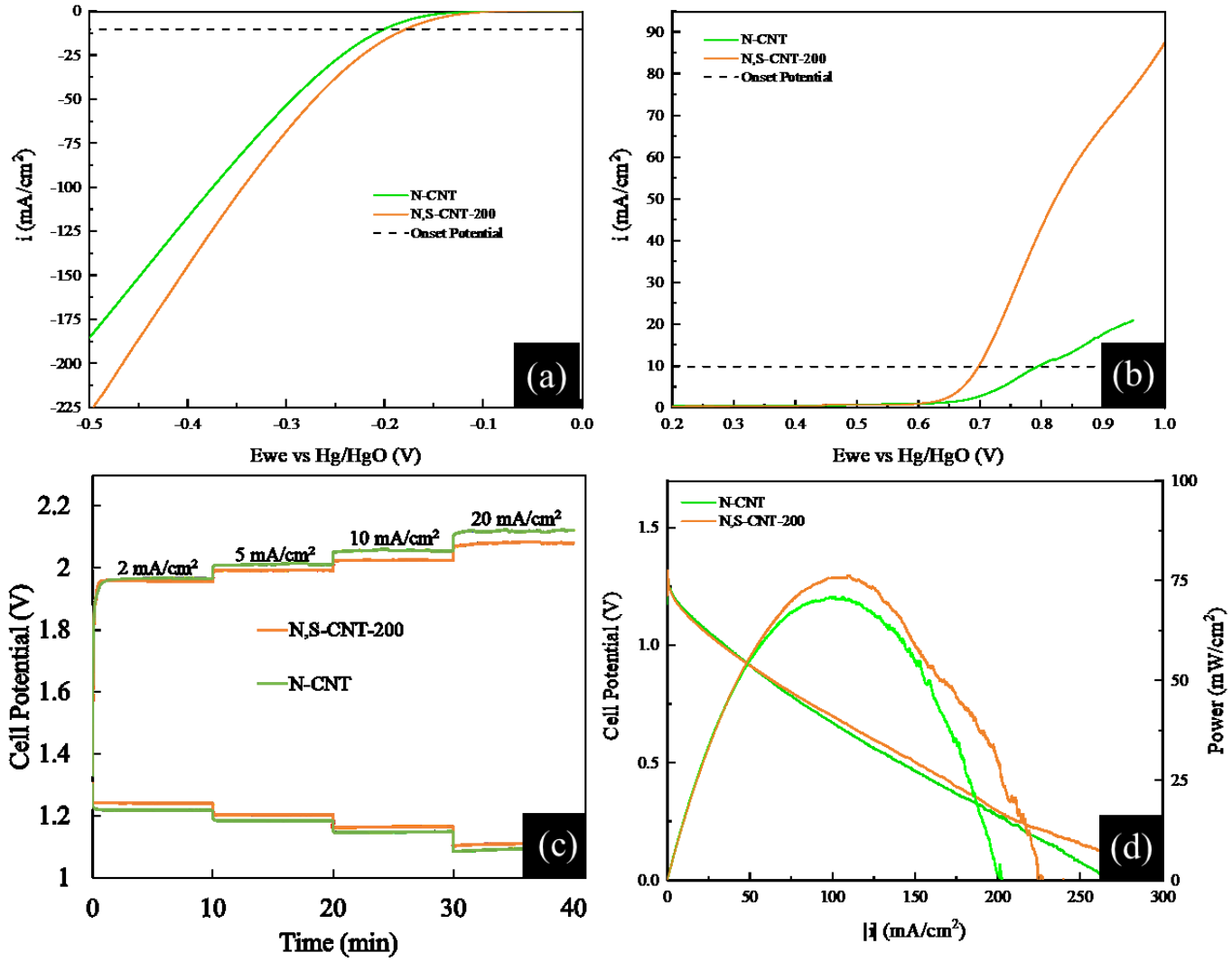

Figure 4-3 Electrochemical testing for N,S-CNTs and N-CNTs. (a) ORR LSV curves, (b) OER LSV curves, (c) full-cell rate testing, and (d) power density.

4.3.2. Electrochemical Results

The metal oxide compositions chosen for anchoring to the N,S-CNTs were NMCO/N,S-CNT-[1:9:4] and ZNMCO/N,S-CNT-[16:1:24:1]. These were chosen based on the best performing tri-metallic oxide (NMCO/N-CNT-[1:9:4]-An) and the best performing tetra-metallic oxide (ZNMCO/N-CNT-[16:1:24:1]-An) in Sections 3.3.1.1 and 3.3.2.1, respectively. Comparison between the oxides on the N,S-CNTs and the N-CNTs is provided throughout this section. Full-cell testing at ± 20 mA/cm^2 was used to evaluate both catalytic performance and electrode performance since the preparation technique has more of an influence on full-cell testing [98]. Half-cell and full-cell electrochemical testing was done on the Ni-Mn-Co and Zn-Ni-Mn-Co oxides anchored onto N,S-CNTs and compared with Pt-Ru/C (Figure 4-4). A current density of ±10 mA/cm^2 was used to determine the onset potentials for ORR and OER during LSV testing. The main parameters are summarized in Table 4-2 and include results from Section 3.3.1.1 and Section 3.3.2.1 for comparison. The NMCO/N,S-CNT-[1:9:4]-An electrode has the best ORR and OER activity for the oxides anchored onto N,S-CNTs with onset potentials comparable to those obtained for the NMCO/N-CNT-[1:9:4]-An electrode. Similarly, the unannealed NMCO/N,S-CNT-[1:9:4] sample has comparable ORR/OER activities to the unannealed NMCO/N-CNT-[1:9:4] electrode. The ZNMCO/N,S-CNT-[16:1:24:1] electrodes are better catalysts in terms ORR/OER activities than Pt-Ru/C and comparable to the tri-metallic oxides on both N,S-CNTs and N-CNTs. The ZNMCO/N,S-CNT-[16:1:24:1]-An electrode has the better ORR/OER activities of the tetra-metallic oxides anchored onto N,S-CNTs. Sulfur has a tendency to bind to active sites, resulting in decreased active sites for the adsorption of reactants [119]. This effect may not be as prominent in the tri-metallic oxides, as sulfur is known to have electrochemical benefits with Co-based catalysts, since there is more Co present [114], [119]. Comparing these electrodes with Pt-Ru/C shows that Pt-Ru/C has the most positive onset ORR potential (-0.064 V vs. Hg/HgO); however, the OER potentials of the NMCO/N,S-CNT-[1:9:4] electrodes are comparable to that of Pt-Ru/C (0.62 V vs Hg/HgO). These results suggest that Pt-Ru/C is still the superior ORR catalyst, while NMCO/N-CNT-[1:9:4]-An and NMCO/N,S-CNT-[1:9:4]-An are comparable as OER catalysts.

Figure 4-4c shows the full-cell test results for the NMCO/N,S-CNT-[1:9:4] and ZNMCO/N,S-CNT-[16:1:24:1] electrodes compared to Pt-Ru/C. Table 4-2 summarizes and

compares the full-cell testing results, at 20 mA/cm^2, of the oxides anchored onto the N-CNTs and N,S-CNTs. Annealing the sample does not have an effect on the OER potential for the tri-metallic oxide; however, when the ZNMCO/N,S-CNT sample was annealed the OER potential increased by 0.05 V. The ORR potential is slightly affected by annealing for both tri-metallic and tetra-metallic oxides anchored onto N,S-CNTs. Previous work (Chapter 3.3.1.1 and 3.3.2.1, respectively) for NMCO/N-CNTs and ZNMCO/N-CNTs showed that annealing improved the ORR performance of electrodes with a high amount of Mn. The addition of S to the N-CNTs dampens the effect that temperature treatment has on the ORR performance; annealing has a more significant impact on the metallic oxide anchored onto the N-CNTs. Conversely, the addition of S with the tetra-metallic oxides and heat treatment negatively impacts the OER performance, whereas for the tri-metallic oxides, and tetra-metallic oxides on N-CNTs has no effect on the OER performance. Comparison of the unannealed samples (Table 4-2) show that anchoring the Ni-Mn-Co oxide onto co-doped N,S-CNTs improved both the ORR and OER potentials, leading to a 3% increase in efficiency. As mentioned before, S combined with Co-based catalysts can have a positive effect on electrochemical performance [119]. The detrimental effect S has with the tetra-metallic oxide is not as apparent with full-cell battery testing, since the method of fabrication has more of an effect. The annealed samples of each composition have the same OER potential and comparable ORR potentials.

Power density curves for the NMCO/N,S-CNT and ZNMCO/N,S-CNT electrodes are shown in Figure 4-4d; maximum power densities are provided in Table 4-2. The NMCO/N,S-CNT-[1:9:4] electrodes and the unannealed ZNMCO/N,S-CNT-[16:1:24:1] electrode have comparable maximum power densities to the NMCO/N-CNT-[1:9:4]-An electrode. However, the NMCO/N,S-CNT-[1:9:4]-An electrode reached its maximum power density at a lower current density. The power curve for the NMCO/N,S-CNT-[1:9:4]-An electrode is noisy at the highest current densities. At high current densities, concentration polarization is more noticeable. Mass transport is limited for the oxygen reactions leading to unstable performance. The best performing catalyst during LSV for ORR activity was the NMCO/N,S-CNT-[1:9:4]-An electrode, which correlates to the electrode with the highest power density. Previous studies suggest that metal oxides with a higher number of metals in the oxide have higher power densities, due to an increase in oxidation states [98]. Additionally, Mn-oxides are known to be good ORR catalysts, so that a higher amount of Mn should give better ORR activity and better

power densities during discharge. This is confirmed by comparing the power density of ZNMCO/N,S-CNT-[16:1:24:1] with NMCO/N,S-CNT-[1:9:4]; however, annealing has a negative impact on the power density for the ZNMCO/N,S-CNT-[16:1:24:1] electrode. The metallic oxides anchored onto N,S-CNTs do not exceed the maximum power density of Pt-Ru/C (120 mW/cm^2). These results show that annealing the ZNMCO/N,S-CNT electrodes with Zn-Ni-Mn-Co oxide with N,S-CNTs decreases the maximum power density achievable. The poor performance of the ZNMCO/N,S-CNT-[16:1:24:1] electrodes is likely due to the low amount of Co in the sample, since S and Co have a synergistic effect. Wang [120] found that annealing promoted crystallization of ZnS:Mn thin films. This could explain why annealing the ZNMCO/N,S-CNT-[16:1:24:1] electrode has more of a negative effect on the full-cell rate tests and maximum power density. Further analysis will be provided in Section 4.3.3.2.

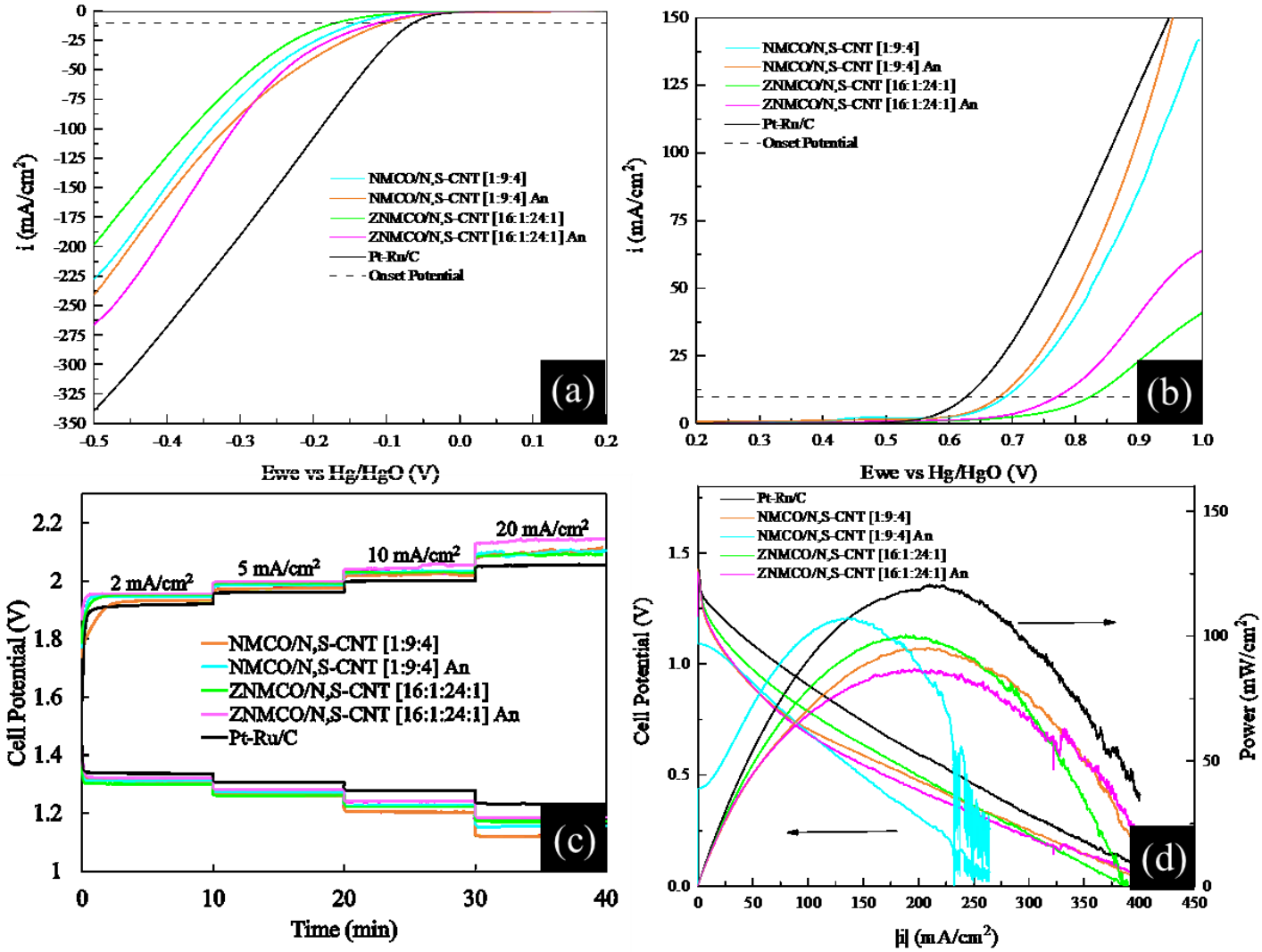

Figure 4-4 Electrochemical results for tri-metallic and tetra-metallic catalysts. a) ORR LSV measurements, b) OER LSV measurements, c) battery rate tests, d) power curves power curves. Some electrodes have been annealed while others are in the as fabricated condition.

Table 4-2 Summary of electrochemical performance data

Sample	Onset ORR Potential [V, @ -10 mA/cm^2]	Onset OER Potential [V, @ 10 mA/cm^2]	ORR Potential [V, @ 10mA/cm^2]	OER Potential [V, @ 20mA/cm^2]	Efficiency [%, @ 20mA/cm^2]	Maximum Power Density [mW/cm^2]
NMCO/N-CNT [1:9:4]	-0.131	0.67	1.08	2.13	50.7%	N/A
NMCO/N-CNT [1:9:4] An	-0.095	0.65	1.19	2.09	56.9%	97
NMCO/N,S-CNT [1:9:4]	-0.137	0.70	1.12	2.09	53.6%	95
NMCO/N,S-CNT [1:9:4]-An	-0.096	0.68	1.16	2.09	55.5%	107
ZNMCO/N-CNT [16:1:24:1]	-0.160	0.79	1.10	2.02	54.5%	N/A
ZNMCO/N-CNT [16:1:24:1]-An	-0.108	0.80	1.15	2.02	56.9%	125
ZNMCO/N,S-CNT [16:1:24:1]	-0.165	0.82	1.17	2.09	56.0%	100
ZNMCO/N,S-CNT [16:1:24:1]-An	-0.109	0.77	1.19	2.14	55.6%	85

Bifunctional cycling tests were conducted on the unannealed samples of the NMCO/N,S-CNT-[1:9:4] and ZNMCO/N,S-CNT-[16:1:24:1] electrodes, and compared with previous N-CNT electrodes and Pt-Ru/C (Figure 4-5). The unannealed samples were chosen since the full-cell testing indicated that there was not a significant difference between unannealed and annealed electrodes. As such, eliminating the annealing step simplified the overall electrode preparation process. The first ten or so cycles during bifunctional cycling are conditioning cycles, which is the amount of time needed to completely wet the GDL. A summary of the initial and final efficiencies is shown in Table 4-3.The ORR and OER potential for both electrodes are very stable. The differences between the initial cycle (cycle 11) and the final cycle for the

NMCO/N,S-CNT-[1:9:4] and ZNMCO/N,S-CNT-[16:1:24:1] electrodes are 1.5%, and 2.3%, respectively. Both NMCO/N,S-CNT-[1:9:4] and ZNMCO/N,S-CNT-[16:1:24:1] electrodes outperform the NMCO/N-CNT-[1:9:4]-An electrode (Section 3.3.1.1). The final efficiencies of the NMCO/N,S-CNT-[1:9:4], and ZNMCO/N,S-CNT-[16:1:24:1] electrodes are comparable to the final efficiency of the ZNMCO/N-CNT-[16:1:24:1]-An electrode (Section 3.3.2.1).

Table 4-3 Bifunctional cycling efficiency summary

Sample	Initial Efficiency (%, 11th cycle)	Final Efficiency (%)
NMCO/N-CNT-[1:9:4]-An	52.0	52.3
NMCO/N,S-CNT-[1:9:4]	53.6	55.1
ZNMCO/N-CNT-[16:1:24:1]-An	53.5	56.0
ZNMCO/N,S-CNT-[16:1:24:1]	52.1	54.4

The tri-metallic oxides had a relatively stable ORR potential at 1.13 V for 200 cycles at 10 mA/cm^2. The NMCO/N,S-CNT-[1:9:4] electrode had a reduction in the OER potential from 2.09 V to 2.05 V, whereas the NMCO/N-CNT-[1:9:4]-An electrode remained constant at 2.17 V. As with the tri-metallic oxides, the tetra-metallic oxides had stable ORR potentials as well, with values between 1.12 V and 1.15 V. There was significant improvement in the OER potential for both electrodes. ZNMCO/N-CNT-[16:1:24:1]-An had a final OER potential of 2.05 V while ZNMCO/N,S-CNT-[16:1:24:1] had a final OER potential of 2.08 V. At around the 100th cycle and the 150th cycle, there is a temporary decrease in electrode performance. This temporary degradation in performance is due to bubble formation and electrolyte evaporation. Once the bubbles were removed and electrolyte refilled, the performance completely recovered. The four transition metal oxide catalyst electrodes outperformed the Pt-Ru/C catalyst in bifunctional cycling stability and electrochemical potential. The NMCO/N,S-CNT-[1:9:4] electrode outperformed the NMCO/N-CNT-[1:9:4]-An electrode, while the ZNMCO/N,S-CNT-[16:1:24:1] electrode was comparable with the ZNMCO/N-CNT-[16:1:24:1]-An electrode.

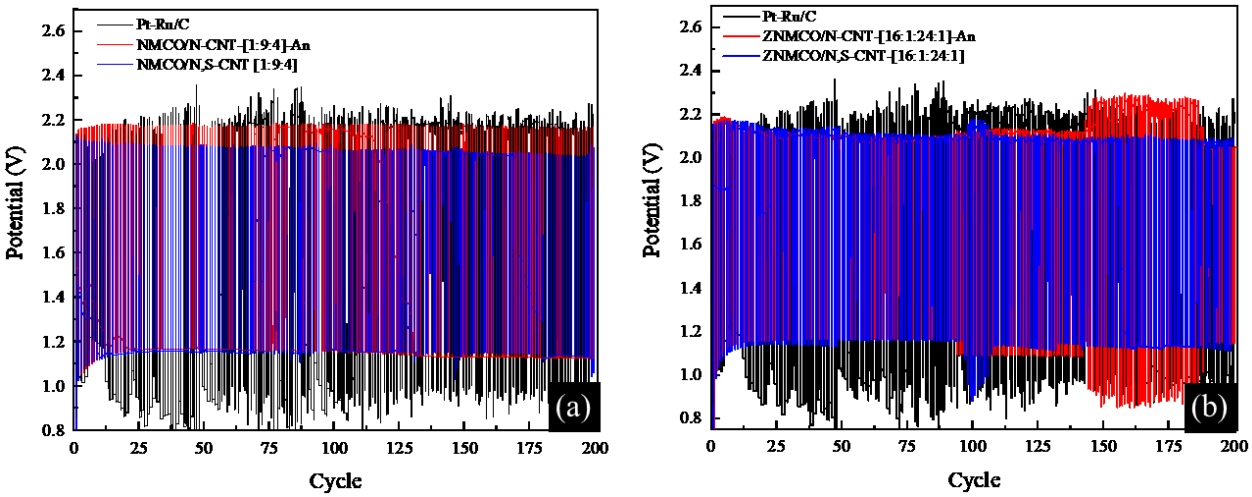

Figure 4-5 Bifunctional cycling of (a) NMCO/N-CNT-[1:9:4]-An, NMCO/N,S-CNT-[1:9:4], and Pt-Ru/C samples, and (b) ZNMCO/N-CNT-[16:1:24:1]-An, ZNMCO/N,S-CNT-[16:1:24:1], and Pt-Ru/C samples, using a homemade Zn-air battery at 10 mA/cm^2 for 200 cycles (30 min per cycle) in 6 M KOH + 0.25 M ZnO.

The electrochemical results indicate that sulfur improves the electrochemical results when paired with high Co content catalysts, as evident from the NMCO/N,S-CNT-[1:9:4] unannealed sample during both full-cell rate testing and bifunctional cycling testing. For the low Co sample, i.e., the ZNMCO-[16:1:24:1] electrode, co-doping of CNTs with S and N lowered the overall bifunctional cycling efficiency.

4.3.3. Microstructural Characterization

4.3.3.1. Tri-metallic oxides on N,S-CNTs

SEM and EDX analysis were done on the NMCO/N,S-CNT-[1:9:4] electrode (Figure 4-6a, & d). For comparison, SEM and EDX analysis of the NMCO/N-CNT-[1:9:4]-An electrode is shown in Figure 4-6b-c. The unannealed NMCO/N,S-CNT-[1:9:4] electrode was further investigated and compared to the NMCO/N-CNT-[1:9:4]-An electrode, since the electrochemical results for the NMCO/N,S-CNT-[1:9:4] electrodes were similar and the unannealed electrode simplifies the process. The SEM images (Figure 4-6a-b) show the nanoparticles (yellow arrows) on the N-CNTs (blue arrows) and N,S-CNTs (red arrows), as well as the clusters of nanoparticles on the GDL (green arrows). The EDX spectra have strong metal peaks for Ni, Mn, and Co (Figure 4-6c-d). The Ni peaks are less intense for the tri-metallic oxide on the N,S-CNTs. This will be further discussed in the next paragraph. The C peak is from the GDL and the N,S-CNTs and N-CNTs, while the oxygen peak is from the metal oxides. The strong fluorine peak is present from the PTFE on the GDL and the Nafion used during synthesis. Sodium is present from the NaOH used during fabrication and the S peak in both spectra is from the $NiO_4S{\cdot}7(H_2O)$ utilized during synthesis. The S doped onto the N-CNTs is likely not detectable by the EDX detector. The S content, determined by EDX analysis, is ~0.3 at% in both the N-CNTs and N,S-CNTs.

As mentioned in the previous paragraph, the Ni peaks are less intense for the NMCO/N,S-CNT-[1:9:4] sample compared with the NMCO/N-CNT-[1:9:4] sample, which implies that there is a smaller amount of Ni in the former. However, as discussed in Chapter 3, there are two sources of Ni; i.e., Ni utilized as a catalyst during CNT synthesis and Ni in the metal salts used to produce the metal oxide. This could lead to variable amounts of Ni detected in the samples. If the Mn:Co ratios for the two samples are compared, the values are quite similar, i.e., in the 2.1-2.2 range. The average relative amounts of Ni, Mn, and Co in the N,S-CNT electrode are 8.5 at%, 63.4 at%, and 28.2 at%, respectively. There is not a significant difference between the relative amounts of the metals when compared with the N-CNT electrode; i.e., 6.6 at%, 62.9 at%, and 30.2 at% for Ni, Mn, and Co, respectively.

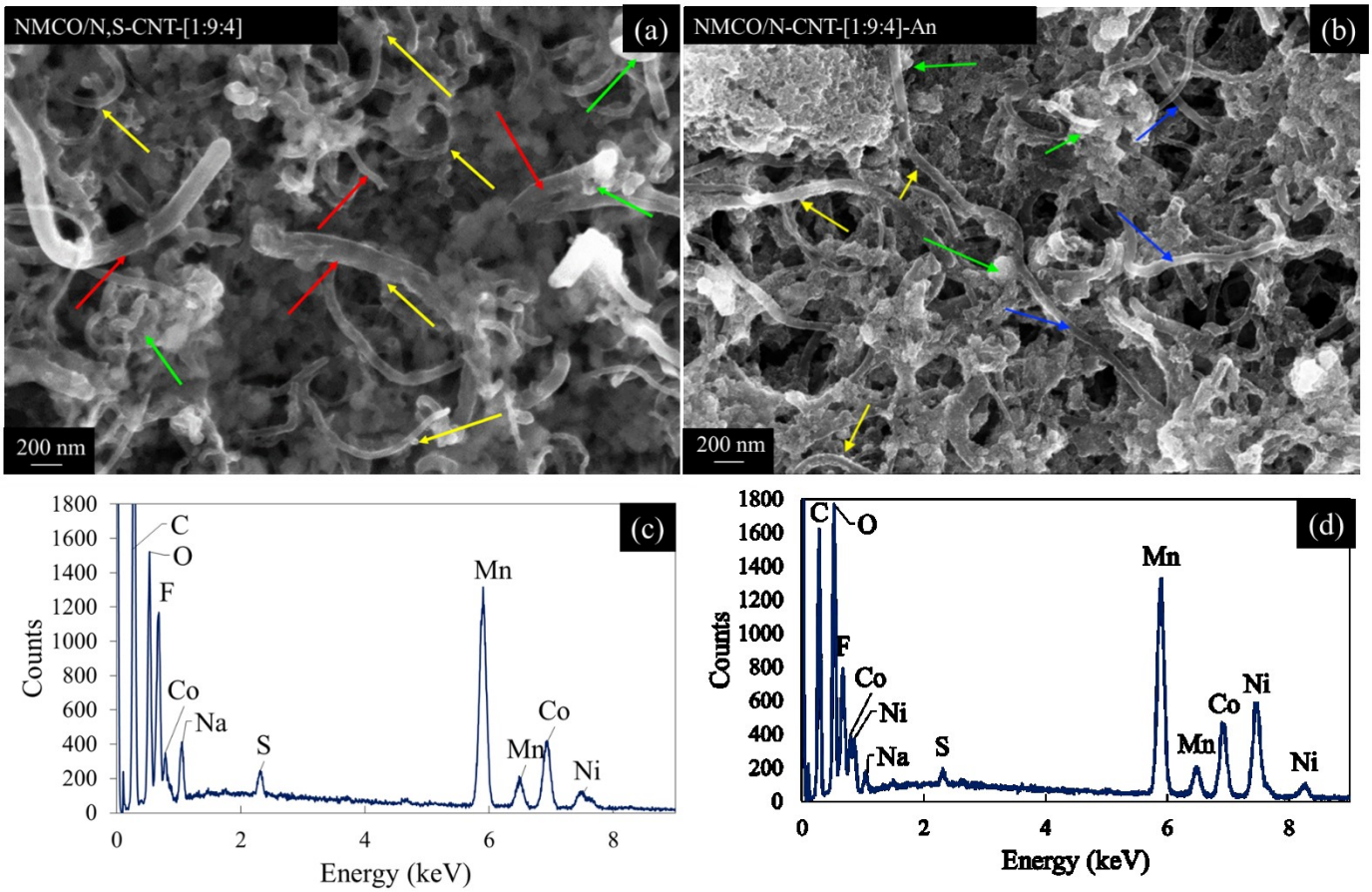

Figure 4-6 SEM and EDX analysis. (a) SE image of NMCO/N,S-CNT-[1:9:4], (b) SE image of NMCO/N-CNT-[1:9:4]-An, (c) EDX spectrum from NMCO/N,S-CNT-[1:9:4], and (d) EDX spectrum from NMCO/N-[1:9:4]-An. Blue arrows indicate N-CNTs, red arrows indicate N,S-CNTs, green arrows indicate clusters of precipitates on the GDL surface, and yellow arrows indicate nanoparticles decorated on the CNTs.

TEM/STEM analysis was conducted to further investigate the microstructure of the NMCO/N,S-CNT-[1:9:4] sample (Figure 4-7 and Figure 4-8). The STEM high angle annular dark field (HAADF) image of the NMCO/N,S-CNT-[1:9:4] electrode shows the defect bamboo structure of the N,S-CNTs as well as the metal oxide nanoparticles anchored onto the N,S-CNTs and clusters of metal oxide nanoparticles, confirming the SEM observations (Figure 4-7a and Figure 4-8a). The lattice fringes in the high resolution TEM (HRTEM) image (Figure 4-7b) indicate that the metal oxide nanoparticles are crystalline. EDX elemental maps for Ni, Mn, and Co are shown in (Figure 4-7d-g, and Figure 4-8b-d). Similar to the NMCO/N-CNT electrode, the clusters of nanoparticles contain all three metals (Figure 3-6). Nickel is present over the entire

N,S-CNT, which is an outcome of Ni being used as a catalyst in the CNT synthesis process and has been observed previously in Chapter 3.0 [95]. The Mn and Co EDX maps overlap and correlate with the nanoparticles decorating the N,S-CNTs (Figure 4-7); however, Ni appears to be absent. As an example, semi-quantitative EDX analysis of the region shown in Figure 4-7c indicates that the particles contain about 74 at% Mn and 26 at% Co, with no Ni. Nanoparticle clusters, not associated with CNTs, do contain Ni; e.g., the region shown in Figure 4-8a contains about 20 at% Ni, 57 at% Mn, and 23 at% Co. The amounts are very similar to those for the same metal composition anchored onto N-CNTs (Section 3.3.1.2). Since Ni is present over the entire N,S-CNT, comparing the Mn:Co ratio enables for better comparison between SEM and (S)TEM results. From the (S)TEM results, the Mn:Co ratio for the oxides particles is ~2.5:1, while the SEM results give a Mn:Co ratio of 2.1:1. The differences in composition between the two analyses is due to the different sample volumes. SEM EDX analysis was done over a much larger area of the GDL surface, while STEM EDX was much more localized.

Selected area diffraction (SAD) patterns were obtained from the oxide nanoparticle clusters; an example for the region indicated in Figure 4-8a, is shown in Figure 4-8e. The diffuse ring with a d-spacing ~0.325 nm is from the CNTs (carbon), while the spotty, discontinuous rings are from the oxide particles. The SAD pattern was indexed to a Mn-Co spinel oxide structure (same structure as PDF #23-1237, with a nominal composition of $MnCo_2O_4$ and a = 8.269 nm). SEM EDX analysis gives a Mn:(Co+Ni) ratio of about 1.8:1, while STEM analysis gives a Mn:(Co+Ni) ratio of about 1.9:1. As mentioned above the difference between the two analyses is due to the different sample volumes. However, the ratios are not significantly different (approximate 2:1) and correspond to a spinel phase with a composition of $(Ni,Co)Mn_2O_4$. This predicted phase for the NMCO/N,S-CNT-[1:9:4] electrode is the same as for the NMCO/N-CNT-[1:9:4]-An electrode (Figure 3-8). The metal valences and corresponding phases will be further discussed along with the XPS analysis.

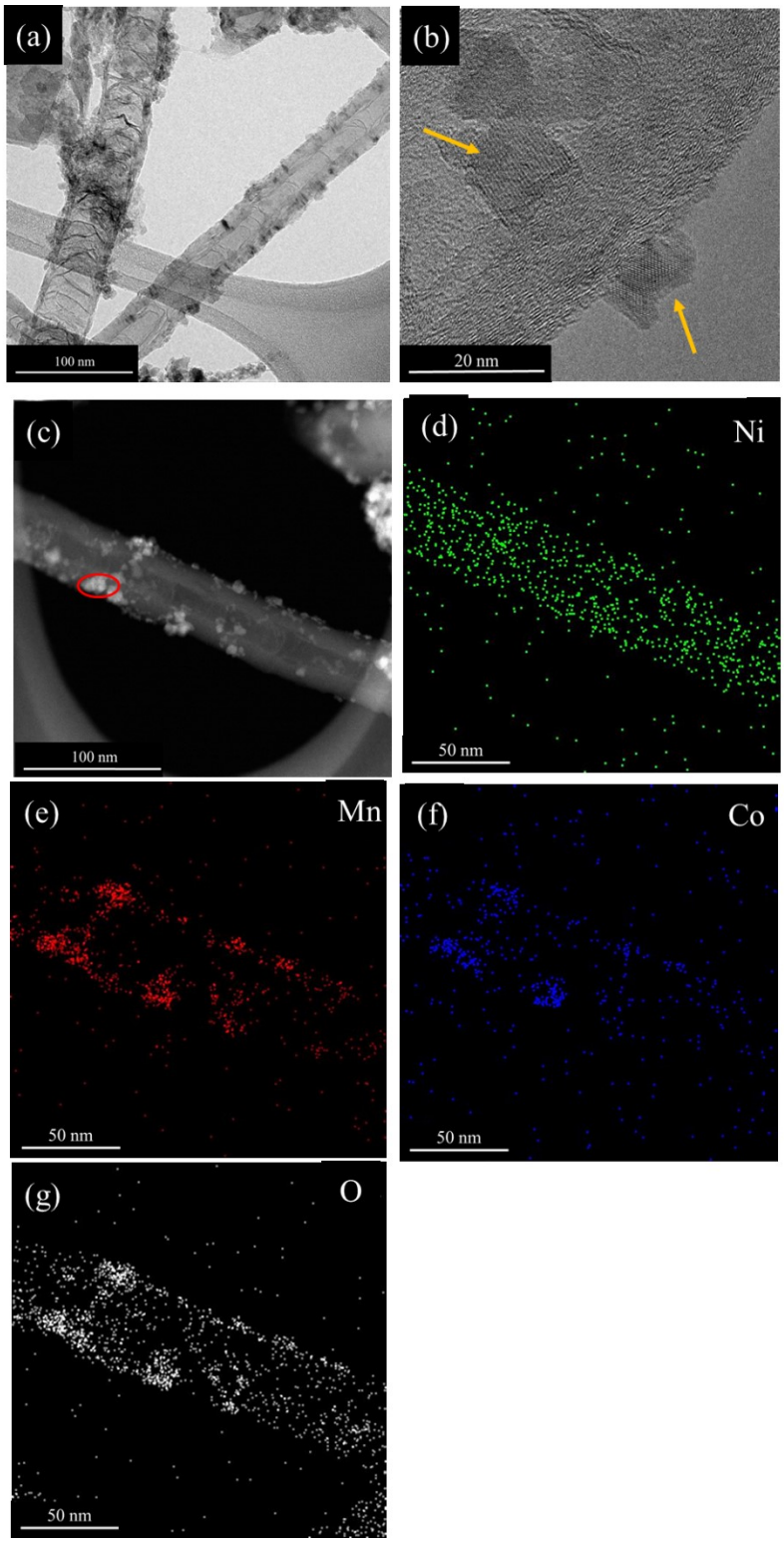

Figure 4-7 TEM/STEM analysis of NMCO/N,S-CNT-[1:9:4]. (a) TEM BF image, (b) HRTEM image, (c) STEM ADF image, (d)-(g) EDX elemental maps for Ni, Mn, Co. and O. Orange arrows in (b) outline nanoparticles on N,S-CNTs.

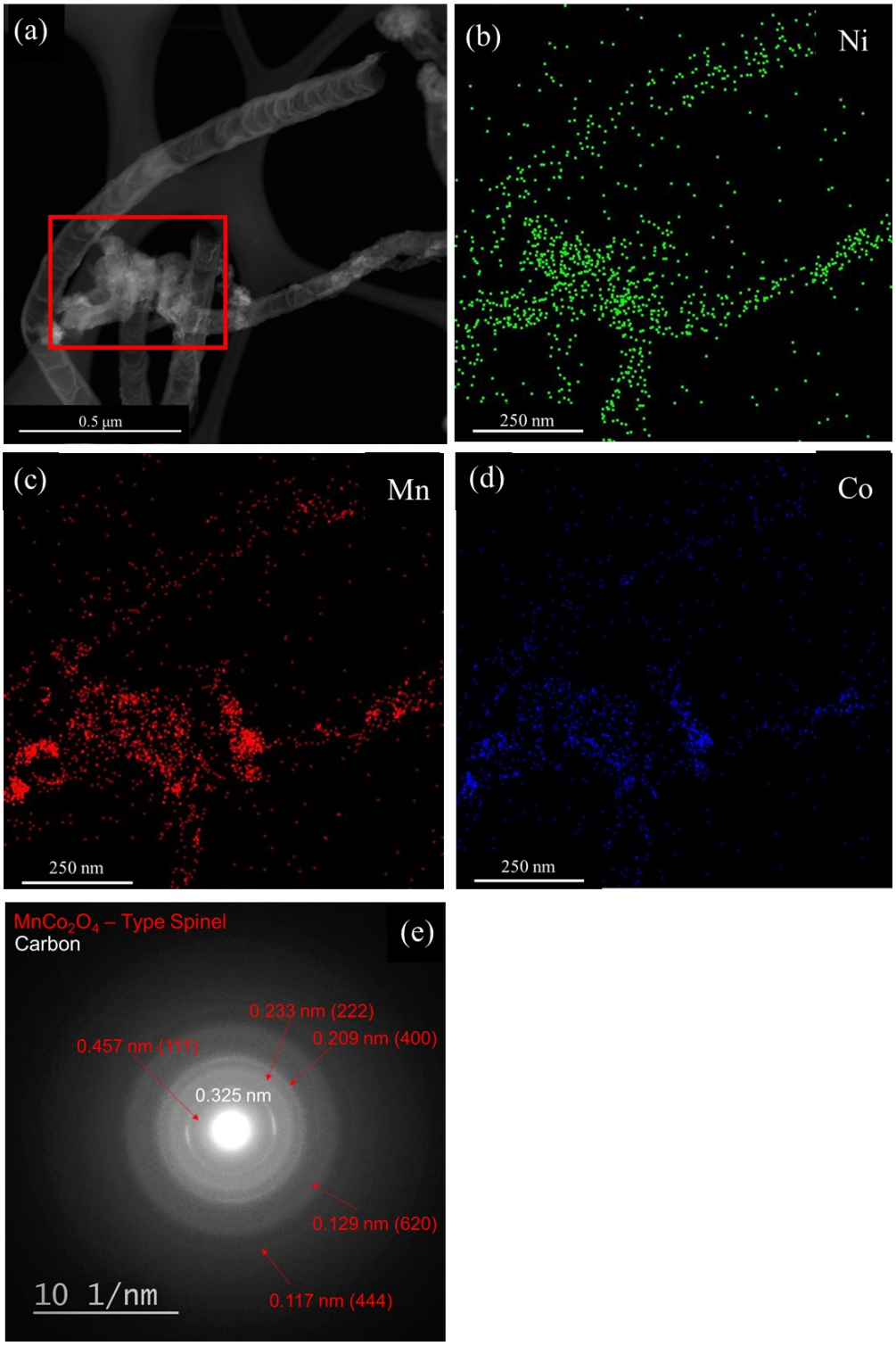

Figure 4-8 TEM/STEM analysis of NMCO/N,S-CNT-[1:9:4]. (a) STEM ADF image, (b)-(d) EDX elemental maps for Ni, Mn, Co. and O, and (e) SAD pattern from the red box in (a).

To confirm the electron microscopy phase analysis for the NMCO/N,S-CNT-[1:9:4] electrode, XPS analysis was done (Figure 4-9). Figure 4-9a shows the survey spectrum with peaks corresponding to Ni, Co, F, Mn, O, and C. The strong fluorine peak is present due to the PTFE in the GDL as well as from the Nafion used during electrode synthesis. Carbon is present from the GDL and the N,S-CNTs, while oxygen is due to the metal oxide particles. Figure 4-9b-d show the high-resolution $2p_{3/2}$ spectra for Ni, Mn, and Co. The deconvolution of the high-resolution $2p_{3/2}$ spectra, as well as the O 1s and Mn 3s high-resolution spectra, are shown in Figure 4-9e-i. The O 1s spectrum can be fit to three peaks at ~529 eV, ~531 eV, and ~534 eV (Figure 4-9i). These peaks correspond to lattice oxygen (M-O-M bonds), hydroxides (M-O-H and H-O-H bonds), and carbon-oxygen bonds [102]. The O 1s peak consists of mainly the hydroxide and lattice oxygen bonds. The O 1s peaks for the NMCO/N,S-CNT electrode are consistent with the results obtained for the NMCO/N-CNT electrode. The NMCO/N-CNT electrode had a Na KLL Auger peak at ~335 eV, whereas the NMCO/N,S-CNT electrode does not.

The Ni $2p_{3/2}$ peak is weak and has significant overlap from the F Auger peak (861 eV); thus the accuracy of the Ni analysis is low. Similar overlap from the F Auger peak was seen when analyzing the NMCO/N-CNT electrode spectrum in Chapter 3 Section 3.3.1.2. The peaks at around 854 eV – 856 eV can be attributed to Ni 3+, while the peaks at ~853 eV and ~860 eV are due to the presence of Ni 2+ (Figure 4-9e) [97]. Note that the F KLL Auger peak at 861 eV contributes to about 80 at% of the Ni $2p_{3/2}$ spectrum. The average valence for Ni is 2.1 (Table 4-4). The Ni valence obtained for the NMCO/N-CNT electrode (Chapter 3) was the same.

The Co $2p_{3/2}$ high-resolution spectrum (Figure 4-9h) can be fit to both Co 2+ and Co 3+, giving an average Co valence of 2.6 (Table 4-4) [95], [97]. It appears that the addition of sulfur to the N-CNTs increases the amount of Co 3+ present in the sample. The increase in valence was expected. Previous studies have reported an increased Co oxidation state when combined with S, likely due to crystal lattice defects induced by S-doping [114], [121]. This is further confirmed by comparing the results here with the XPS results for the NMCO/N-CNT electrode, which had a 2+ valence for Co with little to no Co 3+ contribution (Figure 4-10 and Section 3.3.1.2).

The deconvolution of the Mn $2p_{3/2}$ high-resolution (Figure 4-9f) peak leads to Mn 3+ and Mn 4+ valences, giving an average valence of 3.5 (Table 4-4). Additionally, the Mn 3s peak was used to confirm the Mn valence (Figure 4-9g). The valence is determined by measuring the peak

splitting. Figure 4-9g shows the peak differences for each valence [95], [97], [101], [102]. The energy difference between the two peaks is 5.3 eV, which corresponds to a valence of 3.0 (Table 4-4). Based on the two methods for valence determination, the Mn valence appears to be close to 3+, with perhaps some contribution from 4+. The analysis of the NMCO/N,S-CNT Mn $2p_{3/2}$ and Mn 3s peaks align with the previous XPS analysis for the NMCO/N-CNT Mn $2p_{3/2}$ and Mn 3s peaks in Section 3.3.1.2.

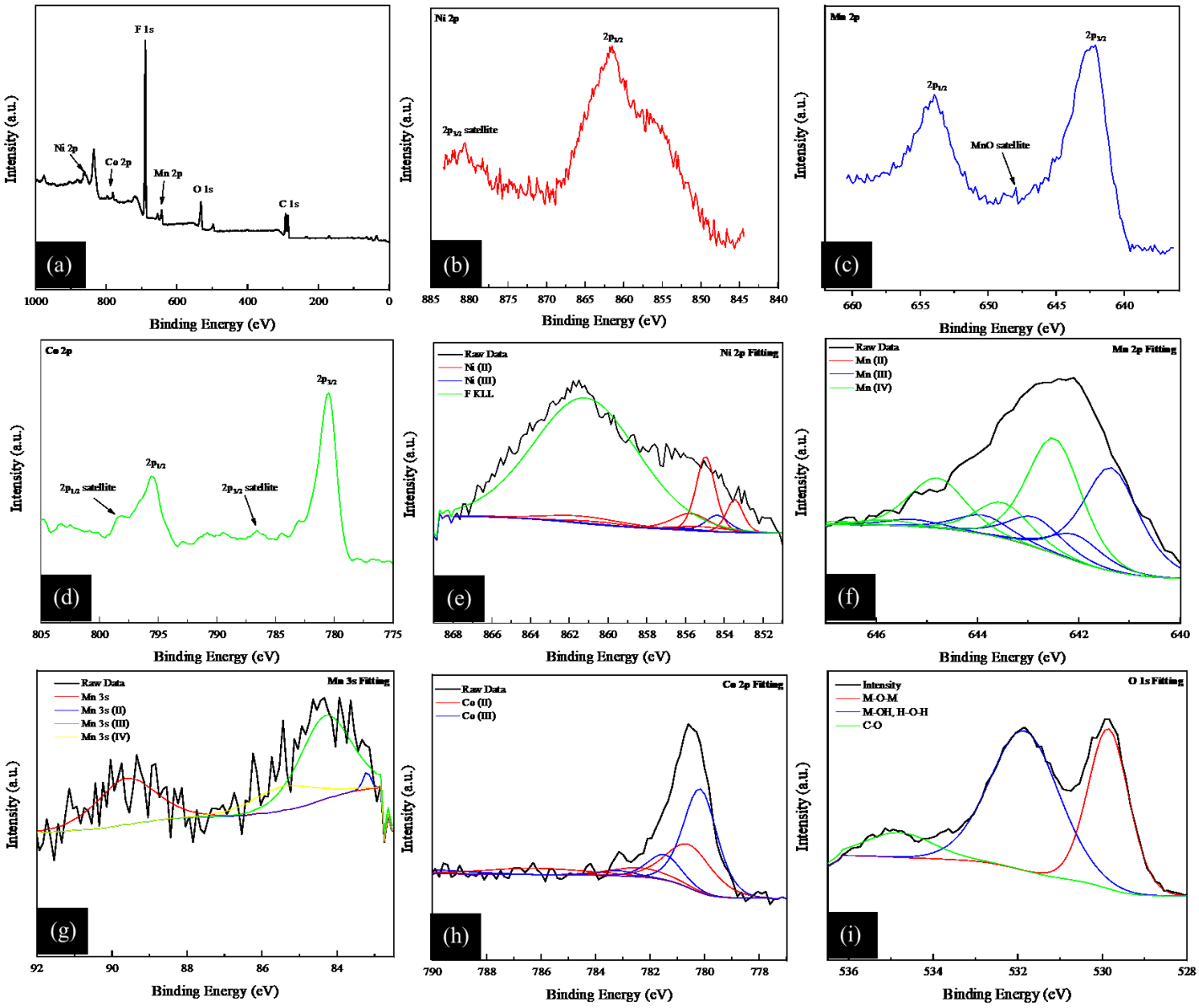

Figure 4-9 XPS spectra and fittings for NMCO/N,S-CNT-[1:9:4]. (a) Survey spectrum, (b) Ni 2p, (c) Ni $2p_{3/2}$, (d) Mn 2p, (e) Mn $2p_{3/2}$, (f) Mn 3s, (g) Co 2p, (h) Co $2p_{3/2}$, and (i) O 1s peaks high-resolution spectra.

Table 4-4 XPS analysis of high-resolution spectra with average valences calculated based on the at% of each valence

Sample	Ni 2p 3/2			Co 2p 3/2			Mn 2p 3/2				Mn 3s	
	2+ (%)	3+ (%)	Average Valence	2+ (%)	3+ (%)	Average Valence	2+ (%)	3+ (%)	4+ (%)	Average Valence	Peak Splitting (eV)	Average Valence
NMCO/N,S-CNT-[1:9:4]	85.8	14.2	**2.1**	40.3	59.7	**2.6**	0.0	47.7	52.3	**3.5**	5.3	**3.0**

The SEM, TEM/STEM, and XPS results can be combined for phase identification of metal oxide in the NMCO/N,S-CNT-[1:9:4] electrode. Electron diffraction patterns were indexed to a cubic, spinel phase, i.e., AB_2O_4 with A corresponding to metal ions with a valence of 2+ (tetrahedral sites) and B corresponding to metal ions with a valence of 3+ (octahedral sites). Overall EDX analysis in the SEM gave a Mn:(Co+Ni) ratio of 1.75:1. Higher ratios (2.4:1) were obtained through EDX analysis in the STEM, but analysis in the STEM is more localized and may not be as representative. The XPS results showed that Ni has an average valence of ~2+, a split valence of 2+ and 3+ for Co, and a valence of ~3+ for Mn. The proposed chemical formula for the spinel phase is then $(Ni,Co)(Mn,Co)_2O_4$. This is similar to the chemical formula for the NMCO/N-CNT-[1:9:4]-An electrode, i.e., $(Ni,Co)Mn_2O_4$. Comparison of the two electrodes indicates that S enables a higher oxidation state for Co, likely due to lattice defects induced from S-doping (Figure 4-10).

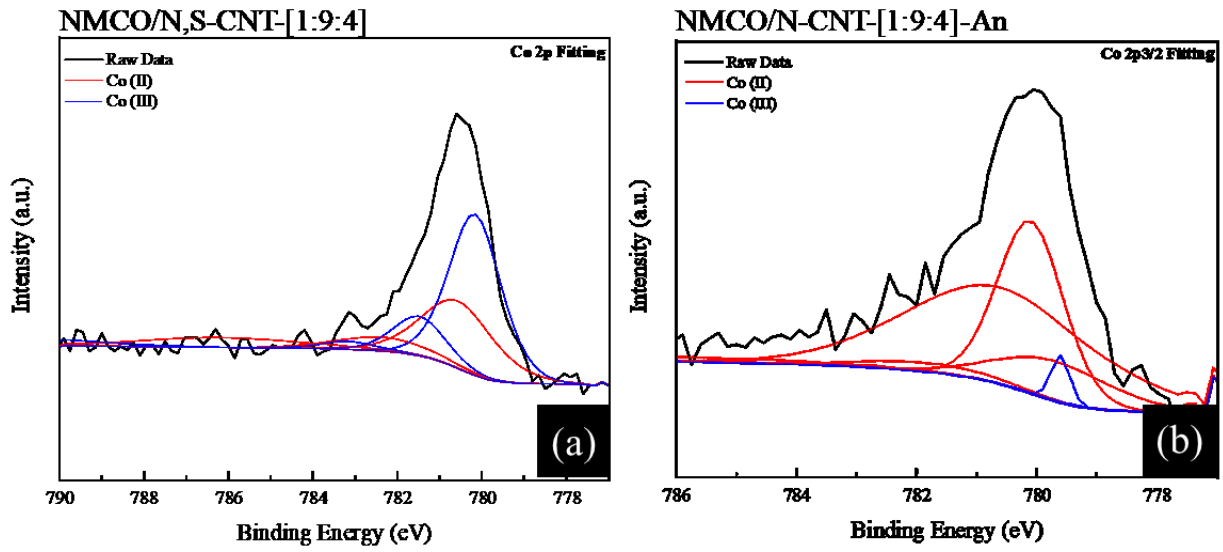

Figure 4-10 XPS Co $2p_{3/2}$ fitting for (a) NMCO/N,S-CNT-[1:9:4], and (b) NMCO/N-CNT-[1:9:4]-An.

4.3.3.2. Tetra-metallic oxides on N,S-CNTs

The unannealed ZNMCO/N,S-CNT-[16:1:24:1] electrode was further investigated due to better electrochemical performance over the annealed electrode. SEM analysis was done on the ZNMCO/N,S-CNT-[16:1:24:1] and ZNMCO/N-CNT-[16:1:24:1]-An electrodes (Figure 4-11). The SE image of the samples (Figure 4-11a-b) shows the N-CNTs (blue arrows) and N,S-CNTs (red arrows), with metal oxide nanoparticles anchored onto the CNTs (yellow arrows) as well as the nanoparticle clusters within the GDL (green arrows). The EDX spectra, shown in Figure 4-11c-d, have strong peaks for Zn and Mn, with weaker peaks for Co and Ni. The Co and Ni peaks are weak as the amount of metal salt added during synthesis is significantly less than that for the Zn and Mn salts. As explained previously, the F peak is from the PTFE in the GDL and from the Nafion used during synthesis. The carbon peak is from the CNTs and the GDL and the oxygen peak is present in the metallic oxides. The Na and S peaks are due to the NaOH and $NiO_4S{\cdot}7(H_2O)$ used during synthesis; however, it is likely that some of the sulfur detected is from the N,S-CNTs. There is no observable difference in microstructure between the tetra-metallic oxide on the N-CNTs and on the N,S-CNTs. Further EDX analysis gives an average relative metal content of Zn, Ni, Mn, and Co in the metal oxide on the N,S-CNTs of 32.6 at% Zn, 3.5 Ni at%, 43.6 Mn at%, and 2.3 Co at%. Comparing these results to the tetra-metallic oxide on N-CNTs (Section 3.3.2.2), there is not a significant difference with 39.1 at% Zn, 2.9 at% Ni,

55.1 at% Mn, and 2.9 at% Co. This is further confirmed by comparing the two Mn:Zn atomic ratios. The metallic oxide on the N,S-CNTs has an average ratio of 1.3:1 while the metallic oxide on the N-CNTs has a ratio of 1.4:1.

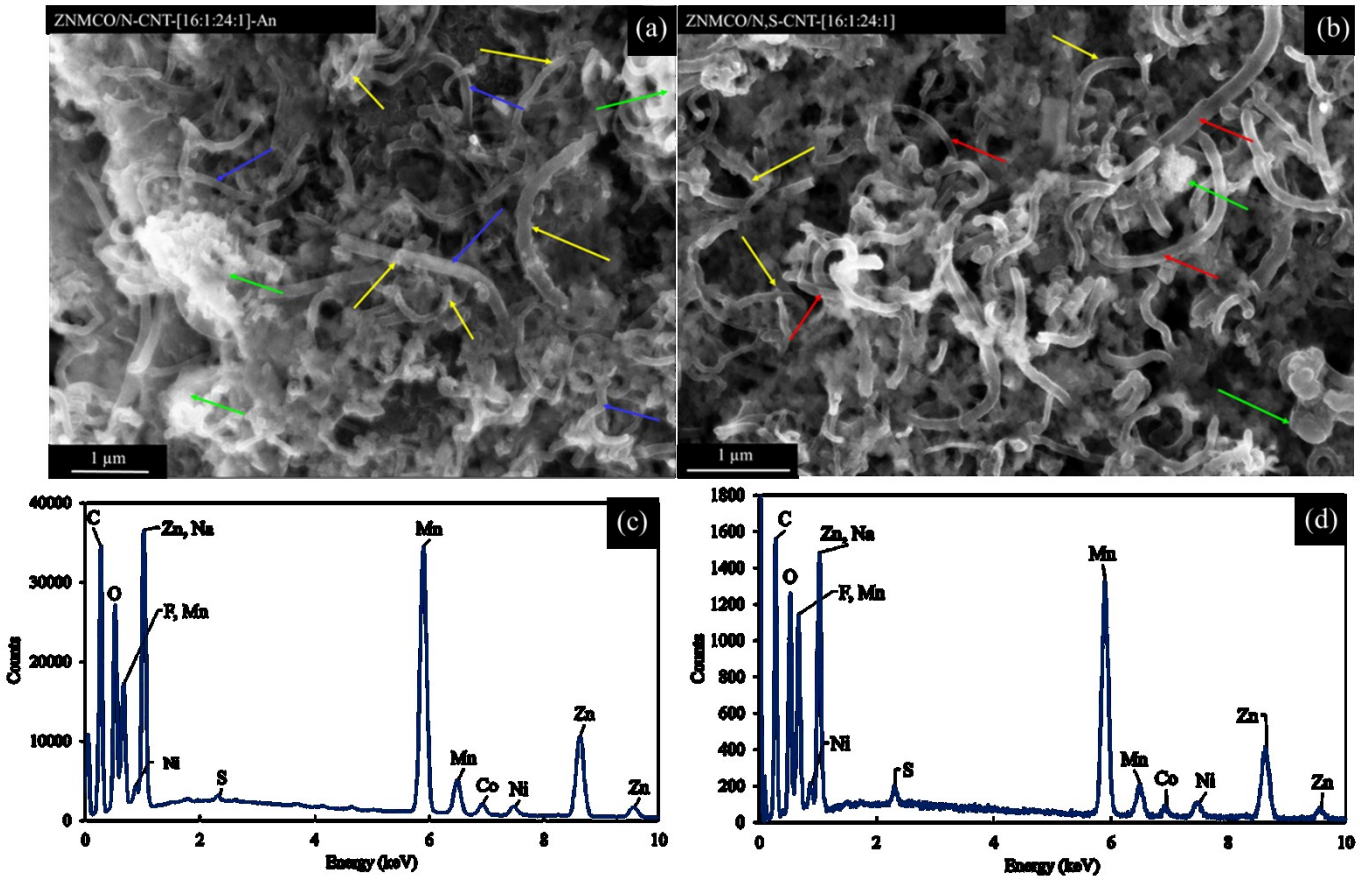

Figure 4-11 SEM and EDX analysis. (a) SE image of ZNMCO/N-CNT-[16:1:24:1]-An, (b) SE image of ZNMCO/N,S-CNT-[16:1:24:1], (c) EDX spectrum of ZNMCO/N-CNT-[16:1:24:1]-An, and (d) EDX spectrum of ZNMCO/N,S-CNT-[16:1:24:1]. Blue arrows indicate N-CNTs, red arrows indicate N,S-CNTs, green arrows indicate clusters of precipitates on the GDL surface, and yellow arrows indicate nanoparticles decorated on the CNTs.

TEMSTEM analysis was done on the ZNMCO/N,S-CNT-[16:1:24:1] electrode (Figure 4-12). The TEM BF, HRTEM, and STEM ADF images (Figure 4-12a-c) show the metallic oxide nanoparticles anchored to the N,S-CNTs as well as present as oxide clusters. The nanocrystalline structure of the nanoparticles anchored onto the N,S-CNTs can be seen in Figure 4-12b (orange arrows). Zn, Mn, Co, and O EDX maps (Figure 4-12d,f-h) overlap with one another and correlate

with the anchored nanoparticles on the N,S-CNTs. The EDX map for Ni (Figure 4-12e) shows it is present over the entire N,S-CNT with little or no Ni in the oxide particles anchored to the CNTs. This result has been observed for the other samples. The average composition of the anchored oxide nanoparticles is 53 at% Mn, 45 at% Zn, and 3 at% Co, while the oxide clusters have a similar composition but contain some Ni (55 at% Mn, 42 at% Zn, 3 at% Co, and 1 at% Ni). For comparison, EDX analysis was performed on the ZNMCO/N-CNT-[16:1:24:1]-An electrode (Section 3.3.2.2). Similar compositions to the ZNMCO/N,S-CNT-[16:1:24:1] electrode were obtained, with no Ni detected in the nanoparticles anchored to the CNTs and a small amount of Ni (<1 at% Ni) for the nanoparticle clusters (Figure 4-13). The SAD pattern for ZNMCO/N,S-CNT-[16:1:24:1] (Figure 4-12i) was indexed to hetaerolite, a tetragonal spinel structure (PDF#24-1133, with a nominal composition of $ZnMn_2O_4$, a = 0.572 nm and c = 0.925 nm) [104], [105]. The overall Mn:Zn atomic ratio is ~1.3:1, which is comparable to the overall Mn:Zn ratio for the ZNMCO/N-CNT-[16:1:24:1]-An electrode (~1.4:1). A Mn:Zn ratio less than 2 indicates that a complex spinel structure may have formed [106]. This will be further discussed with the XPS analysis.

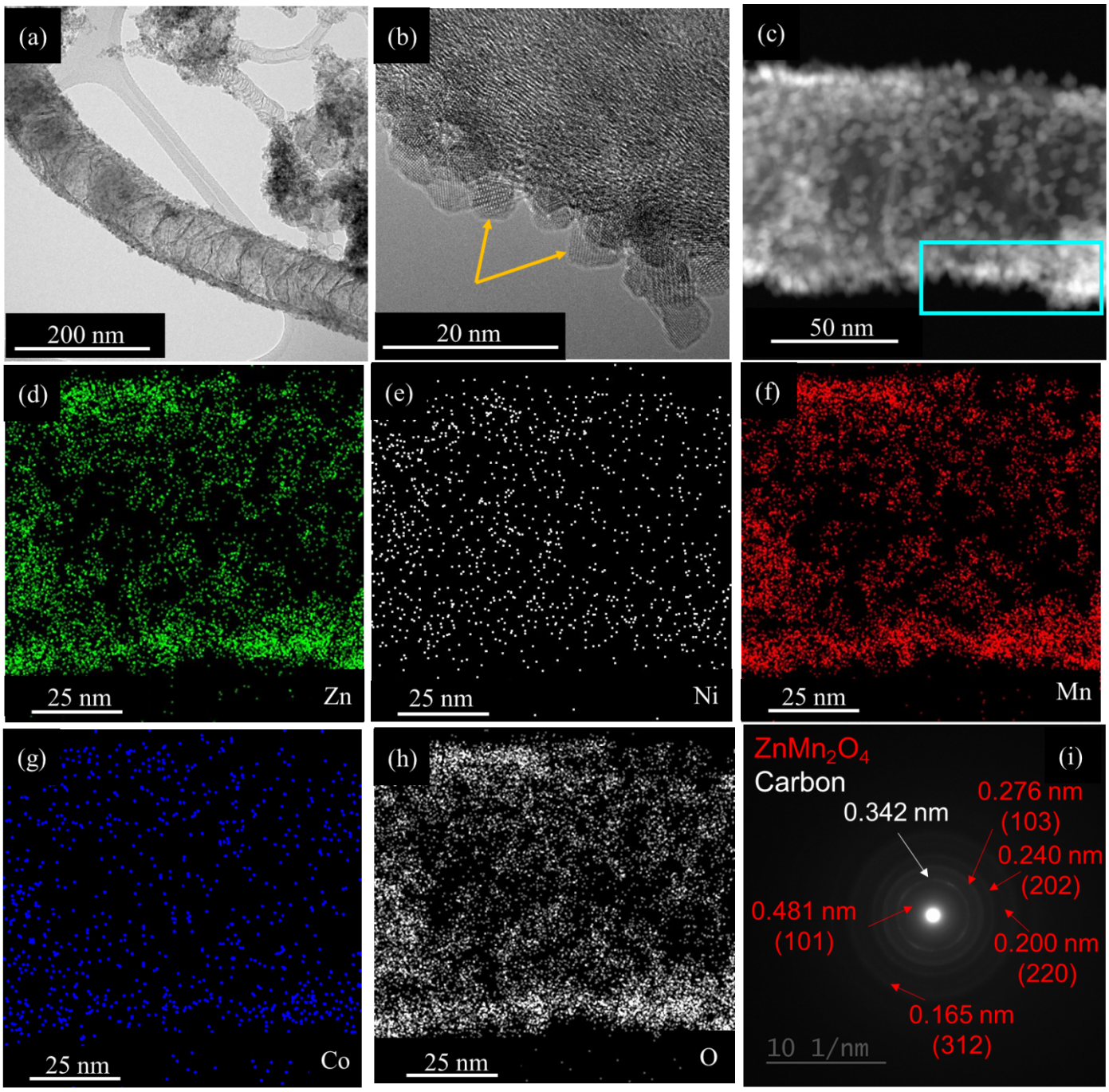

Figure 4-12 (S)TEM analysis of ZNMCO/N,S-CNT-[16:1:24:1]. (a) TEM BF image, (b) HRTEM image, (c) STEM ADF image, (d)-(h) EDX elemental maps for Zn, Ni, Mn, Co, and O, (i) SAD pattern from the cluster of nanoparticles shown in (a). The blue box in (c) outlines the area where composition analysis of the nanoparticles anchored to the N,S-CNTs was done.

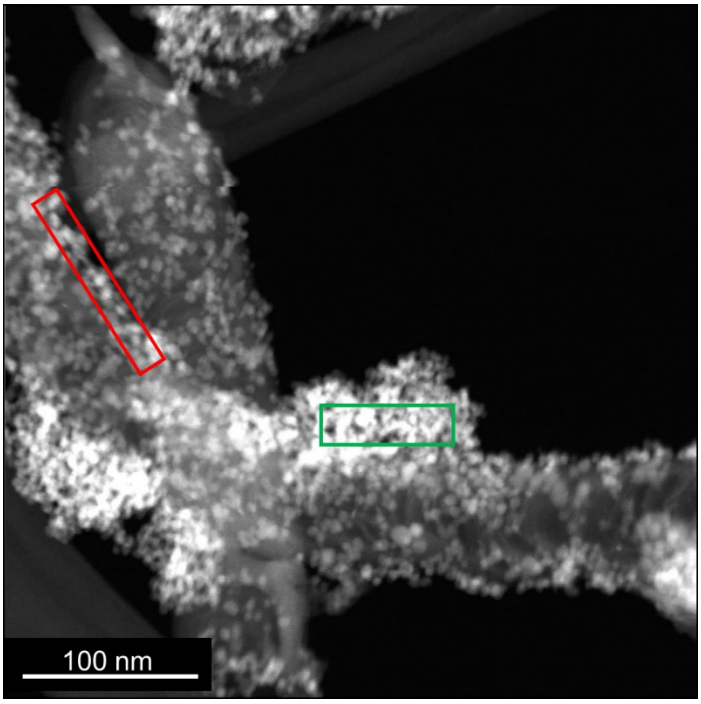

Figure 4-13 STEM ADF image of ZNMCO/N-CNT-[16:1:24:1]-An sample. The red box outlines the area for EDX analysis of nanoparticles anchored onto the N-CNTs. The green box outlines the area for EDX analysis of a cluster of nanoparticles.

Figure 4-14 shows the XPS spectra for the ZNMCO/N,S-CNT-[16:1:24:1] electrode. The survey spectrum (Figure 4-14a) shows peaks for Zn, Ni, Mn, Co, O, F, and C. Although Ni and Co are present, the accuracy of the quantitative analysis is low because of the small amount of Ni and Co relative to Zn and Mn. Additionally, the Ni peak significantly overlaps with the F KLL Auger peak at a binding energy of 861 eV. High-resolution spectra of Zn 2p, Mn 2p, Ni 2p, Co 2p, Mn 3s, and O 1s are provided in Figure 4-14b-e.

The O 1s spectrum (Figure 4-14f) can be fit to three peaks; M-O-M (~530 eV), M-O-H (~532 eV), and C-O (~535 eV) bonds. Lattice oxygen and hydroxide bonds make up the majority of the O 1s spectrum [102], [107], [108], [122]. The O 1s spectrum analysis correlates to the analysis for the ZNMCO/N-CNT-[16:1:24:1]-An electrode (Chapter 3.3.2.2).

The Zn 2p and Zn LMM Auger peaks (Figure 4-14h-i) were analyzed to confirm the valence of Zn. The Zn 2p spectrum corresponds to the Zn $2p_{3/2}$ and Zn $2p_{1/2}$ peaks at binding energies of ~1022 eV and ~1045 eV, respectively. The Zn LMM Auger peak can be fit to a

kinetic energy of ~988 eV. These results confirm that ZnO is present, which means that Zn has a valence of 2+ [33], [107], [109].

The F KLL Auger peak (861 eV) contributes to about 90 at% of the Ni 2p spectrum; thus the certainty in the Ni analysis is low. The Ni 2p high-resolution peak (Figure 4-14g) can be deconvoluted to Ni 2+ and Ni 3+ peaks, giving an average valence of 2.4 (Table 4-5). The high-resolution spectrum for Co $2p_{3/2}$ (Figure 4-14l) can be fit to the 3+ multiplet peaks, giving Co a valence of 3.0 (Table 4-5), although it should be noted that the spectrum is noisy so the analysis must be viewed with caution.

The Mn 2p and Mn 3s peaks were utilized to determine the valence of Mn (Figure 4-14j-k). Deconvolution of the Mn $2p_{3/2}$ peak gives an average valence of 3.4 (Table 4-5). As previously mentioned, the Mn valence can also be determined from the peak splitting of the 3s peaks; however, the Mn 3s spectrum overlaps with Zn 3p spectrum. As such, there is uncertainty in the results. The peak splitting for the Mn 3s spectrum is 4.2 eV, which corresponds to a valence of 4+ [95], [97], [101], [102], [122]. The Mn 2p results are likely more reliable, so the Mn valence is a mix of 4+ and 3+. XPS analysis for the ZNMCO/N-CNT-[16:1:24:1] electrode (Section 3.3.2.2) gave an average valence of 3.7 based on the Mn 3s spectrum and 3.4 based on the Mn 2p spectrum. The results are, therefore, similar for both the N-CNT and N,S-CNT electrodes.

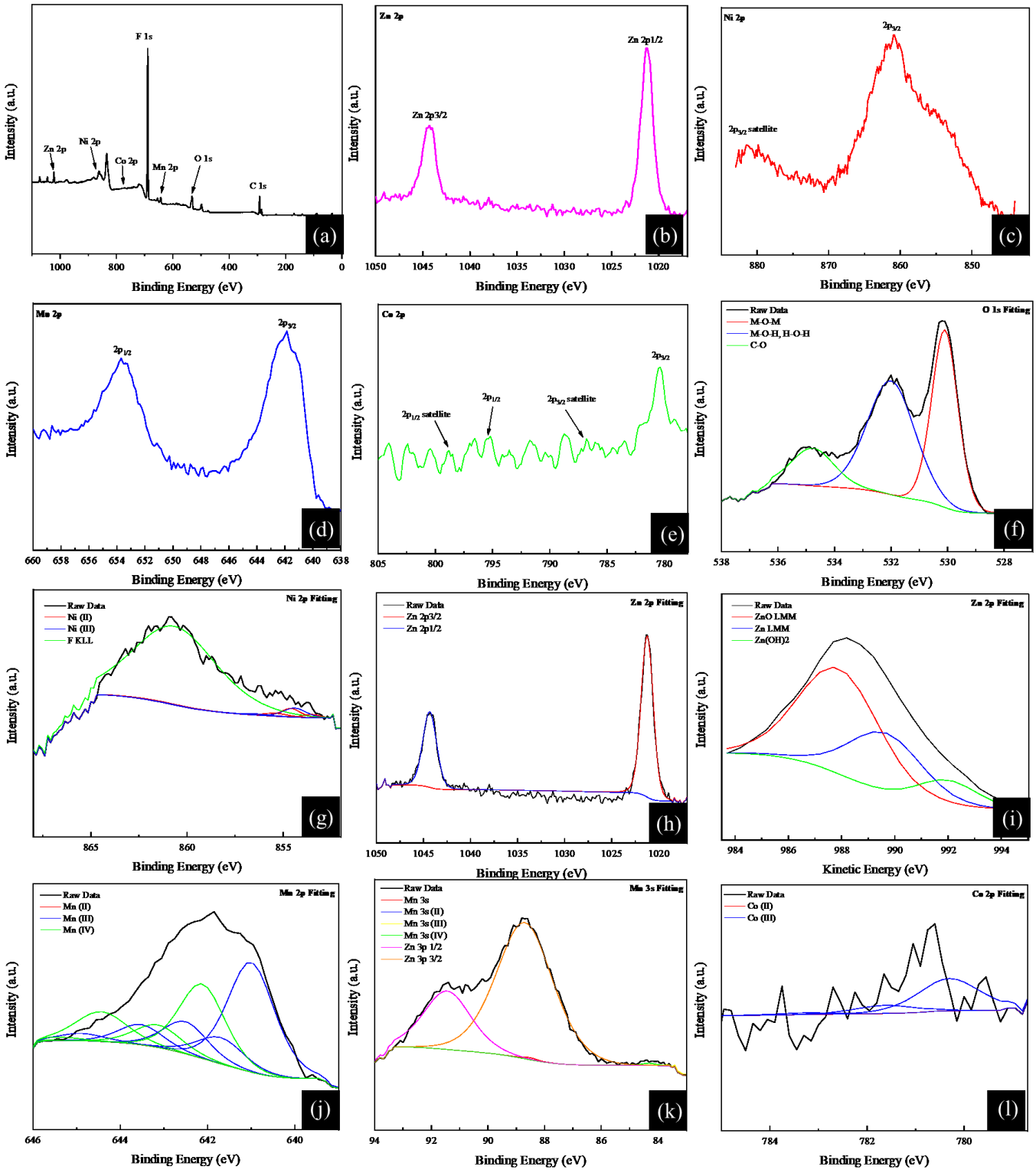

Figure 4-14 XPS spectra and fittings for ZNMCO/N,S-CNT-[16:1:24:1]. (a) Survey spectrum, (b) Zn 2p, (c), Ni 2p, (d) Mn 2p, (e) Co 2p, (f) O 1s, (g) Ni 2p, (h)-(i) Zn 2p, (j) Mn 2p, (k) Mn 3s, and (l) Co 2p high-resolution spectra.

Table 4-5 XPS analysis from high-resolution spectra. The average valences are calculated based on at% of each valence.

Sample	Ni 2p 3/2			Co 2p 3/2			Mn 2p 3/2				Mn 3s	
	2+ (%)	3+ (%)	Average Valence	2+ (%)	3+ (%)	Average Valence	2+ (%)	3+ (%)	4+ (%)	Average Valence	Peak Splitting (eV)	Average Valence
ZNMCO/N,S-CNT-[16:1:24:1]	57.3	42.7	**2.4**	0.0	100.0	**3.0**	0.0	59.2	40.9	**3.4**	4.2	**4.0**

A combination of the SEM, TEM/STEM and XPS results was used to identify the metallic oxide for the ZNMCO/N,S-CNT-[16:1:24:1] electrode. Electron diffraction showed a structure similar to hetaerolite ($ZnMn_2O_4$), which is a tetragonal spinel phase. SEM EDX analysis gave an overall Mn:Zn ratio of ~1.4:1 and a similar (Mn+Co):(Zn+Ni) ratio. XPS analysis provided valences for Zn and Ni of 2+, a Co valence of 3+, and a mixed valence of 3+ and 4+ for Mn. There are two possible chemical formulas for the metallic oxide. One possibility is $(Zn,Ni)(Co,Mn)_2O_4$, where the Mn has a valence of 3+. The other possibility is a $Mn(Zn,Ni)_2O_4$ where Mn has a 4+ and the other metallic elements have 2+ valences. This is also supported by the Mn:Zn ratio, which is less than 2, indicating substitution from other elements and/or a mixed Mn valence [106]. This means that Zn 2+ and Ni 2+ are likely in the tetrahedral lattice sites, while Co 3+ and Mn 3+ and Mn 4+ are in the octahedral lattice sites. These microstructural characterization results match with the results in Chapter 3 (Section 3.3.2.2). The addition of S to the N-CNTs does not increase the valences in the tetra-metallic oxide. Overall there are no microstructural differences between the tetra-metallic oxide anchored onto the N-CNTs and the N,S-CNTs.

4.4. Conclusions

Doping of S onto N-CNTs was achieved by thermal treatment with thiourea. The best tri-metallic oxide (NMCO/N-CNT-[1:9:4]) and tetra-metallic oxide (ZNMCO/N-CNT-[16:1:24:1]) compositions, from Chapter 3, were then successfully anchored onto N,S-CNTs and impregnated into a porous, carbon-based gas diffusion layer (GDL). Unannealed and annealed samples of the NMCO/N,S-CNT-[1:9:4] and ZNMCO/N,S-CNT-[16:1:24:1] electrodes were investigated.

Comparing the performance of the N-CNTs and the N,S-CNTs, without the metal oxide catalyst showed that co-doping S onto the N-CNTs improved catalytic activity and battery performance relative to the N-CNTs alone. The N,S-CNTs improved ORR and OER catalytic activities to -0.178 V and 0.7 V, from -0.200 V and 0.80 V vs. Hg/HgO, respectively. The battery efficiency at 20 mA/cm^2 improved from 51.4% to 53.3%, with major improvement to the OER potential.

The NMCO/N,S-CNT-[1:9:4] unannealed electrode had an onset ORR potential of -0.137 V, an efficiency of 53.6% at 20 mA/cm^2 during rate testing, and a maximum power density of 95 mW/cm^2. Annealing of the NMCO/N,S-CNT-[1:9:4] electrode improved the performance to -0.096 V, 55.5%, and 107 mW/cm^2, for the onset ORR potential, efficiency at 20 mA/cm^2, and maximum power density, respectively. These results were comparable to the electrochemical performance of the NMCO/N-CNT-[1:9:4] electrodes in Chapter 3. The maximum power of the NMCO/N,S-CNT-[1:9:4]-An electrode was higher than that of its counterpart on N-CNTs.

The ZNMCO/N,S-CNT-[16:1:24:1] unannealed electrode had an onset ORR potential of -0.168 V, an efficiency of 56% at 20 mA/cm^2 during rate testing, and a maximum power density of 100 mW/cm^2. Annealing this sample, ZNMCO/N,S-CNT-[16:1:24:1]-An, improved the catalytic activity, to -0.109 V, decreased the maximum power density (85 mW/cm^2), and produced a similar battery efficiency at 20 mA/cm^2 of 55.6%. Comparison with the ZNMCO/N-CNT-[16:1:24:1] electrodes showed that the results were not significantly different; however the maximum power density of the ZNMCO/N-CNT-[16:1:24:1]-An electrode was higher than that of the ZNMCO/N,S-CNT-[16:1:24:1]-An electrode, by about 40 mW/cm^2.

The bifunctional cycling test, at 10 mA/cm^2 for 200 cycles, for the NMCO/N,S-CNT-[1:9:4] electrode showed stability and OER potential improvement when compared to the equivalent test done on the NMCO/N-CNT-[1:9:4]-An electrode. The overall efficiency (after cycling) of the NMCO/N,S-CNT-[1:9:4] electrode was ~55%, while the NMCO/N-CNT-[1:9:4]-An electrode had an overall efficiency of ~52%. Comparison of the ZNMCO/N,S-CNT-[16:1:24:1] and ZNMCO/N-CNT-[16:1:24:1]-An electrodes bifunctional cycling tests did not show a significant difference between the electrodes, with efficiencies ~54% and ~56%, respectively. The best performing electrodes were the NMCO/N,S-CNT-[1:9:4] and the ZNMCO/N-CNT-[16:1:24:1]-An electrodes.

The performance increase for the NMCO/N,S-CNT-[1:9:4]-An electrode is attributed to the increased Co valence, as a result of S-doping. This effect was not observed for the

ZNMCO/N,S-CNT-[16:1:24:1] electrodes, since Co was already at a valence of 3+ in the ZNMCO/N-CNT-[16:1:24:1] electrodes. Overall, co-doping S onto N-CNTs had little to no effect on the electrochemical performance of the impregnated metal oxide/N-CNT catalysts.

5.0. Conclusions and Future Work

5.1. Conclusions

This thesis explored different catalysts to improve the air-electrode performance in zinc-air batteries. A wide range of Ni-Mn-Co and Zn-Ni-Mn-Co oxides, based on previous work in our group and a design of experiments (DOE), were anchored onto N-CNTs were prepared and impregnated into a porous carbon gas diffusion layer (GDL). These catalysts showed promising advantages versus similar literature studies as well as previously studied catalysts in our group. In an attempt to improve these results sulfur was doped onto the N-CNTs (N,S-CNTs) and the best tri- and tetra-metallic oxides were decorated onto the N,S-CNTs. The following sections will go into further detail on the achievements of each study.

5.1.1. Tri- and Tetra-Metallic Work on N-CNTs

Tri-metallic, Ni-Mn-Co oxides (NMCO) and tetra-metallic, Zn-Ni-Mn-Co oxides (ZNMCO), determined from previous work and a DOE, anchored onto N-CNTs were successfully synthesized and impregnated into a porous, carbon-based gas diffusion layer (GDL) using a simple method. The NMCO/N-CNT-[1:9:4]-An electrode had the best rate testing efficiency of 58.4% at 20 mA/cm^2, while the NMCO/N-CNT-[1:5:1] electrode had excellent maximum power density of 116 mW/cm^2 out of the tri-metallic oxides. The best performing tetra-metallic oxides were the ZNMCO/N-CNT-[16:1:24:1]-An, which had an efficiency of 57.2% (at 20 mA/cm^2) and the ZNMOC/N-CNT-[1:1:5:1]-An electrode had a maximum power density of 134 mW/cm^2. Compared to Pt-Ru/C catalysts these performance specifications compare positively. Stability and OER potential during bifunctional cycling of the Ni-Mn-Co oxides improved with the addition of Zn. After 200 charge/discharge cycles at 10 mA/cm^2, ZNMCO/N-CNT-[16:1:24:1]-An maintained an efficiency of 56.4%. Both tri-metallic and tetra-metallic oxides outperformed Pt-Ru/C during cycle testing.

5.1.2. Tri- and Tetra-Metallic Work on N,S-CNTs

Co-doped S and N CNTs (N,S-CNTs) were successfully synthesized. Tri-metallic (Ni-Mn-Co) and tetra-metallic (Zn-Ni-Mn-Co) transition metal oxides compositions previously determined (Chapter 3.0) were then successfully anchored onto N,S-CNTs and impregnated into

a porous, carbon-based gas diffusion layer (GDL). Comparison of the previously studied oxides on N-CNTs and the equivalent oxides on N,S-CNTs microstructural characteristics do not show significant differences. However, the electrochemical results show significant improvement to the tri-metallic oxides, while the tetra-metallic oxides show no or negative effects. The best performing samples were the ZNMCO/N,S-CNT-[16:1:24:1] with an efficiency of 56.0% at 20 mA/cm^2, and the NMCO/N,S-CNT-[1:9:4] with a maximum power density of ~95 mW/cm^2. These results are comparable to the reference catalyst Pt-Ru/C. The addition of sulfur to the Ni-Mn-Co oxide improved the maximum power density by about 10 mW/cm^2, as well as positively impacted the NMCO bifunctional cycling performance by lowering the OER potential (2.05 V), giving an overall efficiency of 55.1% for 200 charge-discharge cycles at 10 mA/cm^2. Bifunctional cycling tests of the Zn-Ni-Mn-Co oxides showed little to no improvement with the co-doped CNTs. Additionally, annealing of the tetra-metallic oxide on N,S-CNTs negatively impacted the OER potential during full-cell rate testing. The negative impact the sulfur doped N-CNTs have on the tetra-metallic oxide could be from the addition of Zn with Ni-Mn-Co, or the significantly decreased amount of Co compared to the Ni-Mn-Co oxide tested. Both tri-metallic and tetra-metallic oxides outperform Pt-Ru/C during bifunctional cycling.

5.2. Future Work

5.2.1. Optimization of Impregnation Technique

The impregnation technique was previously designed in the Ivey group. This method was optimized based on transition metals anchored onto N-CNTs. However, the impregnation technique could be further optimized based on the specific materials used. For example, the N,S-CNTs used in Chapter 4.0 could perform better by optimizing the total amount of catalyst salt added, different amount of N,S-CNTs, time GDL is soaked in the solution, etc. As stated throughout Chapter 4.0 sulfur has a positive impact when paired with Co-based catalysts. The tetra-metallic oxide studied in Chapter 4.0 had a very low amount of Co salt added during synthesis. Therefor it would be worth further investigating more Ni-Mn-Co and Zn-Ni-Mn-Co oxides on N,S-CNTs to study the effect sulfur has on various amounts of metal oxides.

Additionally, sequential impregnation with different catalysts could show synergistic effects and positively impact the electrode during bifunctional cycling. Studying different methods of sequential impregnation e.g., impregnating the microporous layer and then the

macroporous layer of the GDL with the same or different catalyst solutions. Impregnating both layers of the GDL is currently being done within our group.

Further optimization of the transition metal oxide may be worth pursuing. This could include trying different metal salt contents and/or trying five or more metal salts to create a high entropy alloy. Preliminary investigation was done into a Fe-Zn-Ni-Mn-Co oxide on N-CNTs (FZNMCO/N-CNT) with metal salt ratios of 1:1:1:1:1. Full-cell rate testing revealed an efficiency of ~54% and a good OER potential of 2.02 V, at 20 mA/cm^2, which are comparable to ZNMCO/N-CNT results in Chapter 3.3.2.1. Testing different metal ratios could improve the efficiency and cycling behaviour.

Studies have used heteroatom doped graphene combined with nanoparticles as bifunctional catalysts with some success. Taking this concept and doping the porous carbon GDL with heteroatoms and impregnating the heteroatom doped GDL with transition metal oxide nanoparticles decorating heteroatom CNTs could further improve the bifunctional properties of the air electrode.

5.2.2. Heteroatom Doped CNTs

Thiourea was used as a precursor for sulfur doping N-CNTs. The amount of thiourea used was optimized while the amount of N-CNTs added remained constant. It would be worth further investigation into the optimal ratio of thiourea to N-CNTs to maximize the amount of sulfur being doped on the N-CNTs. Trying a different approach to obtaining co-doped CNTs with S and N could also be investigated.

Doping multiple heteroatoms produces synergistic effects. Heteroatoms have different electronegativities than carbon, which improve catalytic activity through charge separation and transfer effects [123]. Wu *et al.* had round trip bifunctional efficiency of ~57.5% for 200 cycles at 10 mA/cm^2 with N, F, P-ternary doped carbon nanofiber catalysts [43]. Additionally, B has the ability to affect the carbon valence which can lead to a reduced activation energy, improving the reaction kinetics at the air electrode [91]. Ali *et al.* [91] produced a Co phosphide on B, N, and P-doped CNTs that exhibited good long term stability at -0.25 V vs. RHE for 15 h with little to no performance degradation. Investigating different heteroatom co- or tri-doped CNTs combined with transition metal oxides and the impregnation technique could prove beneficial for rechargeable ZABs.

6.0. References

[1] Fu J, Cano ZP, Park MG, Yu A, Fowler M, and Chen Z (2017) Electrically Rechargeable Zinc–Air Batteries: Progress, Challenges, and Perspectives. Adv. Mater.7:1-34. https://doi.org/10.1002/adma.201604685

[2] Fang W, Zhao J, Zhang W, Chen P, Bai Z, and Wu M (2021) Recent Progress and Future Perspectives of Flexible Zn-Air Batteries. J. Alloys Compd. 869:158918. https://doi.org/10.1016/j.jallcom.2021.158918

[3] Chang Z and Zhang X (2018) Introduction to Metal-Air Batteries: Theory and Basic Principles. Metal-Air Batteries: Fundamentals and Applications. 1–9

[4] Schroder D (2015) Analysis of Reaction and Transport Processes in Zinc Air Batteries. Springer

[5] Pei P, Wang K, and Ma Z (2014) Technologies for Extending Zinc-Air Battery's Cyclelife: A Review. Appl. Energy. 128:315–324. https://doi.org/10.1016/j.apenergy.2014.04.095

[6] Wei L, Ang E, Yang Y, Qin Y, Zhang Y, Ye M, Liu Q, and Li C (2020) Recent Advances of Transition Metal Based Bifunctional Electrocatalysts for Rechargeable Zinc-Air Batteries. J. Power Sources. 477: 228696. https://doi.org/10.1016/j.jpowsour.2020.228696

[7] Worku AK, Ayele DW, and Habtu NG (2021) Recent Advances and Future Perspectives in Engineering of Bifunctional Electrocatalysts for Rechargeable Zinc–Air Batteries. Mater. Today Adv.9:100116.https://doi.org/10.1016/j.mtadv.2020.100116

[8] Berg H (2017) Battery technologies for electric vehicles. Batteries for Electric Vehicles - Materals and Electrochemistry.139–167

[9] Yu T, Cai R, and Chen Z (2018) Zn – Air Batteries. Metal-Air Batteries: Fundamentals and Applications.265–290

[10] Jiao D, Ma Z, Li J, Han Y, Mao J, Ling T, and Qiao S (2020) Test Factors Affecting the Performance of Zinc–Air Battery. J. Energy Chem. 44:1–7. https://doi.org/10.1016/j.jechem.2019.09.008

[11] Ghareghashi A and Mohebbi A (2020) Anode Materials for Zinc-Air Batteries. Zinc Batteries: Basics, Developments, and Applications.103–130

[12] Neburchilov V, Wang H, Martin JJ, and Qu W (2010) A Review On Air Cathodes for Zinc-Air Fuel Cells. J. Power Sources.195:1271–1291.https://doi.org/10.1016/j.jpowsour.2009.08.100

[13] Davari E and Ivey DG (2018) Bifunctional Electrocatalysts for Zn-Air Batteries. Sustain. Energy Fuels 2:39–67. https://doi.org/10.1039/c7se00413c

[14] Tsehaye MT, Alloin F, Iojoiu C, Tufa, RA, Aili, D, Fischer, P, and Velizarov, S (2020) Membranes for Zinc-Air Batteries: Recent Progress, Challenges and Perspectives. J. Power Sources.475:228689. https://doi: 10.1016/j.jpowsour.2020.228689

[15] Beard K (2019) Battery Components. In Linden's Handbook of Batteries, 5th edn. pp 5

[16] Tran TNT, Aasen D, Zhalmuratova D, Labbe M, Chung H, and Ivey DG (2020) Compositional Effects of Gel Polymer Electrolyte and Battery Design for Zinc-Air Batteries. Batter. Supercaps. 3:917–927. https://doi.org.10.1002/batt.202000054

[17] Jónsson E (2020) Ionic Liquids as Electrolytes for Energy Storage Applications – A Modelling Perspective. Energy Storage Mater. 25:827–835. https://doi.org/10.1016/j.ensm.2019.08.030

[18] Alwast D, Schnaidt J, Jusys Z, and Behm RJ (2020) Ionic Liquid Electrolytes for Metal-Air Batteries: Interactions between O2, Zn 2+ and H2O Impurities. J. Electrochem. Soc. 167:070505. https://doi.org/10.1149/2.0052007jes

[19] Jin Y and Chen F (2015) Facile Preparation of Ag-Cu Bifunctional Electrocatalysts for Zinc-Air Batteries. Electrochim. Acta. 158:437–445. https://doi.org/10.1016/j.electacta.2015.01.151

[20] Gu Y, Yan G, Lian Y, Qi P, Mu Q, Zhang C, Deng Z, and Peng Y (2019) MnIII-Enriched α-MnO2 Nanowires as Efficient Bifunctional Oxygen Catalysts for Rechargeable Zn-Air Batteries. Energy Storage Mater.23:252–260. https://doi.org/10.1016/j.ensm.2019.05.006

[21] Reier T, Oezaslan M, and Strasser P (2012) Electrocatalytic Oxygen Evolution Reaction (OER) on Ru, Ir, and Pt Catalysts: A Comparative Study of Nanoparticles and Bulk Materials. ACS Catal.2:1765–1772. https://doi.org/10.1021/cs3003098

[22] Gu P, Zheng M, Zhao Q, Xiao X, Xue H, and Pang H (2017) Rechargeable Zinc-Air Batteries: A Promising Way to Green Energy. J. Mater. Chem. A.5:7651–7666. https://doi.org/10.1039/c7ta01693j

[23] Shi Q, Peng F, Liao S, Wang H, Yu H, Liu Z, Zhang B, and Su D (2013) Sulfur and Nitrogen Co-Doped Carbon Nanotubes for Enhancing Electrochemical Oxygen Reduction Activity in Acidic and Alkaline Media. J. Mater. Chem. A. 1:14853–14857. https://doi.org/10.1039/c3ta12647a

[24] Li P, Ma R, Zhou Y, Chen Y, Liu Q, Peng G, Liang Z, and Wang J (2015) Spinel Nickel Ferrite Nanoparticles Strongly Cross-Linked with Multiwalled Carbon Nanotubes as a Bi-Efficient Electrocatalyst for Oxygen Reduction and Oxygen Evolution. RSC Adv. 5:73834–73841. https://doi.org/10.1039/c5ra14713a

[25] Zhao S, Yan L, Luo H, Mustain W, and Xu H (2017) Recent Progress and Perspectives of Bifunctional Oxygen Reduction/Evolution Catalyst Development for Regenerative Anion Exchange Membrane Fuel Cells. Nano Energy. 47:172–198. https://doi.org/10.1016/j.nanoen.2018.02.015

[26] Yang J, Ganesan P, Ishihara A, and Nakashima N (2019) Carbon Nanotube-Based Non-Precious Metal Electrode Catalysts for Fuel Cells, Water Splitting and Zinc-Air Batteries. ChemCatChem. 11:5929–5944.https://doi.org10.1002/cctc.201901785

[27] Yang Y, Yang C, Tao K, Ma Q, and Han L (2020) Construction of S-Doped ZnCo2O4 Microspindles with Enhanced Electrochemical Performance for Supercapacitors. Vacuum. 181:109740. https://10.1016/j.vacuum.2020.109740

[28] Nivetha R, Chella S, Kollu P, Jeong SK, Bhatnagar A, and Andrews NG (2018) Cobalt and Nickel Ferrites Based Graphene Nanocomposites for Electrochemical Hydrogen Evolution. J. Magn. Magn. Mater. 448:165–171. https://doi.org/10.1016/j.jmmm.2017.05.083

[29] Chen HM and Hsu CS (2017) Developed In-Situ X-Ray Spectroscopy to Investigate the Catalyst System Toward Oxygen Evolution Reaction. SPring-8/ SACLA. 22:297–305

[30] Green MA, Ho-Baillie A, and Snaith HJ (2014) The Emergence of Perovskite Solar Cells. Nat. Photonics. 8:506–514. https://doi.org/10.1038/nphoton.2014.134

[31] Osgood H, Devaguptapu SV, Xu H, Cho J, and Wu G (2016) Transition Metal (Fe, Co, Ni, and Mn) Oxides for Oxygen Reduction and Evolution Bifunctional Catalysts in Alkaline Media. Nano Today.11:601–625.https://doi.org/10.1016/j.nantod.2016.09.001

[32] Huang T, Zhao C, Zheng R, Zhang Y, and Hu Z (2015) Facilely Synthesized Porous ZnCo2O4 Rodlike Nanostructure for High-Rate Supercapacitors. Ionics (Kiel). 21:3109–

3115.https://doi.org/10.1007/s11581-015-1491-2

[33] Xu N, Q Nie, Liu J, Huang H, Qiao J, and Zhou XD (2020) Insert Zn 2+ in Tetrahedral Sites of Bi-metal Zn-Co Spinel Oxides with High Oxygen Catalytic Performance for Liquid and Flexible Zinc-Air Batteries. J. Electrochem. Soc. 167:050512. https://doi.org/10.1149/1945-7111/ab6e5d

[34] Osgood H, Devaguptapu SV, Xu H, Cho J, and Wu G (2016) Transition Metal (Fe, Co, Ni, and Mn) Oxides for Oxygen Reduction and Evolution Bifunctional Catalysts in Alkaline Media. Nano Today.11:601–625.https://doi.org/10.1016/j.nantod.2016.09.001

[35] Meng Y, Song W, Huang H, Ren Z, Chen SY, and Suib SL (2014) Structure-Property Relationship of Bifunctional MnO2 Nanostructures: Highly Efficient, Ultra-Stable Electrochemical Water Oxidation and Oxygen Reduction Reaction Catalysts Identified in Alkaline Media. J. Am. Chem. Soc.136:11452–11464.https://doi.org/10.1021/ja505186m

[36] Mainar AR, Colmenares LC, Leonet O, Alcaide F, Iruin JJ, Weinberger S, Hacker V, Iruin E, Urdanpilleta I, and Blazquez JA (2016) Manganese Oxide Catalysts for Secondary Zinc-Air Batteries: From Electrocatalytic Activity to Bifunctional Air Electrode Performance. Electrochim. Acta. 217:80–91. https://doi.org/10.1016/j.electacta.2016.09.052

[37] Zhong Y, Dai J, Xu X, Su C, and Shao Z (2020) Facilitating Oxygen Redox on Manganese Oxide Nanosheets by Tuning Active Species and Oxygen Defects for Zinc-Air Batteries. ChemElectroChem. 7:4949–4955. https://doi.org/10.1002/celc.202001419

[38] Yang D, Tan H, Rui X, and Yu Y (2019) Electrode Materials for Rechargeable Zinc-Ion and Zinc-Air Batteries: Current Status and Future Perspectives

[39] Guan Z, Zhang X, Fang J, Wang X, Zhu W, and Zhuang Z (2020) Fe,Ni,S,N-Doped Carbon Materials as Highly Active Bi-Functional Catalysts for Rechargeable Zinc-Air Battery. Mater. Lett.258:126826. https://doi.org/10.1016/j.matlet.2019.126826

[40] Wei HL, Tan AD, Hu SZ, Piao JH, and Fu ZY (2021) Efficient Spinel Iron-Cobalt Oxide/Nitrogen-Doped Ordered Mesoporous Carbon Catalyst for Rechargeable Zinc-Air Batteries. Chinese J. Catal. 42:1451–1458.https://doi.org/10.1016/S1872-2067(20)63752-4

[41] Mousavifar SA, Ganjali MR, Faridbod F, and Norouzi P (2021) A Novel Nano-Electrocatalyst Based on LaCoFe2O4–Graphene as a Candidate Cathode for Metal–Air

Batteries. J. Mater. Sci. Mater. Electron. 8535–8544. https://doi.org/10.1007/s10854-021-05484-7

[42] Huang Z, Qin X, Gu X, Li G, Mu Y, Wang N, Ithisuphalap K, Wang H, Guo Z, Shi Z, Wu G, and Shao M (2018) Mn3O4 Quantum Dots Supported on Nitrogen-Doped Partially Exfoliated Multiwall Carbon Nanotubes as Oxygen Reduction Electrocatalysts for High-Performance Zn-Air Batteries. ACS Appl. Mater. Interfaces. 10:23900–23909. https://doi.org/10.1021/acsami.8b06984

[43] Wu M, Wang Y, Wei Z, Wang L, Zhuo M, Zhang J, Han X, and Ma J (2018) Ternary Doped Porous Carbon Nanofibers with Excellent ORR and OER Performance for Zinc-Air Batteries. J. Mater. Chem. A. 6:10918–10925.htpps://doi.org/10.1039/c8ta02416b

[44] Jiang T, Dai P, Zhang W, and Wu M (2021) Fish Bone-Derived N, S Co-Doped Interconnected Carbon Nanofibers Network Coupled with (Fe, Co, Ni)9S8 Nanoparticles as Efficient Bifunctional Electrocatalysts for Rechargeable and Flexible All-Solid-State Zn-Air Battery. Electrochim. Acta.373:137903. https://doi.org/10.1016/j.electacta.2021.137903

[45] Zhu Q (2021) Synthesis and Characterization of Nitrogen-Doped Carbon Nanotubes. J. Mater. Sci. Mater. Electron. pp. 9694–970. https://doi.org/10.1007/s10854-021-05631-0

[46] Aasen D, Clark M, and Ivey DG (2019) A Gas Diffusion Layer Impregnated with Mn 3 O 4 -Decorated N-Doped Carbon Nanotubes for the Oxygen Reduction Reaction in Zinc-Air Batteries. Batter. Supercaps. 2:882–893. https://doi.org/10.1002/batt.201900102

[47] Dobrzańska-Danikiewicz AD, Łukowiec D, Cichocki D, and Wolany W (2013) Carbon Nanotubes Decorating Methods. Arch. Mater. Sci. Eng. 61:53–61.

[48] Liu X, Park M, Kim MG, Gupta S, Wang X, and Wu G (2016) High-Performance Non-Spinel Cobalt-Manganese Mixed Oxide-Based Bifunctional Electrocatalysts for Rechargeable Zinc-Air Batteries. Nano Energy. 20:315–325.https://doi.org/10.1016/j.nanoen.2015.11.030

[49] Wu M, Zhang G, Chen N, Hu Y, Regier T, Rawach D, and Sun S (2021) Self-Reconstruction of Co/Co2P Heterojunctions Confined in N-Doped Carbon Nanotubes for Zinc-Air Flow Batteries. ACS Energy Lett.1153–1161. https://doi.org/10.1021/acsenergylett.1c00037

[50] Chen Z, Yu A, Higgins D, Li H, Wang H, and Chen Z (2012) Highly Active and Durable

Core-Corona Structured Bifunctional Catalyst for Rechargeable Metal-Air Battery Application. Nano Lett.12:1946–1952. https://doi.org/10.1021/nl2044327

[51] Li C, Zhou E, Yu Z, Liu H, and Xiong M (2020) Tailor-Made Open Porous 2D CoFe/SN-Carbon with Slightly Weakened Adsorption Strength of ORR/OER Intermediates as Remarkable Electrocatalysts Toward Zinc-Air Batteries. Appl. Catal. B Environ. 269:118771. https://doi.org/10.1016/j.apcatb.2020.118771

[52] Fang G, Gao J, Lv J, Jia H, Li H, Liu W, Xie G, Chen Z, Huang Y, Yuan Q, Liu X, Lin X, Sun S, and Qiu HJ (2020) Multi-Component Nanoporous Alloy/(Oxy)hydroxide for Bifunctional Oxygen Electrocatalysis and Rechargeable Zn-Air Batteries. Appl. Catal. B Environ. 268:118431. https://doi.org/10.1016/j.apcatb.2019.118431

[53] Grzesik Z, Smoła G, Miszczak M, Stygar M, Dąbrowa J, Zajusz M, Świerczek K, and Danielewski M (2020) Defect Structure and Transport Properties of (Co,Cr,Fe,Mn,Ni)3O4 Spinel-Structured High Entropy Oxide. J. Eur. Ceram. Soc. 40:835–839. https://doi.org/10.1016/j.jeurceramsoc.2019.10.026

[54] Dai W, Lu T, and Pan Y (2019) Novel and Promising Electrocatalyst for Oxygen Evolution Reaction Based on MnFeCoNi High Entropy Alloy. J. Power Sources. 430:104–111. https://doi.org/10.1016/j.jpowsour.2019.05.030

[55] Jin Z, Lyu J, Zhao YL, Li H, Lin X, Xie G, Liu X, Kai JJ, and Qiu HJ (2020) Rugged High-Entropy Alloy Nanowires with in Situ Formed Surface Spinel Oxide As Highly Stable Electrocatalyst in Zn-Air Batteries. ACS Mater. Lett. 2:1698–1706. https://doi/org/10.1021/acsmaterialslett.0c00434

[56] Sarkar A, Breitung B, and Hahn H (2020) High Entropy Oxides: The Role of Entropy, Enthalpy and Synergy. Scr. Mater.187:43–48. https://doi.org10.1016/j.scriptamat.2020.05.019

[57] Li S, Zhou X, Fang G, Xie G, Liu X, Lin X, and Qiu HJ (2020) Multicomponent Spinel Metal Oxide Nanocomposites as High-Performance Bifunctional Catalysts in Zn-Air Batteries. ACS Appl. Energy Mater. 3:7710–7718. https://doi.org/10.1021/acsaem.0c01121

[58] Zhao C, Ding F, Lu Y, Chen L, and Hu YS (2020) High-Entropy Layered Oxide Cathodes for Sodium-Ion Batteries. Angew. Chemie - Int. Ed. 59:264–269. https://doi.org/10.1002/anie.201912171

[59] Zhu S, Chen Z, Li B, Higgins D, Wang H, Li H, and Chen Z (2011) Nitrogen-Doped Carbon Nanotubes as Air Cathode Catalysts in Zinc-Air Battery. Electrochim. Acta. 56:5080–5084. https://doi.org/10.1016/j.electacta.2011.03.082

[60] Veera Manohara Reddy Y, Prabhakara Rao V, Vijaya Bhaskar Reddy A, Lavanya M, Venu M, Lavanya M, and Madhavi G (2015) Determination of Dopamine in Presence of Ascorbic Acid and Uric Acid Using Poly (Spands Reagent) Modified Carbon Paste Electrode. Mater. Sci. Eng. C. 57:378–386. https://doi.org/10.1016/j.msec.2015.08.005

[61] Wang H, Qian D, Xiao X, Deng C, Liao L, Deng J, and Lin YW (2018) Preparation and Application of a Carbon Paste Electrode Modified with Multi-Walled Carbon Nanotubes and Boron-Embedded Molecularly Imprinted Composite Membranes. Bioelectrochemistry. 121:115–124. https://doi.org/10.1016/j.bioelechem.2018.01.006

[62] Basile F, Benito P, Fornasari G, Monti M, Scavetta E, Tonelli D, and Vaccari A (2010) A Novel Electrochemical Route for the Catalytic Coating of Metallic Supports. Stud. Surf. Sci. Catal.175:51–58. https://doi.org/10.1016/S0167-2991(10)75007-2

[63] Ranjbar-Nouri Z, Soltanieh M, and Rastegari S (2018) Applying the Protective CuMn2O4 Spinel Coating on AISI-430 Ferritic Stainless Steel Used as Solid Oxide Fuel Cell Interconnects. Surf. Coatings Technol.334:365–372. https://doi.org/10.1016/j.surfcoat.2017.11.036

[64] Besra L and Liu M (2007) A Review on Fundamentals and Applications of Electrophoretic Deposition (EPD). Prog. Mater. Sci. 52:1–61.https://doi.org/10.1016/j.pmatsci.2006.07.001

[65] Therese GHA, Dinamani M, and Kamath PV (2005) Electrochemical Synthesis of Perovskite Oxides. J. Appl. Electrochem. 35:459–465. https://doi.org/10.1007/s10800-004-8346-2

[66] Therese GHA, and Kamath PV (2000) Electrochemical Synthesis of Metal Oxides and Hydroxides. Chem. Mater. 12:1195–1204. https://doi.org/10.1021/cm990447a

[67] Muresan LM (2016) Electrodeposited Zn-Nanoparticle Composite Coatings for Corrosion Protection of Steel. Handbook of Nanoelectrochemistry. pp. 1–17

[68] Tatiparti SSV and Ebrahimi F (2012) Potentiostatic Versus Galvanostatic Electrodeposition of Nanocrystalline Al-Mg Alloy Powders. J. Solid State Electrochem. 16:1255–1262. https://dio.org/10.1007/s10008-011-1522-5

[69] Xiong M and Ivey DG (2017) Sequentially Electrodeposited MnO X /Co-Fe as Bifunctional Electrocatalysts for Rechargeable Zinc-Air Batteries. J. Electrochem. Soc.164:A1012–A1021. https://doi.org/10.1149/2.0481706jes

[70] Sun Z, Wang R, Nikiforov AY, Gopalan S, Pal UB, and Basu SN (2018) CuMn1.8O4 Protective Coatings on Metallic Interconnects for Prevention of Cr-Poisoning in Solid Oxide Fuel Cells. J. Power Sources. 378:125–133. https://doi.org/10.1016/j.jpowsour.2017.12.031

[71] Jiang SP (2006) A Review of Wet Impregnation - An Alternative Method for the Fabrication of High Performance and Nano-Structured Electrodes of Solid Oxide Fuel Cells. Mater. Sci. Eng. A. 418:199–210. https://doi.org/10.1016/j.msea.2005.11.052

[72] Inkson BJ (2016) Scanning Electron Microscopy (SEM) and Transmission Electron Microscopy (TEM) for Materials Characterization. Mater. Charact. Using Nondestruct. Eval. Methods. pp. 17–43. https://dio.org/10.1016/B978-0-08-100040-3.00002-X

[73] J Goldstein J, Lyman C, Newbury D, Lifshin E, Sawyer L, Echlin P, Joy D, and Michael J (2003) Scanning Electon Microscopy and X-Ray Microanalysis, 3rd ed. Springer

[74] Invitation To The SEM World. JEOL USA, p. 54

[75] Zhou W, Apkarian R, Wang ZL, and Joy D (2007) Fundamentals of scanning electron microscopy (SEM). Scanning Microscopy for Nanotechnology: Techniques and Applications. pp. 1–40

[76] Han W, Jiao H, and Fox D (2018) Scanning electron microscopy. Springer Tracts Mod. Phys. 272:35–68. https://doi.org/10.1007/978-981-13-0454-5_2

[77] Walther T (2017) Transmission Electron Microscopy of Nanostructures. Elsevier Inc.

[78] Kim B and Hochella MF (2015) Analytical Transmission Electron Microscopy and Scanning Transmission Electron Microscopy Techniques for the Characterization of Nanomaterial Composition, Phase and Crystallinity. Frontiers of nanoscience. 8:123-152. https://doi.org/0.1016/B978-0-08-099948-7.00004-X

[79] Abd Mutalib M, Rahman MA, Othman MHD, Ismail AF, and Jaafar J (2017) Scanning Electron Microscopy (SEM) and Energy-Dispersive X-Ray (EDX) Spectroscopy. Elsevier B.V

[80] Moulder JF, Stickle WF, Sobol PE, and Bomben KD (2005) Handbook of X-Ray Photoelectron Spectroscopy

[81] Seyama H, Soma M, and Theng BKG (2013) X-Ray Photoelectron Spectroscopy. Development in Clay Science. 5:161-176

[82] Van Der Heide P (2012) Introduction. In X-ray Photoelectron Spectroscopy: An Introduction to Principles and Practices. pp. 1–12

[83] Carley AF and Morgan DJ (2016) Surface Analysis: X-Ray Photoelectron Spectroscopy. Ref. Modul. Mater. Sci. Mater. Eng. pp. 1–7. https://doi.org/10.1016/b978-0-12-803581-8.03311-7

[84] Zhong JQ, Wang M, Hoffmann WH, Van Spronsen MA, Lu D, and Boscoboinik JA (2018) Synchrotron-Based Ambient Pressure X-Ray Photoelectron Spectroscopy of Hydrogen and Helium. Appl. Phys. Lett. 112:1–5. https://doi.org/10.1063/1.5022479

[85] Stojilovic N (2012) Why Can't We See Hydrogen in X-Ray Photoelectron Spectroscopy. J. Chem. Educ.89:1331–1332. https://doi.org/10.1021/ed300057j

[86] Greenfield S and Thompson M (2008) CHNS Elemnetal Analysers. AMC Tech. Briefs. https://doi.org/10.2307/4107413

[87] Choudhary YS, Jothi L, and Nageswaran G (2017) Electrochemical Characterization. Spectroscopic Methods for Nanomaterials Characterization. 2:19-54

[88] Pletcher D, Greff D, Peat R, Peter LM, and Robinson J (2010) Potential Sweep Techniques and Cyclic Voltammetry. Instrumental Methods in Electrochemistry. 178–228

[89] Beard K (2019) Electrochemical Techniques. In Linden's Handbook of Batteries

[90] Bard A and Faulkner L (2001) Electrochemical Methods: Fundamentals and Applications

[91] Aasen D, Clark MP, and Ivey D. G (2020) (Co,Fe) 3 O 4 Decorated Nitrogen- Doped Carbon Nanotubes in Nano- Composite Gas Diffusion Layers as Highly Stable Bifunctional Catalysts for Rechargeable Zinc-Air Batteries. Batter. Supercaps 3:174–184. https://doi.org/10.1002/batt.201900168

[92] Zhao J, Cano M, Giner-Casares JJ, Luque R, and Xu G (2020) Electroanalytical Methods and Their Hyphenated Techniques for Novel Ion Battery Anode Research. Energy Environ. Sci.13:2618–2656. https://doi.org/10.1039/d0ee01184c

[93] Middlemiss LA, Rennie AJR, Sayers R, and West AR (2020) Characterisation of Batteries by Electrochemical Impedance Spectroscopy. Energy Reports. 6:232–241. https://doi.org/10.1016/j.egyr.2020.03.029

[94] Liu X, Park M, Kim MG, Gupta S, Wang X, Wu G, and Cho J (2016) High-Performance

Non-Spinel Cobalt-Manganese Mixed Oxide-Based Bifunctional Electrocatalysts for Rechargeable Zinc-Air Batteries. Nano Energy 20:315–325. https://doi.org/10.1016/j.nanoen.2015.11.030

[95] Aasen D, Clark MP, and Ivey D. G (2020) Investigation of Transition Metal-Based (Mn, Co, Ni, Fe) Trimetallic Oxide Nanoparticles on N-doped Carbon Nanotubes as Bifunctional Catalysts for Zn-Air Batteries. J. Electrochem. Soc. 167:040503. https://doi.org/10.1149/1945-7111/ab7094

[96] Wang Q, Xue Y, Sun S, Yan S, Miao H, and Liu Z (2019) Facile Synthesis of Ternary Spinel Co–Mn–Ni Nanorods as Efficient Bi-Functional Oxygen Catalysts for Rechargeable Zinc-Air Batteries. J. Power Sources 435. https://doi.org/10.1016/j.jpowsour.2019.226761

[97] Lu YT, Chien YJ, Liu CF, You TH, and Hu CC(2017) Active Site-Engineered Bifunctional Electrocatalysts of Ternary Spinel Oxides, M0.1Ni0.9Co2O4 (M: Mn, Fe, Cu, Zn) for the Air Electrode of Rechargeable Zinc-Air Batteries. J. Mater. Chem. A 5:21016–21026. https://doi.org/10.1039/c7ta06302d

[98] Aasen D, Shen Y, and Ivey DG (2020) Zn-Based Oxides Anchored to Nitrogen-Doped Carbon Nanotubes as Efficient Bifunctional Catalysts for Zn-Air Batteries. ChemElectroChem 7:2283–2296. https://doi.org/10.1002/celc.202000362

[99] Anderson M, Whitcomb P, and Bezener M (2018) Formulation Simplified: Finding the Sweet Spot through Design and Analysis of Experiments with Mixtures

[100] Chen Z, Chen Z, and Higgins D (2010) Nitrogen Doped Carbon Nanotubes and Their Impact on the Oxygen Reduction Reaction in Fuel Cells. Carbon N. Y. 48:3057–3065. https://doi.org/10.1016/j.carbon.2010.04.038

[101] Ilton ES, Post JE, Heaney PJ, Ling FT, and Kerisit SN (2015) XPS Determination of Mn Oxidation States in Mn (Hydr)Oxides. Appl. Surf. Sci. 366:475–485. https://doi.org/10.1016/j.apsusc.2015.12.159

[102] Biesinger MC, Payne BP, Grosvenor AP, Lau LWM, Gerson AR, and Smart RSC (2011) Resolving Surface Chemical States in XPS Analysis of First Row Transition Metals, Oxides and Hydroxides: Cr, Mn, Fe, Co and Ni. Appl. Surf. Sci. 257:2717– 2730. https://doi.org/10.1016/j.apsusc.2010.10.051

[103] Callister W and Rethwisch D (2010) Materials Science and Engineering: An Introduction, 9th edn. Wiley, New Jersey

[104] Hem JD, Roberson CE, and Lind CJ (1987) Synthesis and Stability of Hetaerolite, ZnMn2O4, at 25°C. Geochim. Cosmochimoca Acta 51:1539–1547

[105] Li H, Song B, Wang WJ, and Chen XL (2011) Facile Synthesis, Thermal, Magnetic, Raman Characterizations of Spinel Structure ZnMn2O4. Mater. Chem. Phys. 130:39–44. https://doi.org/10.1016/j.matchemphys.2011.04.072

[106] Pramanik A, Chattopadhyay S, Maiti S, De G, and Mahanty S (2021) Hollow-Porous Nanospheres of ZnMn2O4 Spinel: A High Energy Density Cathode for Rechargeable Aqueous Battery. Mater. Chem. Phys. 263:124373. https://doi.org/10.1016/j.matchemphys.2021.124373

[107] Biesinger, MC, Lau LWM, Gerson AR, and Smart RSC (2010) Resolving Surface Chemical States in XPS Analysis of First Row Transition Metals, Oxides and Hydroxides: Sc, Ti, V, Cu and Zn. Appl. Surf. Sci. 257:887–898. https://doi.org/10.1016/j.apsusc.2010.07.086

[108] Biesinger M (2020) X-ray Photoelectron Spectroscopy (XPS) Reference Pages. http://www.xpsfitting.com/. Accessed 22 June 2021

[109] Thermo Fisher Scientific (2021) XPS Reference Table Of Elements. https://xpssimplified.com/periodictable.php. Accessed 22 June 2021

[110] Pramanik A, Chattopadhyay S, Maiti S, De G, and Mahanty S (2021) Hollow-Porous Nanospheres of ZnMn2O4 Spinel: A High Energy Density Cathode for Rechargeable Aqueous Battery. Mater. Chem. Phys. 263:124373. https://doi.org/10.1016/j.matchemphys.2021.124373

[111] Chang S, Zhang H, and Zhang Z (2021) FeCo Alloy/N, S Dual-Doped Carbon Composite as a High-Performance Bifunctional Catalyst in an Advanced Rechargeable Zinc-Air Battery. J. Energy Chem. 56:64–71. https://doi.org/10.1016/j.jechem.2020.07.047

[112] Zhou S, Zhou QX, Su H, Wang Y, Dong Z, Dai X, and Zhang X (2019) Hybrid of Fe3C@N, S Co-Doped Carbon Nanotubes Coated Porous Carbon Derived from Metal Organic Frameworks as an Efficient Catalyst Towards Oxygen Reduction. J. Colloid Interface Sci. 533:311–318. https://doi.org/10.1016/j.jcis.2018.06.091

[113] Chang S, Zhang H, and Zhang Z (2021) FeCo Alloy/N, S Dual-Doped Carbon Composite

as a High-Performance Bifunctional Catalyst in an Advanced Rechargeable Zinc-Air Battery. J. Energy Chem. 56:64–71. https://doi.org/10.1016/j.jechem.2020.07.047

[114] Geng D, Ding NN, Hor TSA, Chien SW, Liu Z, and Zong Y (2015) Cobalt Sulfide Nanoparticles Impregnated Nitrogen and Sulfur Co-Doped Graphene as Bifunctional Catalyst for Rechargeable Zn-Air Batteries. RSC Adv. 5:7280–7284. https://doi.org/10.1039/c4ra13404d

[115] Wang J, Wu Z, Han L, Lin R, Xiao W, Xuan C, Xin HL, and Wang D (2016) Nitrogen and Sulfur Co-Doping of Partially Exfoliated MWCNTs as 3-D Structured Electrocatalysts for the Oxygen Reduction Reaction. J. Mater. Chem. A. 4:5678–5684. https://doi.org/10.1039/c6ta00490c

[116] Patil IM, Reddy V, Lokanathan M, and Kakade B (2018) Nitrogen and Sulphur Co-Doped Multiwalled Carbon Nanotubes as an Efficient Electrocatalyst for Improved Oxygen Electroreduction. Appl. Surf. Sci. 449:697–704. https://doi.org/10.1016/j.apsusc.2017.12.124

[117] Ali A, Liu Y, Mo R, Chen P, and Shen PK (2020) Facile One-Step In-Situ Encapsulation of Non-Noble Metal Co2P Nanoparticles Embedded into B, N, P Tri-Doped Carbon Nanotubes for Efficient Hydrogen Evolution Reaction. Int. J. Hydrogen Energy. 45:24312–24321. https://doi.org/10.1016/j.ijhydene.2020.06.235

[118] Hassani F and Tavakol H (2018) Synthesis of Sulfur-Doped Carbon Nanotubes from Sulfur Powder Using Chemical Vapor Deposition. Fullerenes Nanotub. Carbon Nanostructures. 26:479–486. https://doi.org/10.1080/1536383X.2018.1448793

[119] Liu Z, Wu D, Xing Y, Guo X, and Fang S (2016) Effect of In-Situ Sulfur Poisoning on Zinc-Containing Spinel-Supported Cobalt CO Hydrogenation Catalyst. Appl. Catal. A Gen. 514:164–172. https://doi.org/10.1016/j.apcata.2016.01.021

[120] Wang C (2021) Effect of Annealing Temperature on the Structure and Optical Properties of Mn Doped ZnS Thin Films. J. Mod. Opt. 68:771–775. https://doi.org/10.1080/09500340.2021.1946183

[121] Ran J, Wang T, Zhang J, Liu Y, Xu C, Xi S, and Gao D (2020) Modulation of Electronics of Oxide Perovskites by Sulfur Doping for Electrocatalysis in Rechargeable Zn-Air Batteries. Chem. Mater. 32:3439–3446. https://doi.org/10.1021/acs.chemmater.9b05148

[122] Briggs D (2005) X-Ray Photoelectron Spectroscopy (XPS)

[123] Long Y, Ye F, Shi L, Lin X, Paul R, Liu D, and Hu C (2021) N, P, and S Tri-Doped Holey Carbon as an Efficient Electrocatalyst for Oxygen Reduction in Whole pH Range for Fuel Cell and Zinc-Air Batteries. Carbon N. Y. 179:365–376. https://doi.org/10.1016/j.carbon.2021.04.039